



Development of Ray-Optical Methods for Studying the RCS of 2D Targets on a Rough Sea Surface

R.J. Burkholder, M.R. Pino and D.-H. Kwon

The Ohio State University
ElectroScience Laboratory

Department of Electrical Engineering
1320 Kinnear Road
Columbus, Ohio 43212

1990504133

Technical Report 735231-1
Grant No. N00014-98-1-0243
January 1999

Office of Naval Research
Ballston Centre Tower One
800 North Quincy Street
Arlington, VA 22217-5660

DTIC QUALITY INSPECTED 4

A. Approved for public release; Distribution is unlimited

NOTICES

When Government drawings, specifications, or other data are used for any purpose other than in connection with a definitely related Government procurement operation, the United States Government thereby incurs no responsibility nor any obligation whatsoever, and the fact that the Government may have formulated, furnished, or in any way supplied the said drawings, specifications, or other data, is not to be regarded by implication or otherwise as in any manner licensing the holder or any other person or corporation, or conveying any rights or permission to manufacture, use, or sell any patented invention that may in any way be related thereto.

REPORT DOCUMENTATION PAGE		1. REPORT NO.	2.	3. Recipient's Accession No.									
4. Title and Subtitle		Development of Ray-Optical Methods for Studying the RCS of 2D Targets on a Rough Sea Surface		5. Report Date January 1999									
7. Author(s)		R.J. Burkholder, M.R. Pino and D.-H. Kwon		6.									
9. Performing Organization Name and Address		The Ohio State University ElectroScience Laboratory 1320 Kinnear Road Columbus, OH 43212		8. Performing Org. Rept. No. 735231-1									
12. Sponsoring Organization Name and Address		Office of Naval Research Ballston Centre Tower One, 800 N. Quincy St. Arlington, VA 22217-5660		10. Project/Task/Work Unit No.									
15. Supplementary Notes				11. Contract(C) or Grant(G) No. (C) (G) N00014-98-1-0243									
16. Abstract (Limit: 200 words)				13. Report Type/Period Covered Technical Report									
				14.									
<p>The radar scattering from ship-like targets on a rough, time-varying sea surface is investigated using computational techniques developed specifically for this problem. A spectrally accelerated generalized forward-backward method is used to study the time-varying RCS, and to generate reference solutions for more approximate ray-optical techniques. The ray techniques decouple the target from the sea surface via a plane wave expansion for the sea scattered field in the vicinity of the target. Much larger targets may be analyzed using ray methods, but the accuracy is limited. It is found that the time-varying RCS of a target on a moving sea surface can peak higher than the RCS of the same target on a smooth surface. It is also found that the variation (maximum deviation) of the RCS with time increases with a decreasing coherent (time independent) component of the sea scattered field which illuminates the target. The magnitude of the coherent component is a function of frequency and elevation angle as well as the surface roughness. The roll angle of the target on the sea surface also strongly affects the RCS level, and is another useful indicator of the RCS variation.</p>													
17. Document Analysis <table> <tr> <td>a. Descriptors</td> <td>Ship RCS</td> <td>Ocean Scattering</td> </tr> <tr> <td></td> <td>Ray Methods</td> <td>Numerical Methods</td> </tr> <tr> <td></td> <td>Remote Sensing</td> <td>Rough Surface Scattering</td> </tr> </table>					a. Descriptors	Ship RCS	Ocean Scattering		Ray Methods	Numerical Methods		Remote Sensing	Rough Surface Scattering
a. Descriptors	Ship RCS	Ocean Scattering											
	Ray Methods	Numerical Methods											
	Remote Sensing	Rough Surface Scattering											
b. Identifiers/Open-Ended Terms													
c. COSATI Field/Group													
18. Availability Statement		19. Security Class (This Report)	21. No. of Pages										
A. Approved for public release; Distribution is unlimited.		Unclassified	110										
		20. Security Class (This Page)	22. Price										
		Unclassified											

Acknowledgements

The authors would like to express gratitude to Prof. Fernando Obelleiro and his graduate student Luis Landesa of the University of Vigo, Spain, for their invaluable assistance in developing and testing the Generalized Forward-Backward method, and for their technical discussions which helped advance the technology reported here. The authors also wish to acknowledge the assistance of Prof. Joel T. Johnson, Dr. Hsi-Tseng Chou and Mr. Baran Urgan for contributing their expertise and computer codes for better understanding the EM scattering from rough sea surfaces. Mrs. Dilek Colak-Kaya is thanked for her assistance in preparing numerical results for this report.

Contents

Report Documentation Page	i
Acknowledgements	iii
List of Figures	vii
1 Introduction	1
1.1 Background	1
1.2 Technical Approach	3
1.3 Organization of Report	5
2 The Generalized Forward-Backward Method	7
2.1 Introduction	7
2.2 The Conventional Forward-Backward Method	8
2.3 The Generalized Forward-Backward Method	12
2.3.1 Method Description	12
2.3.2 Solving equations (2.17) and (2.18)	15
2.3.3 Numerical results	17
2.3.4 Discussion and Conclusions	26
2.4 Spectral Acceleration for the GFB	26
2.4.1 Implementation of the Spectral Acceleration	27
2.4.2 Contour Integral	31
2.4.3 Computational cost	34
2.4.4 Results	35
2.4.5 Conclusions	42
3 Plane Wave Spectral Properties of the Sea Scattered Field	44
3.1 Introduction	44
3.2 Numerical Results	45
3.3 Conclusions	54

4 Ship Radar Cross Section Computation Using Ray-Optical Methods	56
4.1 Introduction	56
4.2 Reciprocity Formulation for the Backscattered Field	57
4.2.1 Basic Derivation	57
4.2.2 Simplification for Plane Wave Backscattering	58
4.2.3 Equivalent Current Form for a PEC Target	59
4.2.4 Local Planar Approximation for Sea Surface	60
4.3 Equivalent Ray-Optical Scattering Problem	60
4.4 Numerical Results	63
4.5 Conclusions	79
5 Statistical Properties of the Ship Radar Cross Section	80
5.1 Introduction	80
5.2 RCS as a Function of Time	81
5.3 RCS as a Function of Ship Roll Angle	88
5.4 Effect of Target Geometry on the RCS	90
5.5 Conclusions	93
6 Conclusions and Future Directions	94
6.1 General Observations	94
6.2 Future Work	96
6.3 A Final Note on Coherent Scattering	97
References	100

List of Figures

1.1	Scattering by a ship on a rough sea surface illuminated by an incident EM plane wave.	1
1.2	Ray-optical characterization of the field illuminating the ship.	3
1.3	Plane wave expansion for the incident and sea scattered field illuminating the ship.	4
1.4	Rough sea surface replaced with a locally flat surface.	4
2.1	A scattering obstacle on an ocean-like surface illuminated by a low-angle incident field.	8
2.2	(a) Ocean-like surface illuminated by a TM (E_y) polarized near-grazing incident field. (b) Forward and backward regions for the n -th matching point.	9
2.3	Composite problem and matrix decomposition in the GFB method.	13
2.4	Block decomposition of a “quasi” lower triangular matrix.	16
2.5	Source and target geometry on a sea surface with wind speed 15 m/s. Units are in meters.	18
2.6	Magnitude of the currents as a function of index number (with 10 segments/ λ): (a) the GFB Method (10 th iteration) and (b) Moment Method.	19
2.7	Magnitude of the difference between GFB and MoM currents as a function of index number.	20
2.8	Residual and absolute errors versus the number of iterations.	21
2.9	Geometry for backscatter patterns. In the pattern plots, continuous line represents Surface #1 and dotted line Surface #2. (The ship is the same in both cases.) Wind speed = 15 m/s.	22
2.10	Comparison between the backscattered field of a ship on a rough surface (Surface #1) and on a flat surface. A reference solution for an infinite flat surface found using MoM and image theory is also included.	23
2.11	Comparison between the backscattered field for Surfaces #1 and #2 with the ship. The backscattering from surface #1 without the ship is also plotted.	24
2.12	Comparison between the backscattered field for a ship on Surface #1 and on a randomly generated surface with wind speed = 7 m/s.	25
2.13	Different definitions of the strong and weak groups as a function of the position of the receiving point n	28
2.14	Integration paths of $H_0^{(2)}$ in the complex ϕ -plane.	32

2.15 Saddle points for the weak group are placed at angles close to $\phi_{s,max}$	33
2.16 Integrand of (10) for a point at the top of the target.	34
2.17 (a) Example geometry and source position (units in meters) for a 13 m high target, (b) Magnitude of the current in A/m obtained by applying the Spectral Acceleration (10 th iteration) at 300 MHz, and (c) Magnitude of the difference between the previous result and a reference solution (GFB) (10 th iteration). (d) Same result as (b) at 1.2 GHz. (e) Same result as (c) at 1.2 GHz. The length for the strong group is $L_s = 12m$	37
2.18 (a) Example geometry and source position (units in meters) for a 26 m high target, (b) Magnitude of the current in A/m obtained by applying the Spectral Acceleration (10 th iteration) at 300 MHz, and (c) Magnitude of the difference between the previous result and a reference solution (GFB) (10 th iteration). The length for the strong group is $L_s = 24 m$	38
2.19 Distribution of the currents with and without the r-cards.	39
2.20 Bistatic RCS due to the currents with and without the r-cards. Frequency = 300 MHz, elevation angle = 5°	40
2.21 Bistatic RCS for two different lengths of a flat surface. Frequency = 300 MHz, elevation angle = 5°	41
2.22 Bistatic RCS for two different lengths of rough sea surface. Frequency = 300 MHz, elevation angle = 5°, wind speed = 5 m/s.	42
2.23 CPU time per iteration required by both methods (GFB and GFB with Spectral Acceleration) on a SGI workstation with a 150 MHz IP22 Processor.	43
3.1 Incident and sea scattered fields transformed into a spectrum of plane waves over a vertical cross-section above the sea surface.	45
3.2 Plane wave spectrum due to a 1 GHz plane wave incident at 5° above a sea surface with wind speed 5 m/s. Coherent and incoherent parts are obtained by sampling 40 surface realizations.	47
3.3 Plane wave spectrum due to a 1 GHz plane wave incident at 5° above a sea surface with wind speed 10 m/s. Coherent and incoherent parts are obtained by sampling 40 surface realizations.	49
3.4 Plane wave spectrum due to a 1 GHz plane wave incident at 5° above a sea surface with wind speed 15 m/s. Coherent and incoherent parts are obtained by sampling 40 surface realizations.	50
3.5 Plane wave spectrum due to a 1 GHz plane wave incident at 1.5° above a sea surface with wind speed 15 m/s. Coherent and incoherent parts are obtained by sampling 40 surface realizations.	51
3.6 Coherent plane wave reconstruction of the total fields above the sea surface. Top: wind speed = 5 m/s. Bottom: wind speed = 10 m/s. Incident elevation angle = 5°, frequency = 1 GHz.	53

3.7	Reconstruction of the total fields above the sea surface using the 50 strongest plane wave components. Wind speed = 10 m/s. Incident elevation angle = 5°, frequency = 1 GHz.	54
4.1	Sea surface and scattering target configurations for the reciprocity formulation. Top: incident and scattered fields with target present. Middle: Incident fields with target absent. Bottom: Fields of a test source with target absent.	57
4.2	Plane wave backscattering configuration for the reciprocity formulation.	59
4.3	Local planar approximation for the sea surface and image theory used to find the scattered fields in the vicinity of the target.	61
4.4	Target illuminated by a discrete set of plane waves.	62
4.5	GO ray from the m^{th} incident plane wave which reflects from the target, hits the sea surface, and then hits the target again.	63
4.6	2D RCS of a 13 m high ship on a 402.4 m flat surface computed using GFB and image theory. Frequency = 1 GHz.	64
4.7	2D RCS of a 13 m high ship on a 402.4 m surface computed using coherent components of sea scattered incident field. Wind speed = 5 m/s, frequency = 1 GHz.	66
4.8	2D RCS of a 13 m high ship on a 402.4 m surface computed using 50 strongest plane wave components of sea scattered incident field. Wind speed = 5 m/s, frequency = 1 GHz.	67
4.9	2D RCS of a 13 m high ship on a 402.4 m surface computed using the numerically exact sea scattered incident field. Wind speed = 5 m/s, frequency = 1 GHz.	69
4.10	2D RCS of a 13 m high ship on a 402.4 m surface computed using GFB for a flat surface and a rough surface. Wind speed = 5 m/s, frequency = 1 GHz. .	70
4.11	2D RCS of a 13 m high ship on a 402.4 m surface computed using GFB for a flat surface and a rough surface. Wind speed = 5 m/s, frequency = 1 GHz. .	71
4.12	2D RCS of a 13 m high ship on a 402.4 m surface computed using GFB for a flat surface and a rough surface. Wind speed = 10 m/s, frequency = 1 GHz. .	73
4.13	2D RCS of a 13 m high ship on a 402.4 m surface computed using GFB for a flat surface and a rough surface. Wind speed = 15 m/s, frequency = 1 GHz. .	74
4.14	2D RCS of a 13 m high ship on a 402.4 m surface computed for flat case, coherent case, and rough surface case. Wind speed = 15 m/s, frequency = 1 GHz.	75
4.15	2D RCS of a 13 m high ship with a 90° hull angle on a 402.4 m surface computed for flat case, coherent case, and rough surface case. Wind speed = 15 m/s, frequency = 1 GHz.	77
4.16	2D RCS of a 9 m high ship on a 402.4 m flat surface computed with the EFIE and physical optics. Frequency = 1 GHz.	78
5.1	2D RCS vs. time for a 13 m high ship on a 402.4 m surface. Elevation angle = 5°, wind speed = 15 m/s, frequency = 1 GHz.	82

5.2	13 m high ship on a 402.4 m time-evolving sea surface. Wind speed = 15 m/s, frequency = 1 GHz.	83
5.3	2D RCS vs. time for a 13 m high ship on a 402.4 m surface at three different wind speeds. Elevation angle = 5°, frequency = 1 GHz.	85
5.4	2D RCS vs. time for a 13 m high ship on a 402.4 m surface. Elevation angle = 5°, wind speed = 15 m/s, frequency = 1 GHz.	86
5.5	2D backscatter vs. time for a 13 m high ship on a 204.8 m surface. Elevation angle = 5°, frequency = 300 MHz.	87
5.6	2D RCS vs. roll angle for a 13 m high ship on a flat surface. Elevation angle = 5°, frequency = 1 GHz.	89
5.7	2D RCS vs. time for a 9 m high low-RCS shape on a 402.4 m surface. Elevation angle = 5°, frequency = 1 GHz.	91
5.8	2D RCS vs. roll angle for a 9 m high low-RCS shape on a flat surface. Elevation angle = 5°, frequency = 1 GHz.	92
6.1	2D RCS vs. time for a 9 m high low-RCS shape on a 402.4 m surface with two different incidence angles. Wind speed = 5 m/s, frequency = 1 GHz. . .	99

Chapter 1

Introduction

1.1 Background

It is of interest to be able to predict and study the radar cross section (RCS) of targets on a rough sea surface using computational electromagnetics (CEM) techniques. Figure 1.1 shows a typical situation where a ship is illuminated by an incident electromagnetic (EM) plane wave, and scatters energy in all directions. It is known that the prevailing sea state (surface roughness) can greatly affect the radar scattering of a ship. The time-changing sea surface may increase or decrease the amount of energy backscattered to the receiver compared to a calm surface, so the RCS likewise changes with time. To predict the effect of the sea surface on the RCS, it is necessary to study how the incident field scatters from the rough sea surface before hitting the ship, and how the subsequent scattering from the ship interacts with the sea surface before propagating back to the receiver.

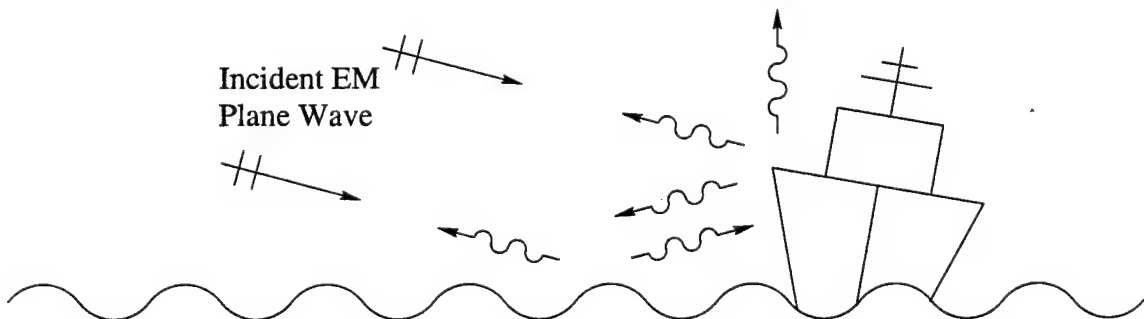


Figure 1.1: Scattering by a ship on a rough sea surface illuminated by an incident EM plane wave.

This report describes the research performed during the first year of Grant No. N00014-98-1-0243 from the Office of Naval Research. The particular focus is to develop algorithms wherein existing CEM tools for predicting the RCS of a target can be modified to account for the presence of the rough sea surface, without having to include the infinitely large rough surface in the computational domain. The first year's study is devoted to a thorough analysis in two dimensions (2D) of the phenomenology associated with the target/rough surface scattering problem. Basic algorithms are developed and tested to provide proofs-of-concept before proceeding to more complex 3D problems. It is noted that the backscatter from the sea surface itself (i.e., "sea clutter") is not of interest here, but has been studied extensively [1, 2]. It is also noted that plane wave incidence is of primary interest here because the definition of RCS assumes that the source is at infinity. For typical surface-to-surface or air-to-surface radar search scenarios, this assumption implies that the downward propagating incident field is locally planar in the vicinity of the target (but the incident field reflected from the sea surface is *not* assumed to be locally planar). The propagation of the EM field from the source to the target, as well as the source and receiver gain, is not included in the plane wave RCS but is included elsewhere in the standard radar equation [2]. The power received by a radar antenna with effective aperture A_e due to scattering from a target with RCS σ is given by

$$P_r = P_t G A_e S^2 \sigma \quad (1.1)$$

where P_t and G are the power and gain of the transmitting antenna, and S is the one-way propagation loss factor. For free space S is $1/4\pi R^2$, where R is the range to the target. For propagation over the sea surface, S is a much more complicated function of distance and is not the subject of this report (although the GFB method of Chapter 2 can compute this function for limited propagation distances).

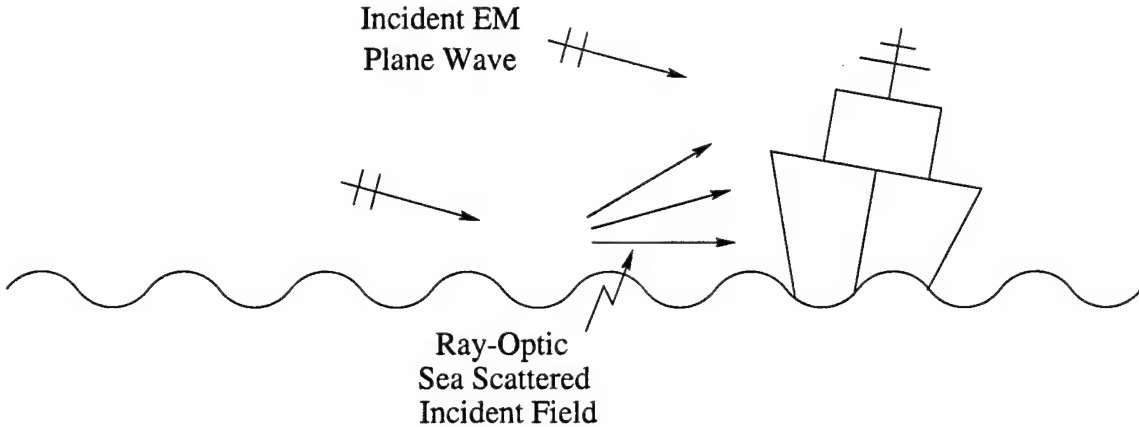


Figure 1.2: Ray-optical characterization of the field illuminating the ship.

1.2 Technical Approach

Since most existing CEM tools for RCS prediction rely on a ray-optical incident field, it is of primary importance to be able to characterize the sea scattered field which illuminates the ship ray-optically, as shown in Figure 1.2. This is especially important for RCS tools which use high-frequency asymptotic methods, such as physical optics (PO), the physical theory of diffraction (PTD), and the uniform theory of diffraction (UTD) [3]. These methods must have a well-defined ray-optical incident field. Furthermore, most ship geometries are very large in terms of the wavelength of the EM field at radar frequencies, so high-frequency methods must usually be used instead of numerical methods which are better suited for smaller problems.

The ray-optical characterization investigated here uses a discrete plane wave expansion for the sea scattered incident field, as shown in Figure 1.3. Once the incident field is characterized ray-optically, the scattering from the ship is found approximately by replacing the rough sea surface with a locally planar surface, as shown in Figure 1.4. This allows the half-space Green's function to be used to compute the scattered field, or equivalently, image theory could be used [4]. (Although image theory is not recommended because including the image of the ship doubles the size of the problem.) The ray-optical expansion of the incident field combined with the local planar approximation for the sea surface effectively decouples the

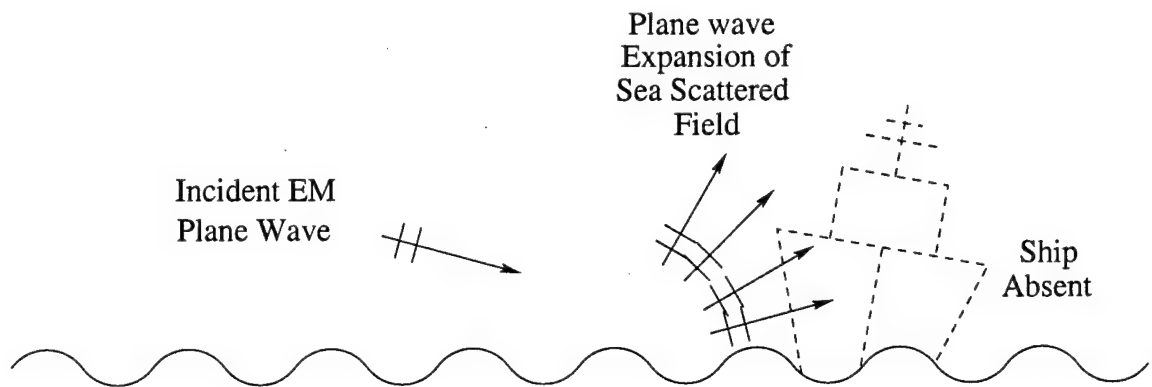


Figure 1.3: Plane wave expansion for the incident and sea scattered field illuminating the ship.

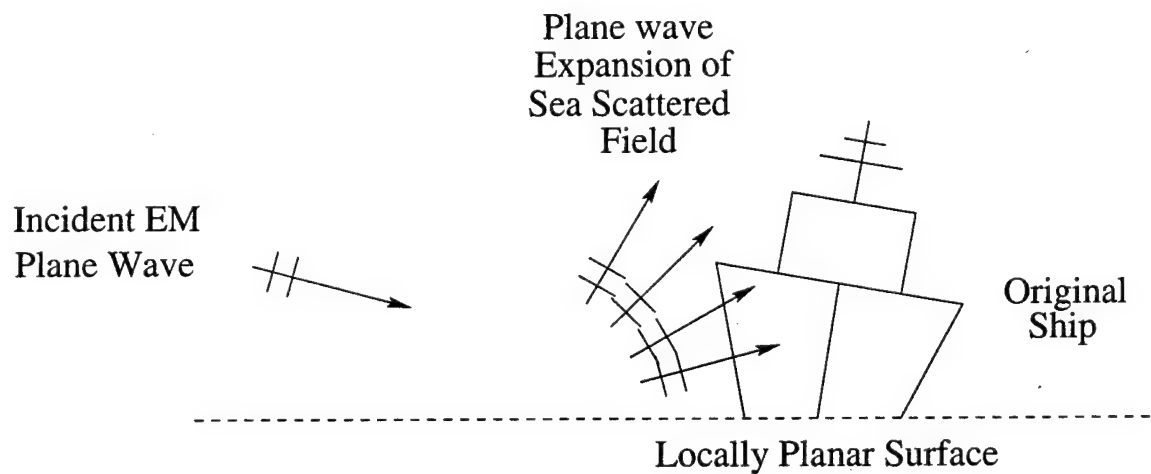


Figure 1.4: Rough sea surface replaced with a locally flat surface.

target scattering problem from the sea surface.

The ship scattered field is found only over the surface of the ship. With this information, the reciprocity theorem [4] is used to compute the backscattered field at the source location. The reciprocity theorem is an exact formulation which gives the target scattered field at the source location in terms of an integral over the surface of the target. The integral is the reaction of the total incident field (including the incident field scattered from the sea surface) with the target scattered field. The only approximation is the use of a locally planar surface in the vicinity of the target to find the scattered field. The use of reciprocity eliminates the need to track the scattered fields back to the source.

Since an approximation is used to find the target scattered fields, the decoupled ray-optical RCS results will not be in perfect agreement with the reference solution which considers the sea surface and target as a whole. However, the goal of this research is not necessarily to predict the exact RCS (which changes with time as the sea surface evolves), but to predict the peak levels and variations in the RCS for a given sea state.

1.3 Organization of Report

Chapter 2 presents an efficient numerical approach termed the *Generalized Forward-Backward* method for computing the scattering from a 2D target on a rough sea surface. This method is used throughout the report to generate reference solutions for the ray-optical algorithms, and to study the scattering properties of different targets under various conditions.

Chapter 3 studies the plane wave spectral properties of the sea scattered field with the target absent. The coherent (time-independent) and incoherent (time-varying) components are clearly delineated. A discrete plane wave expansion for the field which illuminates the target is then proposed. Chapter 4 then uses this expansion as the excitation for finding the scattering from the target in the presence of a locally flat surface, effectively decoupling the target scattering problem from the sea surface. The reciprocity integral is formulated and used to compute the RCS (backscattered field) by integrating only over the target surface.

Chapter 5 investigates the behavior of the RCS as a function of the time-changing sea

surface, and as a function of the roll angle of the target. Different target geometries are studied, including a low-RCS shape. These results give very good insight into the scattering phenomenology, and indicate the usefulness of the ray-optical techniques for predicting peak levels and the pattern variation of the RCS. Finally, conclusions and future directions of research are discussed in Chapter 6.

Chapter 2

The Generalized Forward-Backward Method

2.1 Introduction

In this chapter a generalization of the Forward-Backward (FB) method is presented. This generalization allows us to study the scattering from composite surfaces that can include one or more large arbitrarily shaped obstacles (like a ship or a large rogue breaking wave) on the ocean surface, as shown in Figure 2.1. The conventional FB method is not expected to exhibit convergent behavior for such problems. The new approach, called the *Generalized Forward-Backward* (GFB) method, is based on a combination of the conventional FB method with the Method of Moments (MoM), where the MoM is only applied to the region close to the obstacle. The solution is found through an iterative procedure based on the same general concepts as the FB method, but with some significant differences. The computational cost of the GFB method is similar to the FB solution. It only includes an additional cost associated with the direct MoM solution of a small region containing the obstacle and nearby sea surface. The GFB method is very useful for predicting and studying the EM scattering from targets in the presence of a rough surface. It also used here to provide reference solutions to validate the more approximate ray-optical approaches developed in later chapters.

This chapter is organized as follows: the conventional FB formulation for the solution of the *electric field integral equation* (EFIE) is presented in Section 2.2. Section 2.3 develops the

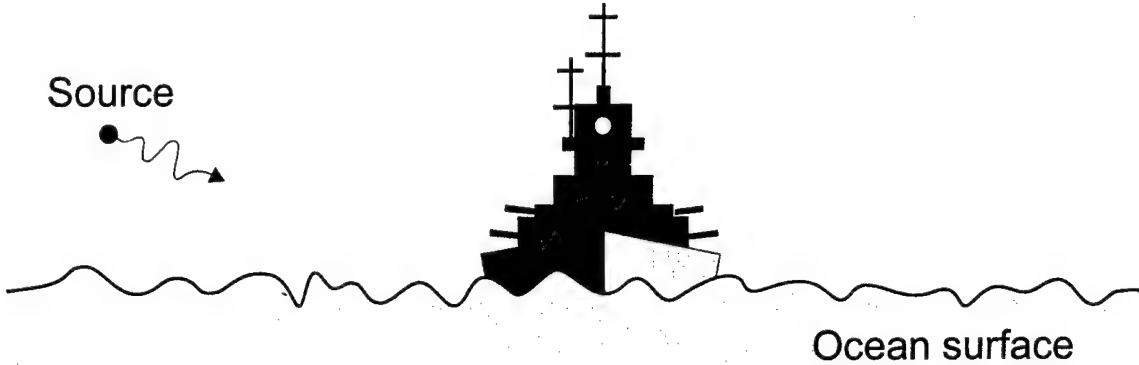


Figure 2.1: A scattering obstacle on an ocean-like surface illuminated by a low-angle incident field.

generalization of the previous method which leads to the new GFB iterative solution. Some numerical results and a summary and conclusions are also included. A Spectral Acceleration of the Generalized Forward-Backward method is presented in Section 2.4. In the rest of the chapter, all the fields and the currents will be assumed to have a time-harmonic dependence of the form $e^{j\omega t}$ which will be suppressed from the field expressions. The radian frequency is ω , and μ and k are the permeability and wavenumber, respectively, of the medium above the rough surface (generally assumed to be free space).

2.2 The Conventional Forward-Backward Method

The magnetic field integral equation (MFIE) for a two-dimensional scattering problem dealing with a one-dimensional rough surface and its solution by the FB method has been presented in [5]. Here we are concerned with the solution of the EFIE in a similar way. The application of the FB method combined with the EFIE has already been done in [6], where a new approach based on the spectral representation of the Green's function accelerates the computation of the forward and backward matrix-vector products. In this section the formulation of the FB method is briefly reviewed, starting with the EFIE followed by a discretization process using the MoM to establish the corresponding matrix equations which will be solved in an iterative way.

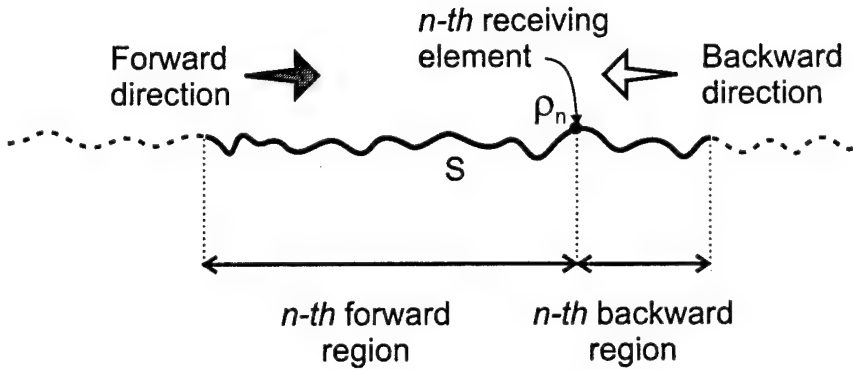
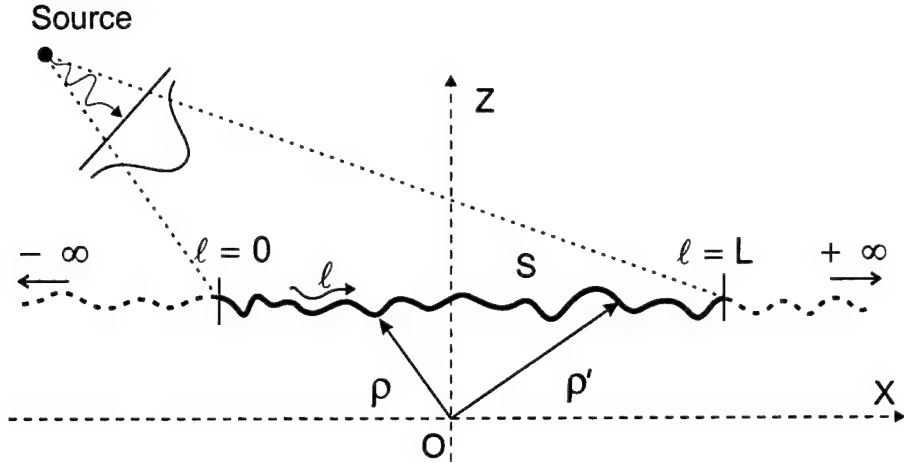


Figure 2.2: (a) Ocean-like surface illuminated by a TM (E_y) polarized near-grazing incident field. (b) Forward and backward regions for the n -th matching point.

Consider a one-dimensional ocean-like surface depicted in Figure 2.2(a). The sea water is modeled as a perfect electrical conductor (PEC), so there is no penetration into the sea surface S . (The method may also be applied to impedance surfaces without loss of generality.) The horizontal and vertical coordinates of this parametric surface are respectively $x(\ell)$ and $z(\ell)$, both functions of the path length ℓ on the surface.

For such a surface, illuminated by a TM (E_y) polarized incident field, the EFIE can be obtained by imposing the tangential electric field boundary condition on the PEC surface S :

$$-\frac{\omega\mu}{4} \int_S J(\rho') H_0^{(2)}(k|\rho - \rho'|) d\ell' = -E^i(\rho) \quad (2.1)$$

where $E^i(\rho)$ is the incident field at a point $\rho \in S$, $\bar{J}(\rho')$ is the induced current and $H_0^{(2)}(k|\rho - \rho'|)$ is the second kind Hankel function with order zero [7]. The current $\bar{J}(\rho')$ radiates in free space and generates the scattered fields. This equation is to be solved through discretization by using the MoM. Although the surface S extends from minus infinity to infinity in x , the incident field is considered to be tapered so that the illuminated rough surface, and thus the integration in (2.1), can be confined to a finite region of length L .

For our purposes, we will apply the most simple formulation of the MoM using a set of N pulse basis functions and point matching weighting at the center of each current element [7]. Typically, about 10 pulse basis functions per wavelength are used. After the discretization process, equation (2.1) is transformed into a matrix equation:

$$\bar{\bar{Z}} \cdot \bar{I} = \bar{V} \quad (2.2)$$

The elements of the impedance matrix $\bar{\bar{Z}}$ are given by:

$$Z_{mn} = \begin{cases} -\frac{\omega\mu}{4} \left[1 - j\frac{2}{\pi} \ln\left(\frac{\gamma k \Delta\ell}{4e}\right) \right] \Delta\ell & m = n \\ -\frac{\omega\mu}{4} H_0^{(2)}(k|\rho_m - \rho_n|) \Delta\ell & m \neq n \end{cases} \quad (2.3)$$

where γ is the Euler constant 1.871, $\Delta\ell$ is the width of the pulse basis and ρ_n is the position vector of the n^{th} pulse basis center. Matrix \bar{I} is a column vector which contains the unknown coefficients $\bar{I} = \{I_n | n = 1, \dots, N\}$ that are used to approximate the current:

$$J(\rho') \approx \sum_{n=1}^N I_n P_n(\rho') \quad (2.4)$$

where $P_n(\rho')$ denotes the unit pulse basis function centered at ρ_n . The column vector \bar{V} elements are given by minus the incident field at the matching points:

$$V_n = -E^i(\rho_n) \quad (2.5)$$

For brevity, the expressions have been developed only for the TM (E_y) polarization. Similar equations can be easily derived for the TE polarization. Nevertheless, the FB method that will be described below is applicable to both polarizations.

The FB method will be formulated using the matrix notation of (2.2), instead of the integral equation (2.1). First, consider the following decomposition applied over the matrices involved in equation (2.2):

$$\bar{I} = \bar{I}^f + \bar{I}^b \quad (2.6)$$

$$\bar{Z} = \bar{Z}^f + \bar{Z}^s + \bar{Z}^b \quad (2.7)$$

where \bar{I}^f is the forward component (i.e. the current contribution due to the waves propagating in the forward direction), \bar{I}^b is the backward component (or current contribution due to the waves propagating in the backward direction), and \bar{Z}^f , \bar{Z}^s and \bar{Z}^b are respectively the lower triangular part, the diagonal part (self impedance terms) and the upper triangular part of \bar{Z} .

Equation (2.2) can now be split into forward-propagation and backward-propagation matrix equations, respectively, as follows:

$$\bar{Z}^s \cdot \bar{I}^f = \bar{V} - \bar{Z}^f \cdot (\bar{I}^f + \bar{I}^b) \quad (2.8)$$

$$\bar{Z}^s \cdot \bar{I}^b = -\bar{Z}^b \cdot (\bar{I}^f + \bar{I}^b) \quad (2.9)$$

where (2.9) has been assumed by definition. It can be seen that, for a given n^{th} matching point located at ρ_n , the right hand side (RHS) of (2.8) contains the incident field and the contribution of the current elements located in the front of this receiving element, which corresponds to the n^{th} forward region in Figure 2.2(b). Likewise, the RHS of (2.9) contains the influence of the current elements in the rear of the receiving element, so it represents the n^{th} backward region contribution as in Figure 2.2(b). From this it is clear that *the MoM current elements must be numbered sequentially as a function of increasing x in the FB method*, i.e.,

$$x(\rho_{n-1}) < x(\rho_n) < x(\rho_{n+1}). \quad (2.10)$$

Equations (2.8) and (2.9) can be solved iteratively, where the currents in the i^{th} stage of the algorithm $(\bar{I}^{f,(i)}, \bar{I}^{b,(i)})$ are obtained as:

$$(\bar{Z}^s + \bar{Z}^f) \cdot \bar{I}^{f,(i)} = \bar{V} - \bar{Z}^f \cdot \bar{I}^{b,(i-1)} \quad (2.11)$$

$$\left(\overline{\overline{Z}}^s + \overline{\overline{Z}}^b \right) \cdot \overline{I}^{b,(i)} = - \overline{\overline{Z}}^b \cdot \overline{I}^{f,(i)} \quad (2.12)$$

The algorithm starts with $\overline{I}^{b,(0)} = 0$. It must be noticed that the matrices involved in this iterative process do not need to be factorized or inverted, because $\overline{\overline{Z}}^s + \overline{\overline{Z}}^f$ is a lower triangular matrix, and $\overline{\overline{Z}}^s + \overline{\overline{Z}}^b$ is an upper triangular matrix; so, the equations (2.11) and (2.12) can be solved for $\overline{I}^{f,(i)}$ and $\overline{I}^{b,(i)}$ by forward and backward substitution, respectively. The convergence has been shown to be extremely rapid for moderately rough surfaces, generally requiring fewer than 10 iterations. However, it should be noted that the algorithm may become unstable for re-entrant surfaces, i.e., for surfaces where $x(\rho_{n+1}) \leq x(\rho_n)$ for one or more points ρ_n . This violates the sequential number requirement of (2.10). The GFB method developed next overcomes this limitation for the case of one or more arbitrarily shaped scattering obstacles on the surface.

2.3 The Generalized Forward-Backward Method

2.3.1 Method Description

Consider now the composite problem depicted in the Figure 2.3, where one or more PEC obstacles (like a ship or large rogue breaking wave) are included in the surface contour S . For this kind of problem the conventional FB method does not exhibit convergent behavior, because the presence of the obstacle highly disturbs the propagation process assumed by the conventional FB method. There are strong interactions between the obstacle and the nearby ocean-like surface, and within the obstacle itself, all of which may not be taken into account with the conventional formulation involved in the standard FB method.

In order to overcome this drawback, a new method called the *Generalized Forward Backward* (GFB) method is presented in this chapter. The GFB method consists on a generalization of the conventional FB approach which enhances the scope of application of the previous method to composite scattering problems as the one depicted in Figure 2.3. This method is based on the same general concepts previously stated for the FB method, but includes some significant differences mainly in the decomposition of the matrix $\overline{\overline{Z}}$ that will

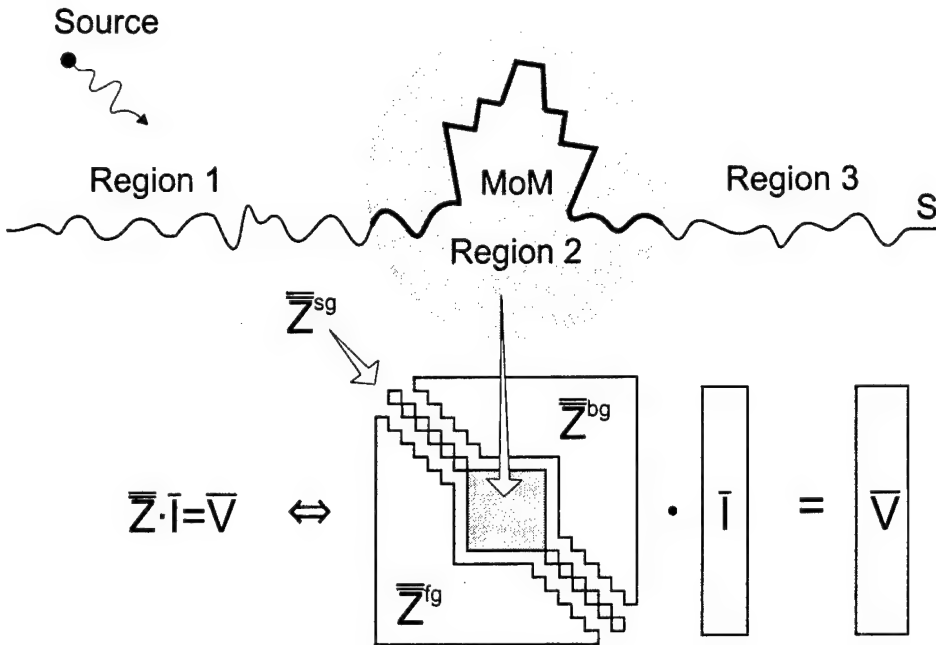


Figure 2.3: Composite problem and matrix decomposition in the GFB method.

be detailed next. For the sake of simplicity, the GFB formulation will be presented for a simple problem consisting of a sea surface containing only one obstacle (see Figure 2.3); the extension of the formulation to several obstacles is obvious as will be seen later.

Again starting with equation (2.2), which has been obtained from (2.1) after the MoM discretization process. In the same way as done in the FB method, the current is expressed as the sum of two contributions (*forward* and *backward*):

$$\bar{I} = \bar{I}^f + \bar{I}^b \quad (2.13)$$

but now the impedance matrix is split in a different way:

$$\bar{Z} = \bar{Z}^{fg} + \bar{Z}^{sg} + \bar{Z}^{bg} \quad (2.14)$$

where the \bar{Z}^{sg} matrix is the diagonal part of \bar{Z} with an additional block including the impedance sub-matrix corresponding to the ship and near-field sea region (Region 2 in Figure 2.3); while \bar{Z}^{fg} and \bar{Z}^{bg} are respectively the lower triangular part and the upper triangular part of \bar{Z} but excluding the matrix \bar{Z}^{sg} , as illustrated in Figure 2.3. With this decompo-

sition, matrix $\overline{\overline{Z}}^{sg}$ contains both the self (diagonal) terms and the interaction of the whole obstacle and nearby sea region together.

Then, the original system is transformed in a similar way as in the conventional FB method, yielding the following matrix equations:

$$\overline{\overline{Z}}^{sg} \cdot \overline{I}^f = \overline{V} - \overline{\overline{Z}}^{fg} \cdot (\overline{I}^f + \overline{I}^b) \quad (2.15)$$

$$\overline{\overline{Z}}^{sg} \cdot \overline{I}^b = -\overline{\overline{Z}}^{bg} \cdot (\overline{I}^f + \overline{I}^b) \quad (2.16)$$

which can be iteratively solved for $\overline{I}^{f,(i)}$ and $\overline{I}^{b,(i)}$ as:

$$\left(\overline{\overline{Z}}^{sg} + \overline{\overline{Z}}^{fg} \right) \cdot \overline{I}^{f,(i)} = \overline{V} - \overline{\overline{Z}}^{fg} \cdot \overline{I}^{b,(i-1)} \quad (2.17)$$

$$\left(\overline{\overline{Z}}^{sg} + \overline{\overline{Z}}^{bg} \right) \cdot \overline{I}^{b,(i)} = -\overline{\overline{Z}}^{bg} \cdot \overline{I}^{f,(i)} \quad (2.18)$$

starting with $\overline{I}^{b,(0)} = 0$ in (2.17).

The solution of (2.17) and (2.18) differs from (2.11) and (2.12) because neither $\overline{\overline{Z}}^{sg} + \overline{\overline{Z}}^{fg}$ nor $\overline{\overline{Z}}^{sg} + \overline{\overline{Z}}^{bg}$ are triangular matrices. Nevertheless, the equations can also be easily solved by combining forward or backward substitution together with the direct factorization of the square block of $\overline{\overline{Z}}^{sg}$ whose dimension depends only on the number of current elements in Region 2, namely the ship and nearby sea (see Fig. 2.3). A description of the solution procedure can be found in the next section. Qualitatively, the solution proceeds as follows.

For each iteration i :

1. Find $\overline{I}^{f,(i)}$ over Region 1 using the forward propagation principle.
2. Direct solve for $\overline{I}^{f,(i)}$ over Region 2 using the fields radiated by the Region 1 currents plus the incident field as excitation.
3. Find $\overline{I}^{f,(i)}$ over Region 3 by the forward propagation principle.
4. Find $\overline{I}^{b,(i)}$ over Region 3 by the backward propagation principle.
5. Direct solve for $\overline{I}^{b,(i)}$ over Region 2 using the fields radiated by the Region 3 currents.

6. Find $\bar{I}^{b,(i)}$ over Region 1 using the backward propagation principle.

The computational cost of the GFB method is practically the same as the conventional FB method. It only has the additional computational cost of factorizing the square block of $\bar{\bar{Z}}^{sg}$ which corresponds to the MoM matrix of Region 2. Nevertheless, due to the limited size of this block matrix, its factorization can be performed once and stored, thus reducing the computational work in subsequent iterations and for other excitations. So, it can be concluded that the GFB method has a computational cost of $O(N^2)$ per iteration as in the FB method [6]. The storage requirement is $O(N)$ to store the iterated currents as in the FB method, with the additional storage of a square matrix of size $M \times M$, where M is the number of current elements included in the MoM region (Region 2 in Figure 2.3). Generally, $M \ll N$, but the $O(M^2)$ matrix storage requirement may be comparable to the $O(N)$ storage of the currents. It is noted that the $O(N)$ storage requirement assumes that the full $\bar{\bar{Z}}$ matrix is not stored, so it is necessary to recompute the matrix elements at each iteration (except for the inner MoM matrix associated with Region 2). However, the simple closed form of the matrix elements allows them to be computed very quickly, and the number of iterations is usually very small (typically less than 10). Finally, it is noted that the new spectral technique introduced in [6] for accelerating the FB method may likewise be used to accelerate the GFB method, with some minor modifications as described in Section 2.4.

2.3.2 Solving equations (2.17) and (2.18)

In this section a description of the procedure used to solve equations (2.17) and (2.18) is presented. It must be pointed that neither $\bar{\bar{Z}}^{sg} + \bar{\bar{Z}}^{fg}$ nor $\bar{\bar{Z}}^{sg} + \bar{\bar{Z}}^{bg}$ are triangular matrices; nevertheless, these equations can be easily solved by combining forward or backward substitution together with the direct factorization of a square block sub-matrix, whose dimension is just the extent of the MoM region. For brevity, we will explain only the resolution of (2.17) which concerns the matrix $\bar{\bar{Z}}^{sg} + \bar{\bar{Z}}^{fg}$. Equation (2.18) can be solved in a similar way.

Equation (2.17) has the general form

$$\bar{\bar{A}} \cdot \bar{x} = \bar{b} \quad (2.19)$$

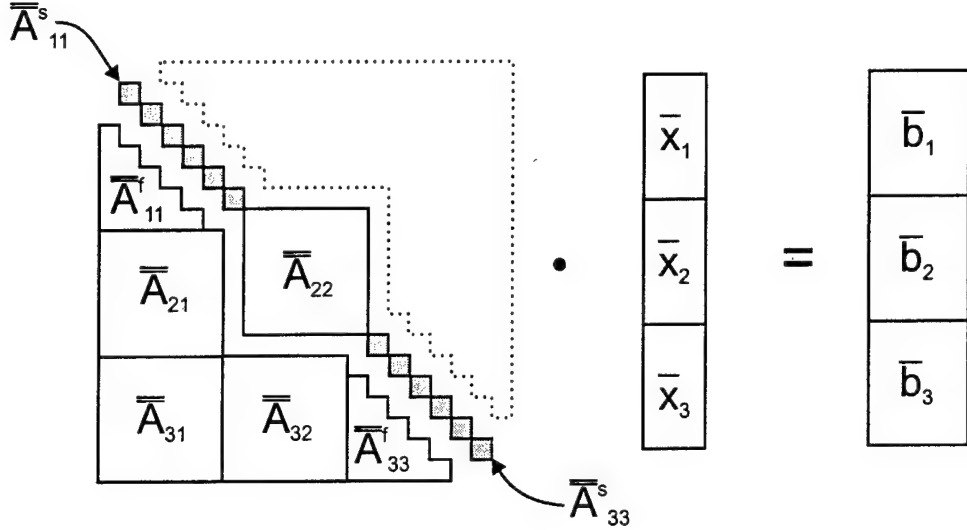


Figure 2.4: Block decomposition of a “quasi” lower triangular matrix.

where $\bar{A} = \bar{Z}^{sg} + \bar{Z}^{fg}$, $\bar{x} = \bar{I}^{f,(i)}$, and $\bar{b} = \bar{V} - \bar{Z}^{fg} \cdot \bar{I}^{b,(i-1)}$. \bar{A} is a “quasi” lower triangular matrix as depicted in Figure 2.4. In order to solve these equations in an efficient way, the matrices \bar{A} , \bar{x} and \bar{b} of (2.19) are subdivided into blocks as shown in Figure 2.4. Thus (2.19) can be expressed in terms of the blocks as follows:

$$(\bar{A}_{11}^s + \bar{A}_{11}^f) \cdot \bar{x}_1 = \bar{b}_1 \quad (2.20)$$

$$\bar{A}_{21} \cdot \bar{x}_1 + \bar{A}_{22} \cdot \bar{x}_2 = \bar{b}_2 \quad (2.21)$$

$$\bar{A}_{31} \cdot \bar{x}_1 + \bar{A}_{32} \cdot \bar{x}_2 + (\bar{A}_{33}^s + \bar{A}_{33}^f) \cdot \bar{x}_3 = \bar{b}_3 \quad (2.22)$$

The solution is then obtained as follows:

1. Equation (2.20) is a lower triangular matrix, so \bar{x}_1 can be easily obtained by forward-substitution.
2. Once \bar{x}_1 is has been calculated, \bar{x}_2 can be obtained from (2.21) by the direct solution of:

$$\bar{A}_{22} \cdot \bar{x}_2 = (\bar{b}_2 - \bar{A}_{21} \cdot \bar{x}_1) \quad (2.23)$$

LU decomposition may be used so that \bar{A}_{22} needs to be factorized only once for a given Region 2 geometry. The factorized matrix may then be saved for subsequent iterations

and for other excitations.

3. Finally, once \bar{x}_1 and \bar{x}_2 have been calculated, \bar{x}_3 can be obtained from (2.22) again by forward substitution from:

$$\left(\bar{\bar{A}}_{33}^s + \bar{\bar{A}}_{33}^f \right) \cdot \bar{x}_3 = \bar{b}_3 - \bar{\bar{A}}_{31} \cdot \bar{x}_1 - \bar{\bar{A}}_{32} \cdot \bar{x}_2 \quad (2.24)$$

because $\bar{\bar{A}}_{33}^s + \bar{\bar{A}}_{33}^f$ is a lower triangular matrix.

A similar procedure is applied for the solution of equation (2.18). The only difference is that in this case we will define upper triangular component matrices that can be solved by back substitution.

2.3.3 Numerical results

In this section results are presented to validate the convergence and accuracy of the new GFB method, and to investigate some of the effects of a random rough surface on the backscatter pattern of a target on the surface. In the following, the sea surfaces are randomly generated realizations of a Gaussian random process with a Pierson-Moskowitz spectrum for a given wind speed [8]. The excitation antenna is a linear array of 15 equally spaced electric line sources with a cosine aperture weighting function. This source array produces a 9° main beam with low sidelobes. (Low sidelobes are important so that the sea surface near the source is not strongly illuminated.) The polarization is horizontal, as in the derivation for the TM EFIE earlier.

Figure 2.5 shows the source location and pattern function relative to a PEC ship-like target on a PEC rough sea surface. For this example, the sea surface is 204.8 m in length, the wind speed is 15 meters per second (m/s), and the wavelength is 1 m. The source is 10 m high on the extreme left, and points horizontally. The MoM region shown within the dashed vertical lines contains the ship and 5 m of sea surface on either side. For validating the new method with this example, the current obtained with GFB is compared with the solution given by MoM applied to the whole surface in Figure 2.6, as a function of the pulse basis

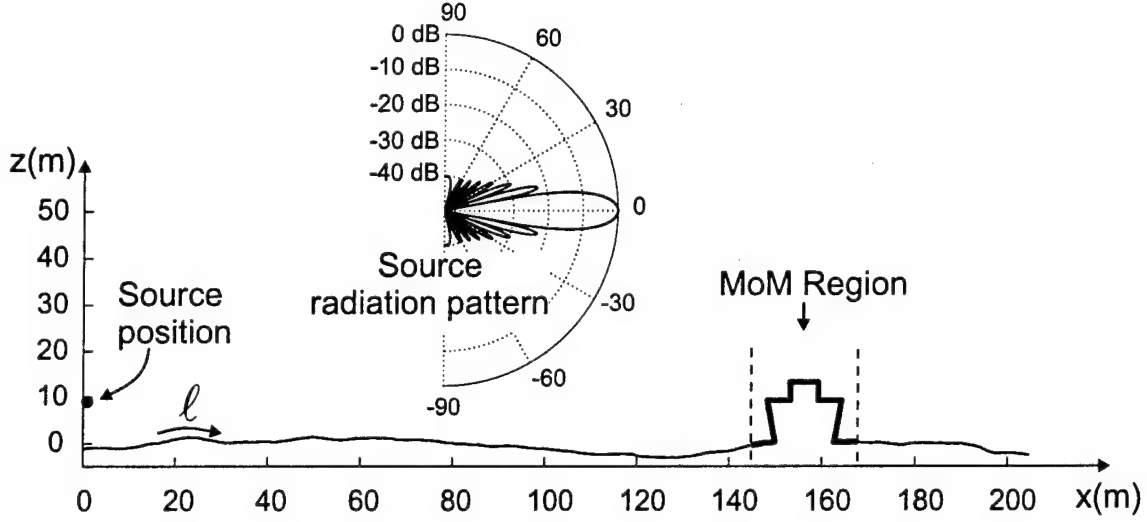


Figure 2.5: Source and target geometry on a sea surface with wind speed 15 m/s. Units are in meters.

index number. For the GFB results, the MoM region is within the outer dashed vertical lines, and the ship is within the inner dashed lines. 10 iterations are used. The difference between the two currents is shown in the Figure 2.7. After only 10 iterations, the maximum difference in the currents is on the order of 10^{-5} .

The residual error is used for monitoring the convergence of the GFB in terms of the number of iterations. The residual error vector after the i^{th} iteration is defined as:

$$\bar{r}^{(i)} = \bar{V} - \bar{Z} \cdot \bar{I}^{(i)}. \quad (2.25)$$

By substituting equations (17) and (18) in (2.25), the residual error vector can be evaluated in a more efficient way as:

$$\bar{r}^{(i)} = \bar{Z}^{fg} \cdot \left[\bar{I}^{b(i-1)} - \bar{I}^{b(i)} \right]. \quad (2.26)$$

The *Residual Error* is defined as:

$$\text{Residual Error} = \frac{\|\bar{r}^{(i)}\|}{\|\bar{V}\|} \quad (2.27)$$

where $\|\bar{r}^{(i)}\|$ denotes the vector norm. The residual error of the GFB for this example is shown in Figure 2.8; it decreases exponentially with the number of iterations. The residual

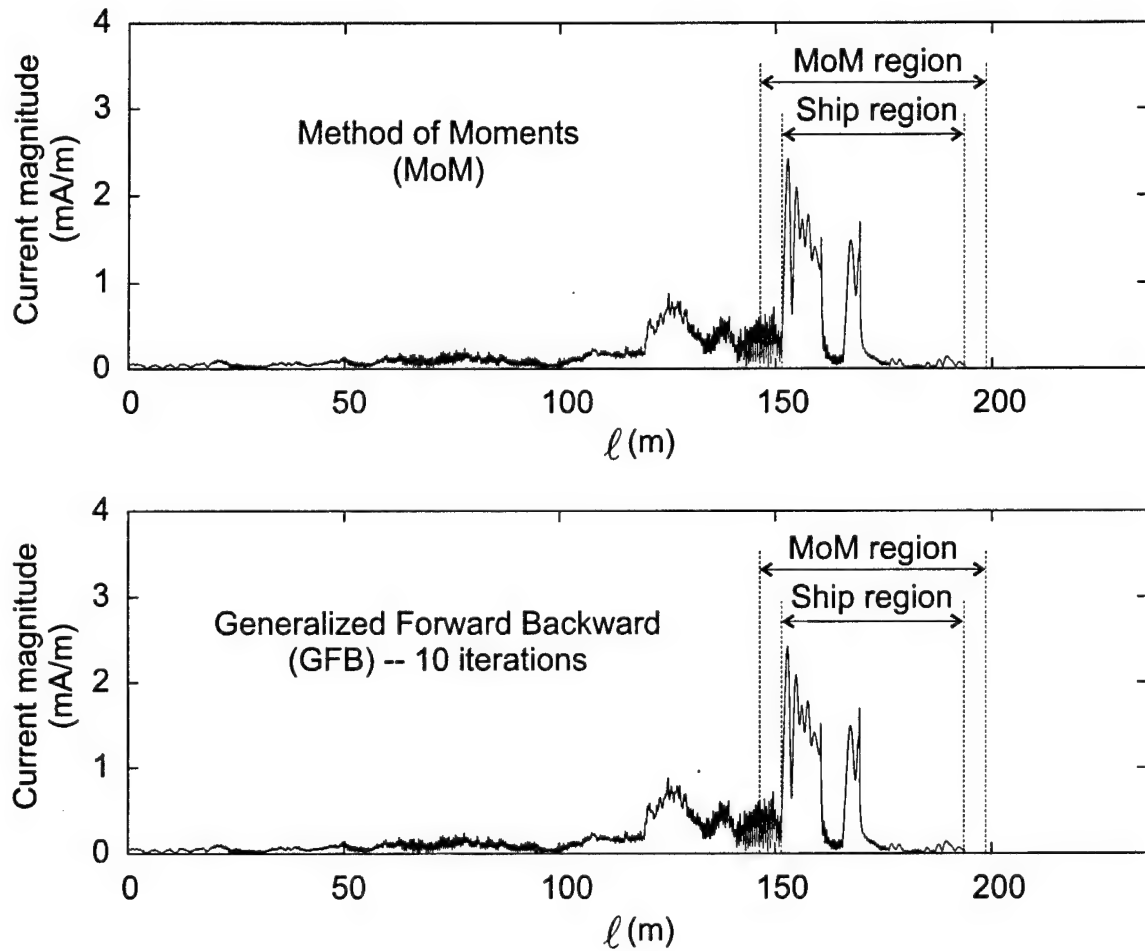


Figure 2.6: Magnitude of the currents as a function of index number (with 10 segments/ λ):
 (a) the GFB Method (10th iteration) and (b) Moment Method.

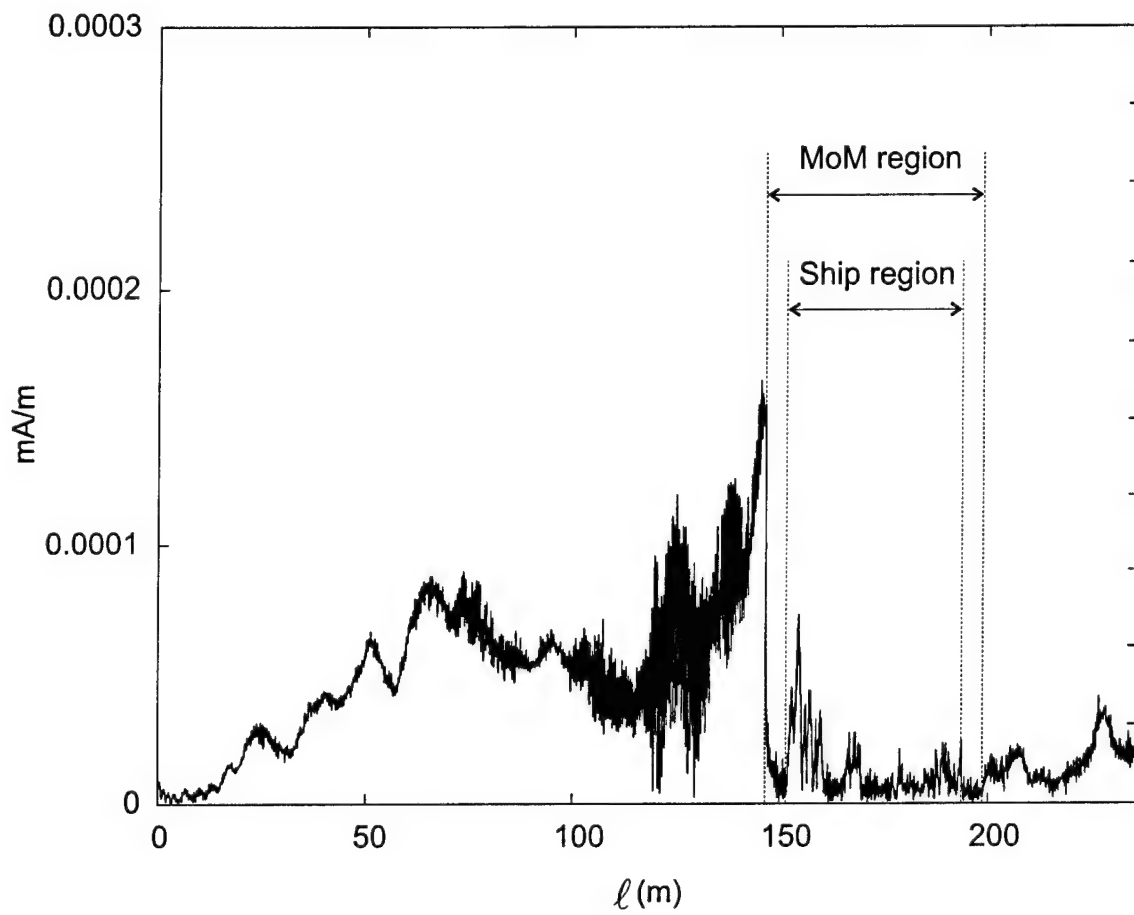


Figure 2.7: Magnitude of the difference between GFB and MoM currents as a function of index number.

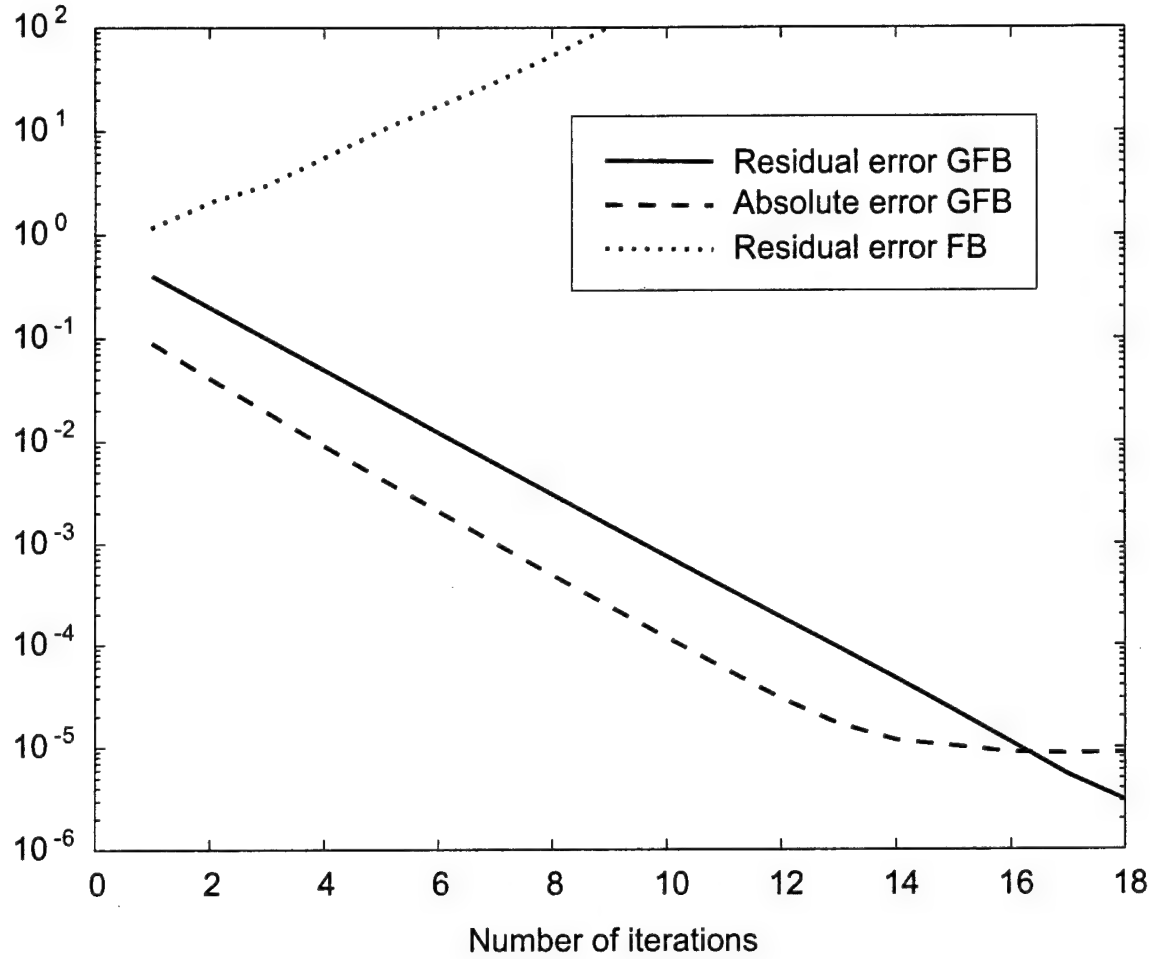


Figure 2.8: Residual and absolute errors versus the number of iterations.

error of the FB method has also been plotted, and as for reasons explained in Section 3, the FB method generally cannot achieve a convergent solution when an obstacle is present in the sea surface. Figure 2.8 also plots the *Absolute Error* of the GFB method, defined by

$$\text{Absolute Error} = \frac{\|\bar{I}^{(i)} - \bar{I}_{MoM}\|}{\|\bar{I}_{MoM}\|} \quad (2.28)$$

where \bar{I}_{MoM} is the MoM reference solution for the currents. It is seen that the absolute error also falls exponentially, but after about 14 iterations it levels out. This is often a characteristic of iterative methods in general, and is caused by the finite numerical precision of the computer. To judge convergence of the solution, the residual error is a very good indicator and is easy to compute at each iteration using (2.26) and (2.27). Halting the

algorithm when the residual error reaches about 10^{-2} or 10^{-3} yields very accurate scattering results. For this example, 6-10 iterations is found to be quite sufficient.

To investigate the scattering behavior of a ship on a rough surface, the geometry of Figure 2.9 is considered. The ship and the source are the same as in Figure 2.5, but the length of the sea surface is 409.6 m, and the source antenna moves in elevation at a constant distance from the ship to generate a backscatter pattern (i.e., the pattern of the scattered field at the source position as a function of elevation angle). The antenna beam points directly at the ship, and the source starts at a height of 10 m above the surface. The wavelength is again 1 m. Two different randomly generated sea surfaces at the same wind speed (15 m/s) are shown in the figure. It is noted that the ship remains upright and does not roll with the waves in the results that follow.

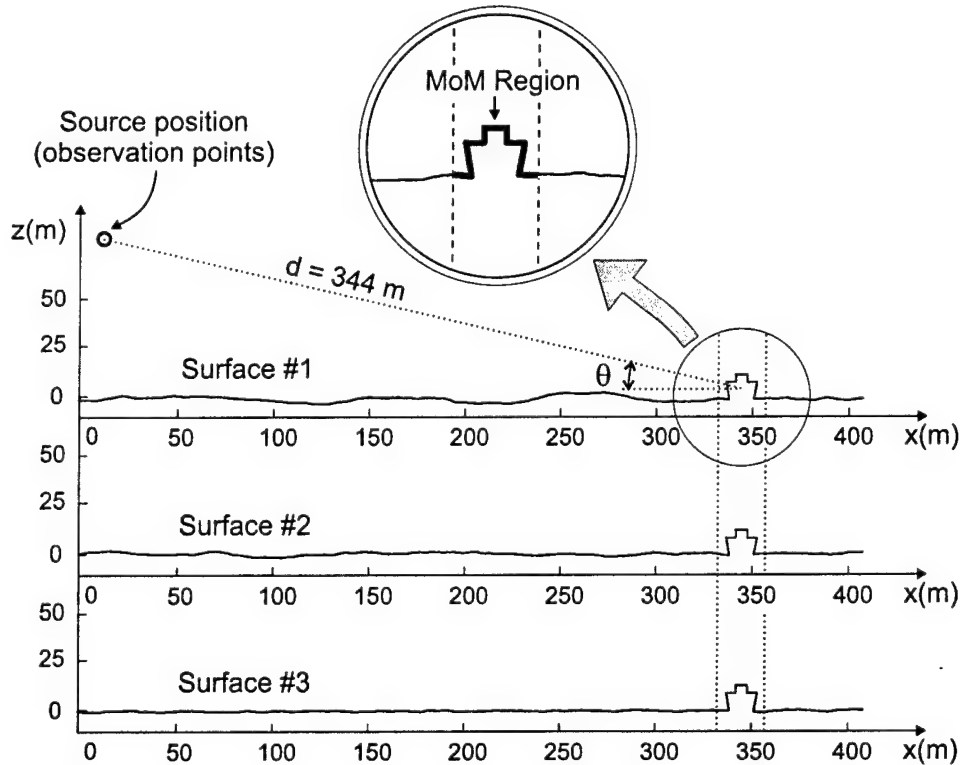


Figure 2.9: Geometry for backscatter patterns. In the pattern plots, continuous line represents Surface #1 and dotted line Surface #2. (The ship is the same in both cases.) Wind speed = 15 m/s.

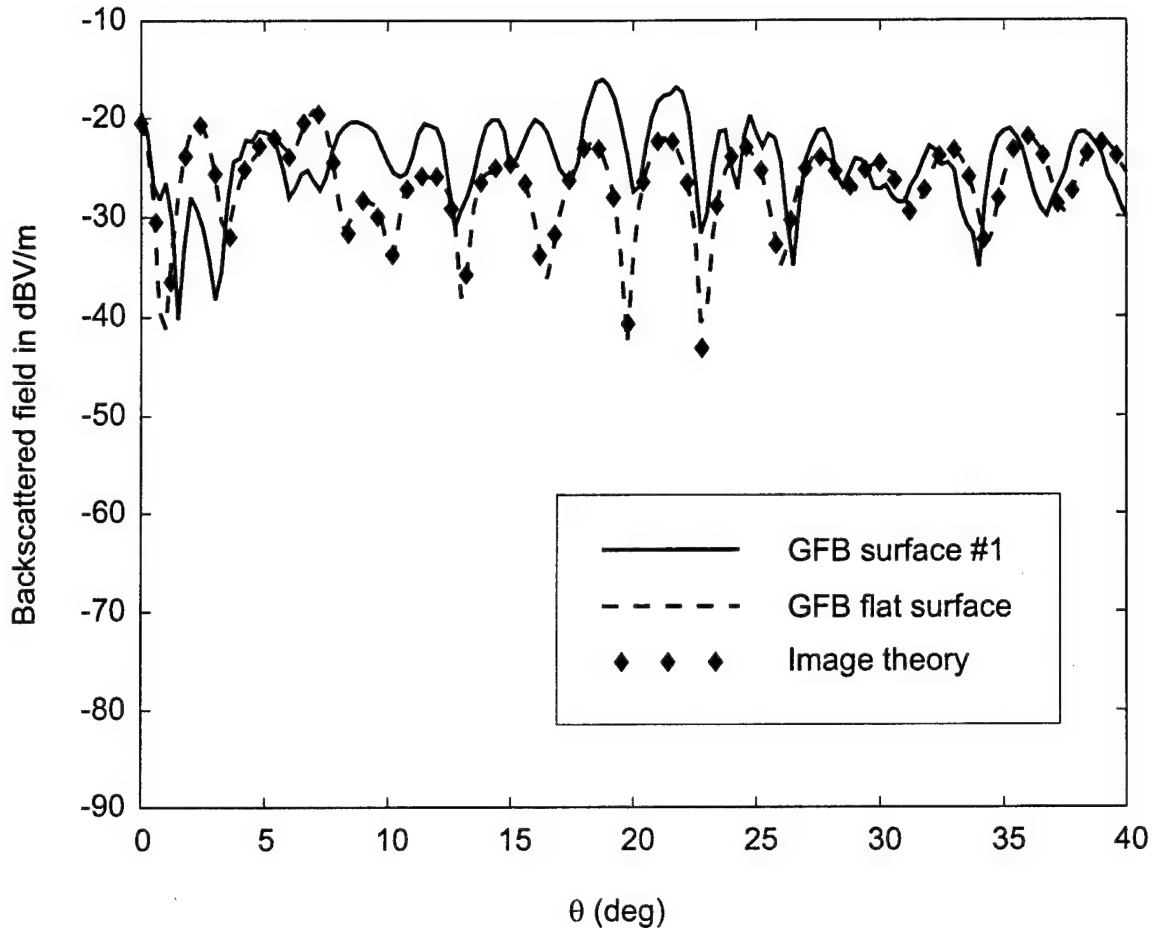


Figure 2.10: Comparison between the backscattered field of a ship on a rough surface (Surface #1) and on a flat surface. A reference solution for an infinite flat surface found using MoM and image theory is also included.

Figure 2.10 shows the backscatter patterns for the ship on Surface #1, and for the ship on a finite flat surface of the same length for comparison. Also shown is a reference MoM solution for the ship on an infinite flat surface found using image theory [4]. The very close agreement between the image theory result and the GFB result for the finite flat surface show that end point effects are negligible, and further validates the GFB method for scattering problems. The figure also shows that the rough surface greatly affects the backscatter pattern compared with a flat surface.

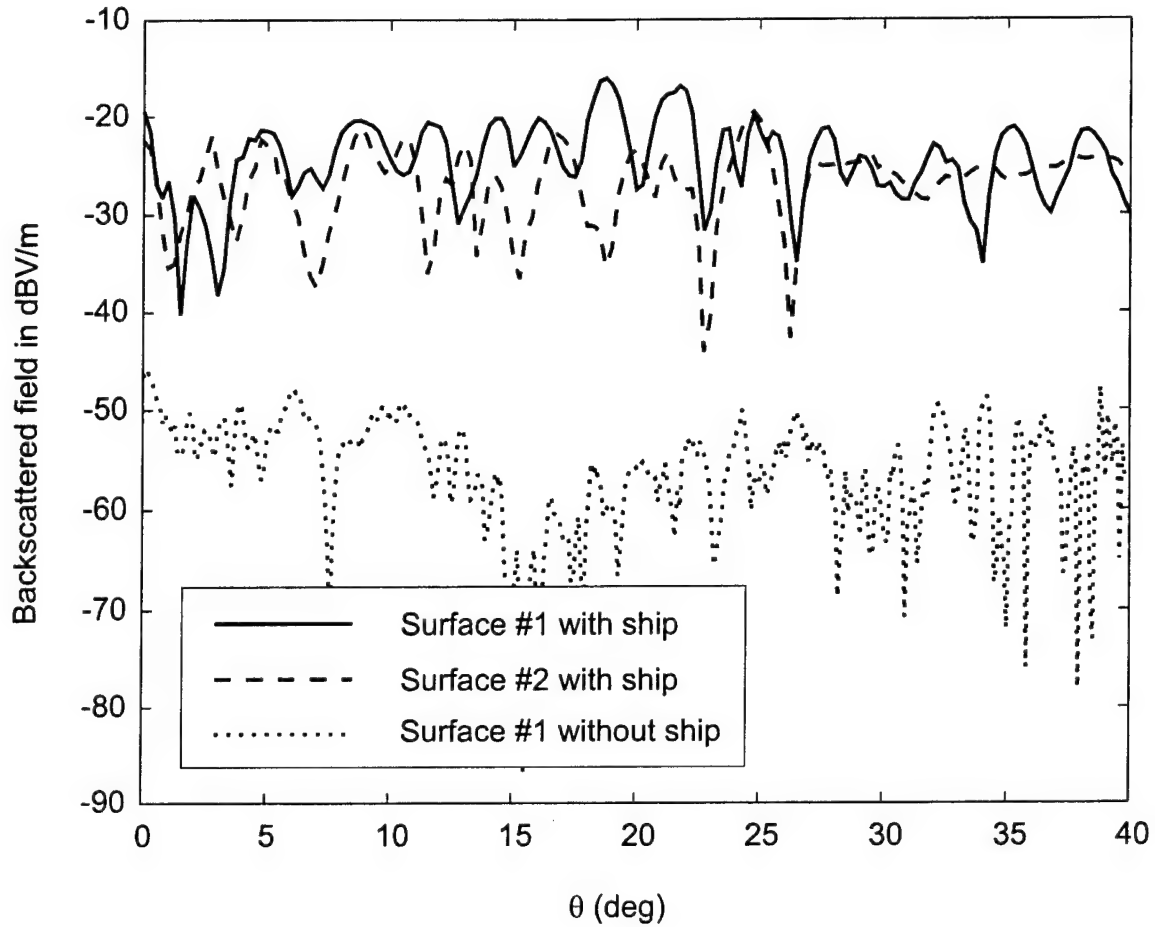


Figure 2.11: Comparison between the backscattered field for Surfaces #1 and #2 with the ship. The backscattering from surface #1 without the ship is also plotted.

Figure 2.11 shows the backscatter patterns for the ship on the two rough surfaces depicted in Figure 2.9. It is seen that the patterns are significantly different for these two surfaces which have the same roughness scale, although it could be argued that the patterns are at about the same average level. The backscatter due to Surface #1 without the ship is also plotted to show the level of the background clutter for this wind speed. The clutter level computed here is quite low, but it should be mentioned that this ocean model does not include the effects of breaking waves which generally dominate the backscatter return from the ocean in the absence of a ship. In fact, the clutter level in Figure 2.11 is due almost entirely to direct reflection of the downward pointing low sidelobe beams. However, as noted

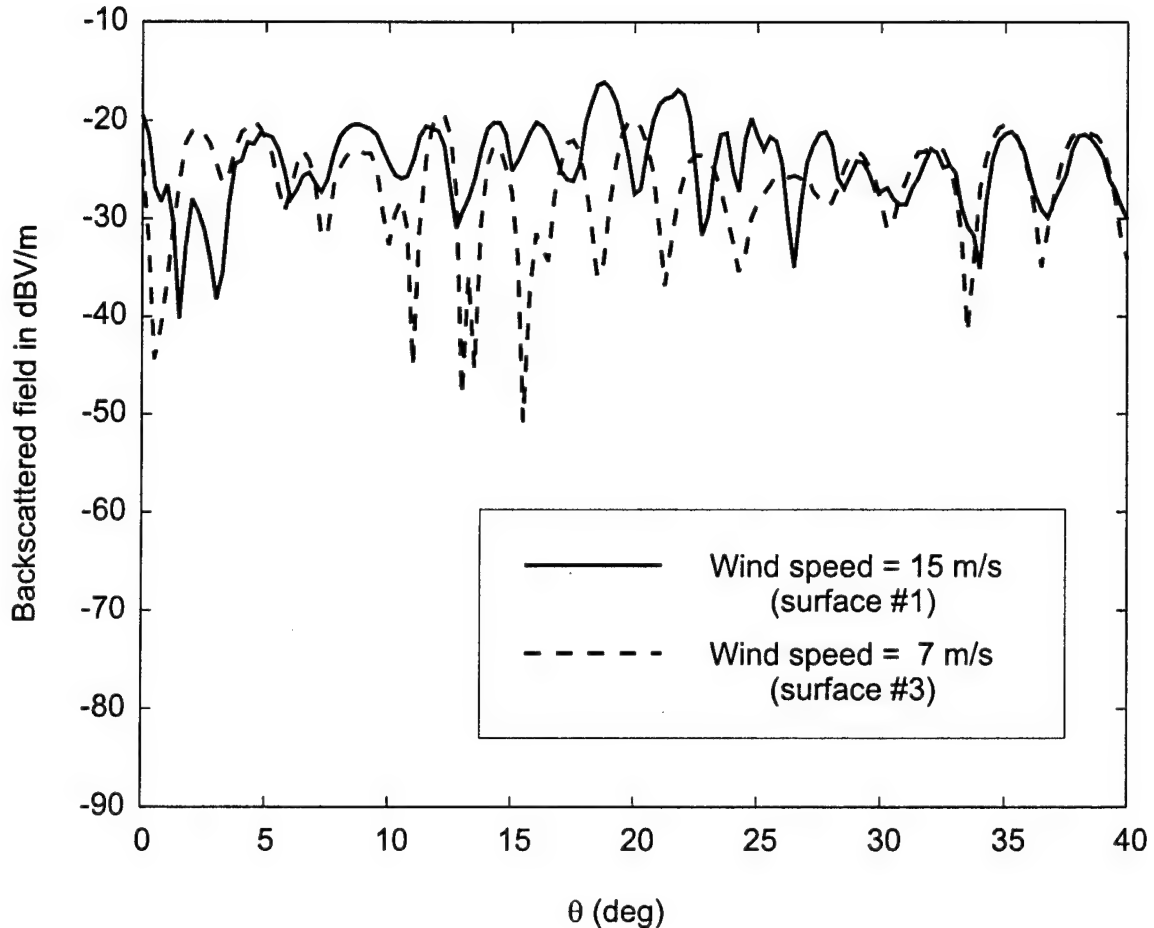


Figure 2.12: Comparison between the backscattered field for a ship on Surface #1 and on a randomly generated surface with wind speed = 7 m/s.

earlier, the GFB method could be used to analyze an isolated breaking wave in the presence of an otherwise smoothly varying ocean surface simply by replacing the ship geometry with that of the wave.

Figure 2.12 shows the backscatter patterns for the ship on Surface #1 and on a randomly generated surface with wind speed 7 m/s. Again, the patterns are significantly different, although they are at about the same average level. Furthermore, the 7 m/s result does not appear any closer to the flat surface result of Figure 2.10 than the 15 m/s result, even though the roughness scale is smaller. Any further conclusions about these results requires a more thorough statistical study, which is the subject of Chapter 5.

2.3.4 Discussion and Conclusions

The new approach has been shown to provide very accurate results and maintains the same fast convergence (usually in less than 10 iterations) and $O(N^2)$ computational cost associated with the conventional FB solution. The storage requirement is $O(N + M^2)$, where M is the number of basis functions used in the small MoM region around the target. Nevertheless, the $O(N^2)$ computational cost makes the method inefficient for very large surfaces. In order to overcome this limitation the GFB could be combined with modern integral equation acceleration algorithms such as the asymptotic fast multipole method [9], or the novel spectral acceleration method [6] which could reduce the computational cost to $O(N)$. The improvement of the GFB method, combining it with novel acceleration algorithms, will be addressed in the next section.

The numerical results show that different random ocean surfaces greatly affect the backscatter patterns of a ship-like target, although the patterns tend to have about the same average level. It is difficult to make any further conclusions at this point about how the wind speed affects the backscatter patterns. One would expect, for example, that higher wind speeds (and therefore, larger roughness scales) would cause a larger variance in the backscatter. A more thorough statistical investigation is necessary, which is the subject of Chapter 5. The purpose of the GFB method introduced here is to provide a numerical tool for studying this class of scattering problems, and to provide a reference solution for more approximate techniques discussed later in this report.

2.4 Spectral Acceleration for the GFB

In the Generalized Forward-Backward method, the direct computation of the matrix-vector products, included in (2.17) and (2.18), $\overline{\overline{Z}}^{fg} \cdot (\overline{I}^{f,(i)} + \overline{I}^{b,(i-1)})$ and $\overline{\overline{Z}}^{bg} \cdot (\overline{I}^{f,(i)} + \overline{I}^{b,(i)})$ implies a computational cost of $O(N^2)$. In [6] a spectral acceleration for the FB was introduced. This acceleration reduces the computational cost of these products to $O(N)$, and is modified here in order to apply it in the GFB method. In this section the modifications are described

and, for clarity, the description is divided into 3 parts which correspond to the 3 regions in Figure 2.3. For brevity, only the acceleration for the *forward* propagation is included; the formulation for the *backward* propagation is obtained in the same way.

2.4.1 Implementation of the Spectral Acceleration

Region #1

In order to evaluate $\bar{I}^{f,(i)}$ in (2.17) at the points in Region #1 ($n < N_1$), a matrix-vector product of the form

$$E_f(\vec{\rho}_n) = \sum_{m=1}^{n-1} I_m Z_{nm}^{fg} \quad \text{where} \quad Z_{nm}^{fg} = H_0^{(2)}(k|\vec{\rho}_n - \vec{\rho}_m|) \quad (2.29)$$

must be computed. In the above expression, $I_m = \bar{I}^{f,(i)} + \bar{I}^{b,(i-1)}$. (It is noted that the constants relating H_0^2 to the 2D Green's function are absorbed into I_m).

To reduce the computational cost of this computation, the spectral acceleration presented in [6] divides the elements into two groups for a given receiving element: *strong interaction* and *weak interaction* groups, as shown in Figure 2.13(a). The criterion that defines these groups is the distance from the receiving element. For a given distance L_s which includes N_s elements ($L_s = N_s \cdot \Delta x$, where Δx is the sampling increment), the forward contribution is decomposed as:

$$E_f(\vec{\rho}_n) = E_w(\vec{\rho}_n) + E_s(\vec{\rho}_n) \\ E_w(\vec{\rho}_n) = \sum_{m=1}^{n-1-N_s} I_m Z_{nm}^{fg} \quad ; \quad E_s(\vec{\rho}_n) = \sum_{m=n-N_s}^{n-1} I_m Z_{nm}^{fg} \quad (2.30)$$

where E_w and E_s are the fields of the weak and strong interaction groups, respectively.

The radiation of the *strong interaction group* is computed as in (2.30), but the *weak group* contribution is obtained by employing the spectral representation of the Hankel function:

$$H_0^{(2)}(k|\vec{\rho}_n - \vec{\rho}_m|) = \frac{1}{\pi} \int_{C_\phi} e^{-jk[(x_n - x_m) \cos \phi + (z_n - z_m) \sin \phi]} d\phi = Z_{nm}^{fg} \quad (2.31)$$

where C_ϕ is the path of integration in the complex ϕ plane (shown later in Figure 2.14). Introducing (2.31) into the expression for $E_w(\vec{\rho}_n)$ and interchanging the integration and

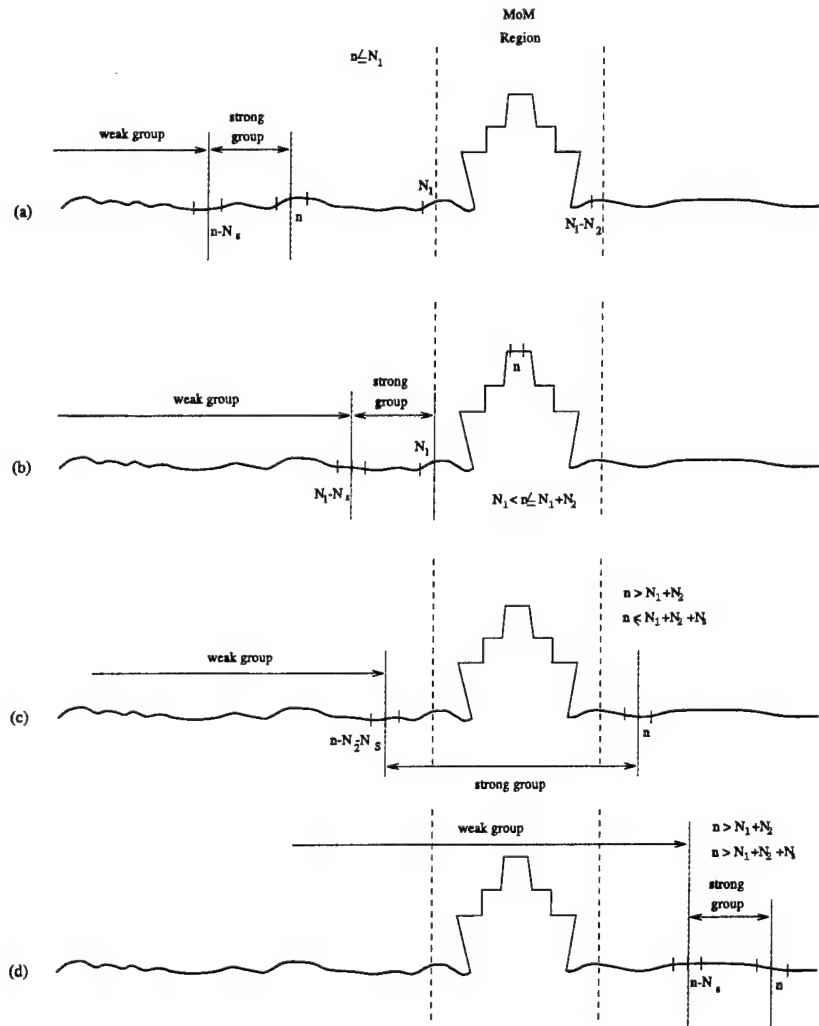


Figure 2.13: Different definitions of the strong and weak groups as a function of the position of the receiving point n .

summation, yields,

$$E_w(\vec{\rho}_n) = \frac{1}{\pi} \int_{C_\phi} F_n(\phi) e^{-jkz_n \sin \phi} d\phi, \quad (2.32)$$

where

$$F_n(\phi) = \sum_{m=1}^{n-N_s-1} I_m e^{-jk[(x_n - x_m) \cos \phi - z_m \sin \phi]}. \quad (2.33)$$

It is at this point where the reduction in the computational cost is obtained because it can be shown that $F_n(\phi)$ is easily updated using a recursive procedure:

$$F_n(\phi) = F_{n-1}(\phi) e^{-jk(x_n - x_{n-1}) \cos \phi} + I_{n-N_s-1} \cdot e^{-jk(x_n - x_{n-N_s-1}) \cos \phi} e^{-jkz_{n-N_s-1} \sin \phi} \quad (2.34)$$

Up to this point the spectral acceleration procedure is the same as presented in [6]. The modifications will appear in regions #2 and #3 as discussed next, and in the numerical evaluation of the integral in (2.32) which will be discussed at the end of this section.

Region #2

Referring to Figure 2.13.b, the sampled values for the current in this region ($I_n^{f,(i)}$, $N_1 < n \leq N_1 + N_2$) are obtained with the direct solving of the following matrix system:

$$\bar{Z}_{nm}^{sg} \cdot \bar{I}_n^{f,(i)} = \bar{V} - \bar{E}_f^{(i)} \quad n, m \in (N_1, N_1 + N_2] \quad (2.35)$$

The evaluation the right-side of (2.35) requires the computation of $E_f^{(i)}(\vec{\rho}_n)$ for each of the elements of this region using,

$$E_f^{(i)}(\vec{\rho}_n) = \sum_{m=1}^{N_1} I_m Z_{nm}^{fg}. \quad (2.36)$$

Due to the different way in which the current is evaluated in this region (compared with regions #1 and #3), the group division is done using another criterion. An element belongs to the *weak* group if the distance from this element to the first element in region #2 (element $(N_1 + 1)$) is larger than L_s . So, in terms of number of elements, it can be express as:

$$E_f^{(i)}(\vec{\rho}_n) = \sum_{m=1}^{N_1-N_s} I_m Z_{nm}^{fg} + \sum_{m=N_1-N_s+1}^{N_1} I_m Z_{nm}^{fg} = E_w^{(i)}(\vec{\rho}_n) + E_s^{(i)}(\vec{\rho}_n) \quad (2.37)$$

It must be noticed that with this criterion, the *weak* and the *strong* groups remain constant for all the elements of the region #2. Taking this point into account, the recursive procedure to update the function $F_n(\phi)$ must be changed to:

$$F_n(\phi) = F_{n-1}(\phi) e^{-jk(x_n - x_{n-1}) \cos \phi} \quad n \in (N_1, N_1 + N_2] \quad (2.38)$$

Region #3

In the region #3 ($n > N_1 + N_2$), the *forward* current component is obtained by forward substitution as in the region #1 and the following matrix-vector product must be computed:

$$E_f(\vec{\rho}_n) = \sum_{m=1}^{n-1} I_m Z_{nm}^{fg}. \quad (2.39)$$

Therefore the procedure used to evaluated the contribution of the *weak* group elements is going to be similar to that in Region #1. Some modifications are included for the first N_s elements of this region for updating the *weak* group due to the presence of the MoM/ship region (Region #2). This splits the Region #3 computation into two cases shown in Figures 2.13 (c) and (d).

(1) Figure 2.13(c): $n \leq N_1 + N_2 + N_s$

For the first N_s elements of this region a special division for the *strong* group is considered. The *strong* group will be formed by all the elements of Region #2, *plus* the N_s elements in Regions #1 and #3 which precede the receiving element. Therefore, the *strong* group will contain $N_2 + N_s$ elements. With this distribution, (2.39) can be rewritten as:

$$E_f(\vec{\rho}_n) = \sum_{m=1}^{n-1-N_2-N_s} I_m Z_{nm}^{fg} + \sum_{m=n-N_2-N_s}^{n-1} I_m Z_{nm}^{fg} = E_w(\vec{\rho}_n) + E_s(\vec{\rho}_n) \quad (2.40)$$

and the procedure to obtain $F_n(\phi)$ must change to:

$$F_n(\phi) = F_{n-1}(\phi) e^{-jk(x_n - x_{n-1}) \cos \phi} + I_{n'} \cdot e^{-jk(x_n - x_{n'}) \cos \phi} e^{-jkz_{n'} \sin \phi} \quad (2.41)$$

where $n' = n - 1 - N_s - N_2$.

(2) **Figure 2.13(d):** $n > N_1 + N_2 + N_s$

When a receiving point if this set is considered, all the elements of the *strong* group are placed in region #3, and the elements of region #2 will be a part of the *weak* group. Therefore, (2.39) can be divided as in (2.30) as

$$E_f(\vec{\rho}_n) = \sum_{m=1}^{n-1-N_s} I_m Z_{nm}^{fg} + \sum_{m=n-N_s}^{n-1} I_m Z_{nm}^{fg} = E_w(\vec{\rho}_n) + E_s(\vec{\rho}_n), \quad (2.42)$$

To compute $E_w(\vec{\rho}_n)$, the function $F_n(\phi)$ can be evaluated as in (2.34), after updating its value at the first element of this set ($p = N_1 + N_2 + N_s + 1$) with the contributions due to the elements in region #2:

$$F_p(\phi) = F_{p-1}(\phi) e^{-jk(x_p - x_{p-1}) \cos \phi} + \sum_{n'=N_1+1}^{N_1+N_2} I_{n'} \cdot e^{-jk(x_p - x_{n'}) \cos \phi} e^{-jkz_{n'} \sin \phi} \quad (2.43)$$

For the following points ($n > p$), the values of $F_n(\phi)$ are obtained via (2.34).

2.4.2 Contour Integral

The previous points of this section were focused on how to evaluate the integrand of (2.32) for the different regions. In this part, the numerical computation of this integral is explained, including how the integration path, the limits and the numerical sampling density are determined. The procedure to obtain these three parameters is basically the same used in [6], although some modifications are included due to the presence of a target on the sea surface. These modifications affect mainly the integration path and the limits of integration.

As explained in [6], because of the Hankel function is analytic in the complex space, the integration contour C_ϕ can be deformed to another integration path C_δ as shown in Figure 2.14. This path is chosen in order to reduce the computational cost needed to evaluate the integral, and to reduce errors caused by the limited numerical precision of the computer when the integrand presents large values. C_δ follows a straight line in the range $-\phi_{s,max} \leq \text{Re}\{\phi\} \leq \phi_{s,max}$ where $\phi_{s,max}$ is defined by

$$\phi_{s,max} = \tan^{-1} \left(\frac{z_{max} - z_{min}}{L_s} \right), \quad (2.44)$$

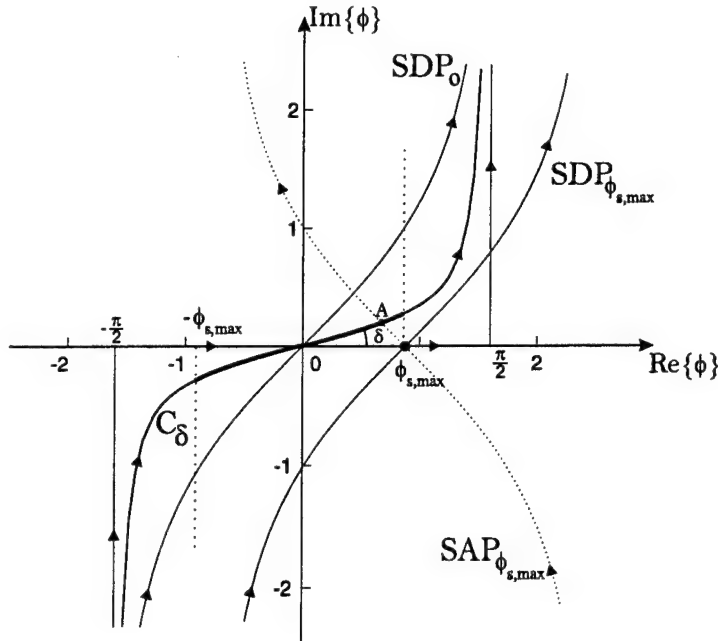


Figure 2.14: Integration paths of $H_0^{(2)}$ in the complex ϕ -plane.

and is illustrated in Figure 2.15. (Notice that $\phi_{s,max}$ is the maximum angle from horizontal formed by any point of the weak group and the receiving element). δ is the angle that C_δ makes with the real axis of the complex ϕ plane, and is chosen such that the integrand of (2.32) does not become too large anywhere along C_δ .

The steepest descent path (SDP) through the saddle point $\phi_{s,max}$ is also in the Figure 2.14, along with the steepest ascent path which is orthogonal to the SDP at the saddle point. It is noted that the SDP and SAP make an angle of 45° with the real axis. For different sets of source and receiver elements, the saddle point moves to different points along the $Re\{\phi\}$ axis in the range $-\phi_{s,max} \leq Re\{\phi\} \leq \phi_{s,max}$. The integrand will have its maximum value on C_δ at the point where the SAP through $\phi_{s,max}$ crosses C_δ (point A in Figure 2.14).

The angle δ is given by \widehat{AOB} , where $B = \phi_{s,max}$ and A is the point on the SAP of $\phi_{s,max}$ where the integrand is equal to e^2 . This criterion guarantees that the every contribution of the elements in the *weak* group are smaller than e^2 , which is chosen to keep the integral numerically stable. It is noted the in [6] this limiting value was chosen to be e^{20} . The reason a much lower is used here is because many of the saddle points associated with the Region

#2 target structure are grouped close to $\phi_{s,max}$ (see Figure 2.15), so their total contribution to the integrand via (2.33) will be much larger than e^2 . In [6] the saddle points are grouped more around the origin, with only a few point near $\pm\phi_{s,max}$. With this new limit of e^2 , it may be shown that δ is given approximately by,

$$\delta = \tan^{-1}(1/b) \quad \text{with} \quad b = \sqrt{\frac{kR_s}{2}}\phi_{s,max} - 1 \quad (2.45)$$

where $R_s = \sqrt{L_s^2 + (z_{max} + z_{min})^2}$. Using this new limit, the integrand in (2.32) does not

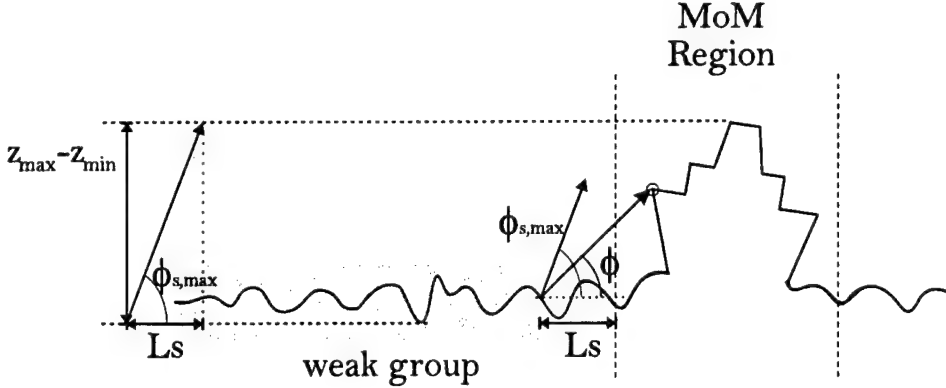


Figure 2.15: Saddle points for the weak group are placed at angles close to $\phi_{s,max}$.

present very large values as demonstrated in Figure 2.16 for a receiving position at the top of the target. This allows the integral to be evaluated very accurately as is shown in the numerical results.

Once the integration path has been determined, the next step is to set up the integration limits. These limits can be easily obtained by using geometrical considerations. If $\phi_{s,max}$ is defined as in Figure 2.15, where z_{max} and z_{min} will denote the maximum and minimum z coordinates of the whole surface including the target, then the integration limits will be $[-\phi_{s,max}, \phi_{s,max}]$. Figure 2.16 plots the integrand of (2.32) for a point at the top of the target, it can be noticed that the main contributions are inside the integration interval, and the integrand is nearly zero outside.

The value of the integration step size used for the FB method in [6] is also used here,

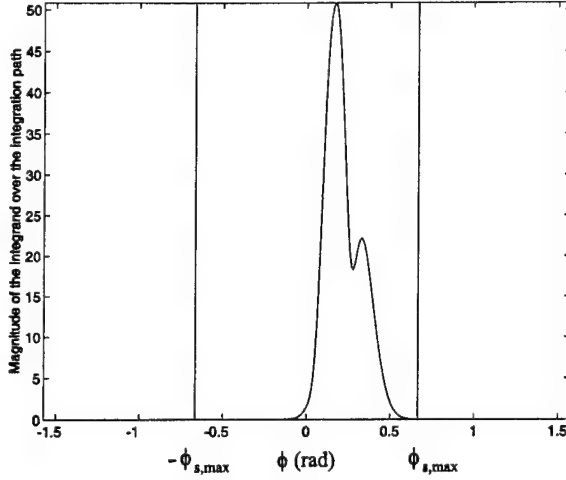


Figure 2.16: Integrand of (10) for a point at the top of the target.

given by

$$\Delta\phi = \sqrt{\frac{5}{k R_s}}/22 \quad (2.46)$$

and the variable of the integration is mapped to the $\text{Re}\phi$ axis according to

$$d\phi \rightarrow \Delta\phi e^{j\delta} \quad (2.47)$$

Using the above integration limits and step size, the integral of (2.32) it is computed by adding the contribution of $2Q + 1$ plane waves in which the integral is discretized. The value of Q is obtained from:

$$Q = \left\lceil \frac{\beta_s}{\Delta\phi} \right\rceil \quad (2.48)$$

where $\lceil \cdot \rceil$ denotes the nearest integer larger than the argument.

2.4.3 Computational cost

The computational cost associated to the Generalized Forward-Backward Method is $O(N^2)$ per iteration. This includes the $O(N^2)$ forward (or backward) integration of the currents radiated to every element, plus the $O(N_2^2)$ computational cost of a matrix-vector product to obtain the current over the MoM Region #2. (The Region #2 MoM matrix is assumed to be factorized prior to the iteration process.) Considering that $N_2 \ll N$, the computational cost per iteration of the Generalized Forward-Backward method is $O(N^2)$

When the Spectral Acceleration method described in this section is applied to the GFB, the computational cost per forward or backward iteration is estimated as follows. The cost for the strong group iteration for N receiving points is $N_s \cdot N$. (One unit of cost is defined roughly as one complex exponentiation plus one complex multiplication plus one complex addition.) The cost of computing the spectral amplitudes (2.34) of $2Q + 1$ plane waves is $2(2Q + 1) \cdot (N - N_s)$, and the cost of computing the integral (2.32) is $(2Q + 1) \cdot (N - N_s)$ for $N - N_s$ receiving elements. The cost of the Region #2 matrix vector product is again N_2^2 . The total cost per iteration is then given approximately by

$$Cost \approx N \cdot N_s + 3(2Q + 1) \cdot (N - N_s) + N_2^2. \quad (2.49)$$

Since N_2 , N_s , and Q are fixed for a given target size, frequency, and surface roughness, the total cost scales as $O(N)$ as the length of the surface increases (provided $N_2^2 \ll N \cdot N_s$).

As a result of the introduction of the spectral acceleration, the computational cost of the GFB is reduced from $O(N^2)$ to $O(N)$ when increasing surface lengths for a given frequency are considered. For the case of a given target and a given sea-surface, the computational cost as a function of frequency is $O(N^2)$ because N_s scales with N for this case. However, even in this situation the spectral acceleration greatly reduces the computational cost of the method. Compared with the ordinary GFB, for a given problem size the accelerated version (fast GFB) reduces the computational cost by a factor of about L_s/L where L is the total length of the surface

2.4.4 Results

Results are included in this section to demonstrate the accuracy and efficiency of the spectral acceleration introduced into the GFB method for different incident fields, frequencies and target heights. For all the results, a Pierson-Moskowitz ocean spectrum wave model is used to generate random sea surfaces.

Figure 2.17 shows the magnitude of the computed currents as a function of the index number for a 13 m high target on a 409.6 m sea surface with a wind speed of 15 m/s (RMS wave height = 1.215 m). The incident field is produced by a linear array of 15 equally spaced

electric line sources with a cosine aperture weighting function to reduce the sidelobe levels. The source, placed at 344 m from the center of the ship, points directly to the ship and forms a 5° angle with the horizontal axis. The geometry and source location are drawn to scale in Figure 2.17(a). Figure 2.17(b) shows the currents at 300 MHz computed using the fast GFB method, and Figure 2.17(c) shows the difference between these currents and the currents computed by the original GFB method. Figures 2.17(d) and (e) show the same results as (b) and (c), respectively, at 1.2 GHz. Figure 2.18 shows the same results at 300 MHz for a target that is a 26 m high.

It is clear that the relative error introduced by the spectral acceleration for these cases is on the order of 10^{-3} or less. This shows that the combination of the GFB method with spectral acceleration provides an accurate method to analyze the scattering from targets on very large sea surfaces.

In the previous examples, the incident field was generated by an array whose radiation pattern was designed to minimize the diffraction effects at the endpoints of the finitely truncated sea surface. In the following examples, an exponentially tapered resistive sheet (R-card) will be placed at both ends of the sea surface to minimize the end point effects as done in [10]. This allows a pure plane wave incident field to be used instead of a localized directive source.

With the R-cards present, the surface impedance near the ends varies as

$$\Delta Z_{mm} = R_1 \cdot (e^{\alpha x} - 1) \quad \text{where} \quad \alpha = \frac{\ln(R_1/R_2)}{L_R}, \quad (2.50)$$

x is the distance from the junction between the R-card and the sea surface, and L_R is the length of the R-card. The surface impedance is zero where the R-card joints the PEC sea surface, and increases exponentially to $R_2 - R_1$ at the ends. The values of R_1 and R_2 used in the results which follow are

$$\begin{aligned} R_1 &= 58.5 \times 10^{-0.49} \quad \Omega/\square \\ R_2 &= 58.5 \times 10^{0.55} \quad \Omega/\square \end{aligned} \quad (2.51)$$

The surface impedance is easily incorporated into the impedance matrix simply by adding

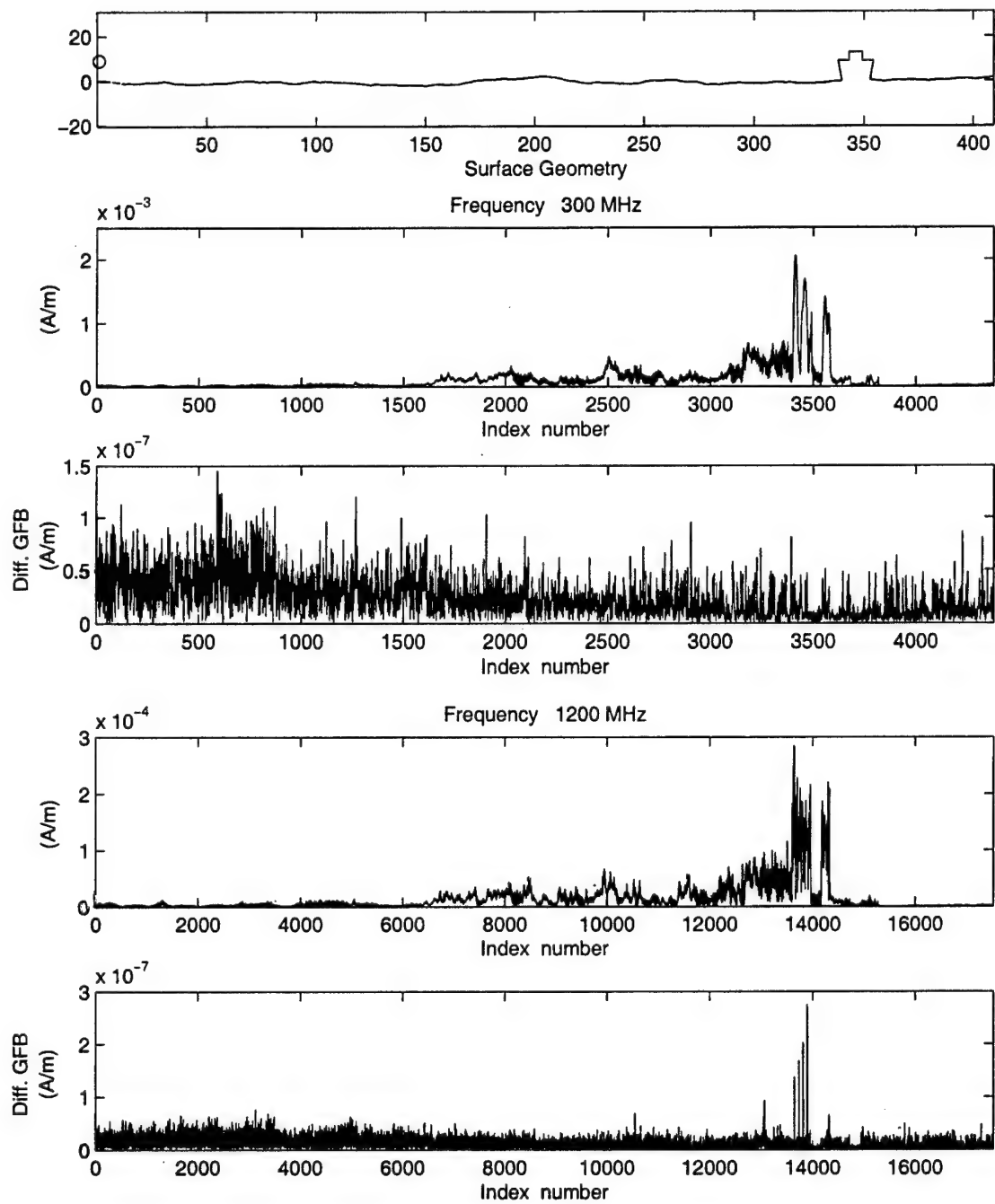


Figure 2.17: (a) Example geometry and source position (units in meters) for a 13 m high target, (b) Magnitude of the current in A/m obtained by applying the Spectral Acceleration (10th iteration) at 300 MHz, and (c) Magnitude of the difference between the previous result and a reference solution (GFB) (10th iteration). (d) Same result as (b) at 1.2 GHz. (e) Same result as (c) at 1.2 GHz. The length for the strong group is $L_s = 12m$.

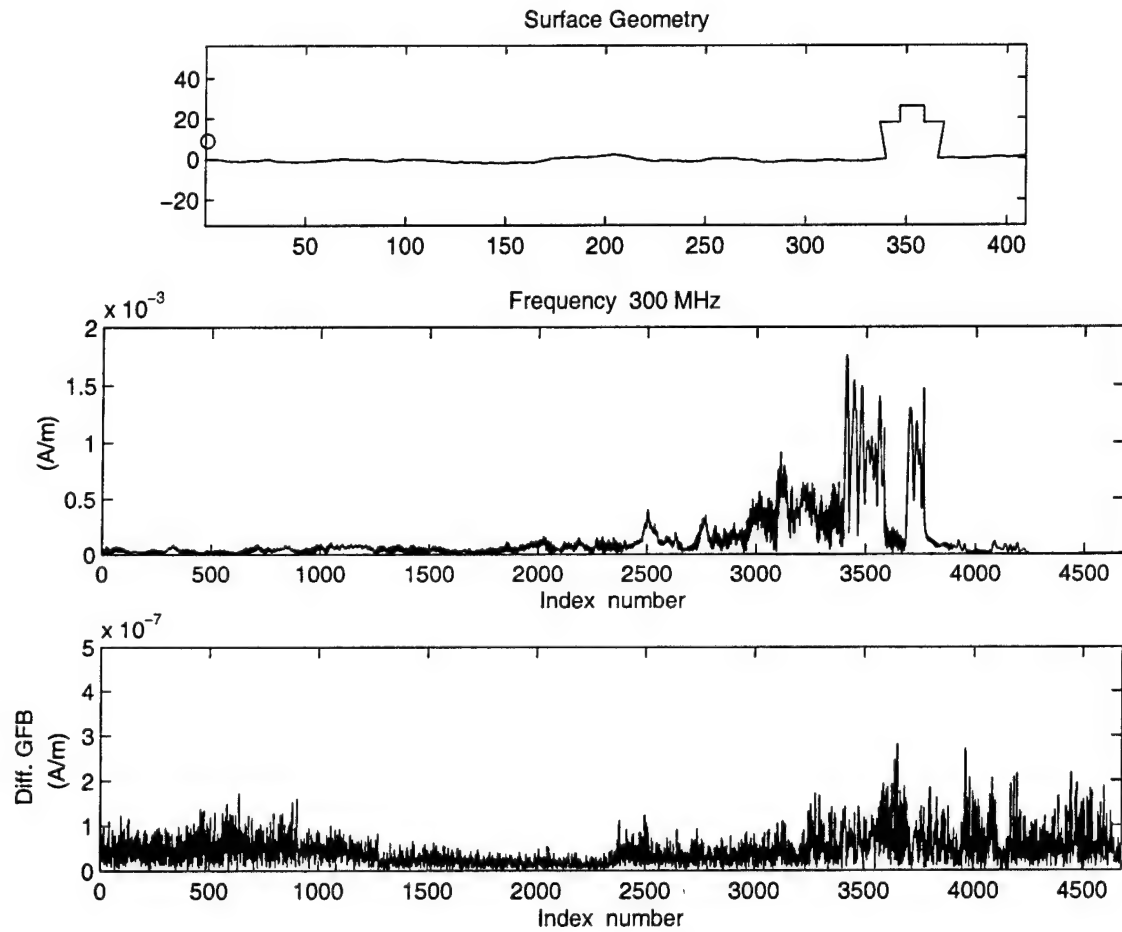


Figure 2.18: (a) Example geometry and source position (units in meters) for a 26 m high target, (b) Magnitude of the current in A/m obtained by applying the Spectral Acceleration (10th iteration) at 300 MHz, and (c) Magnitude of the difference between the previous result and a reference solution (GFB) (10th iteration). The length for the strong group is $L_s = 24$ m.

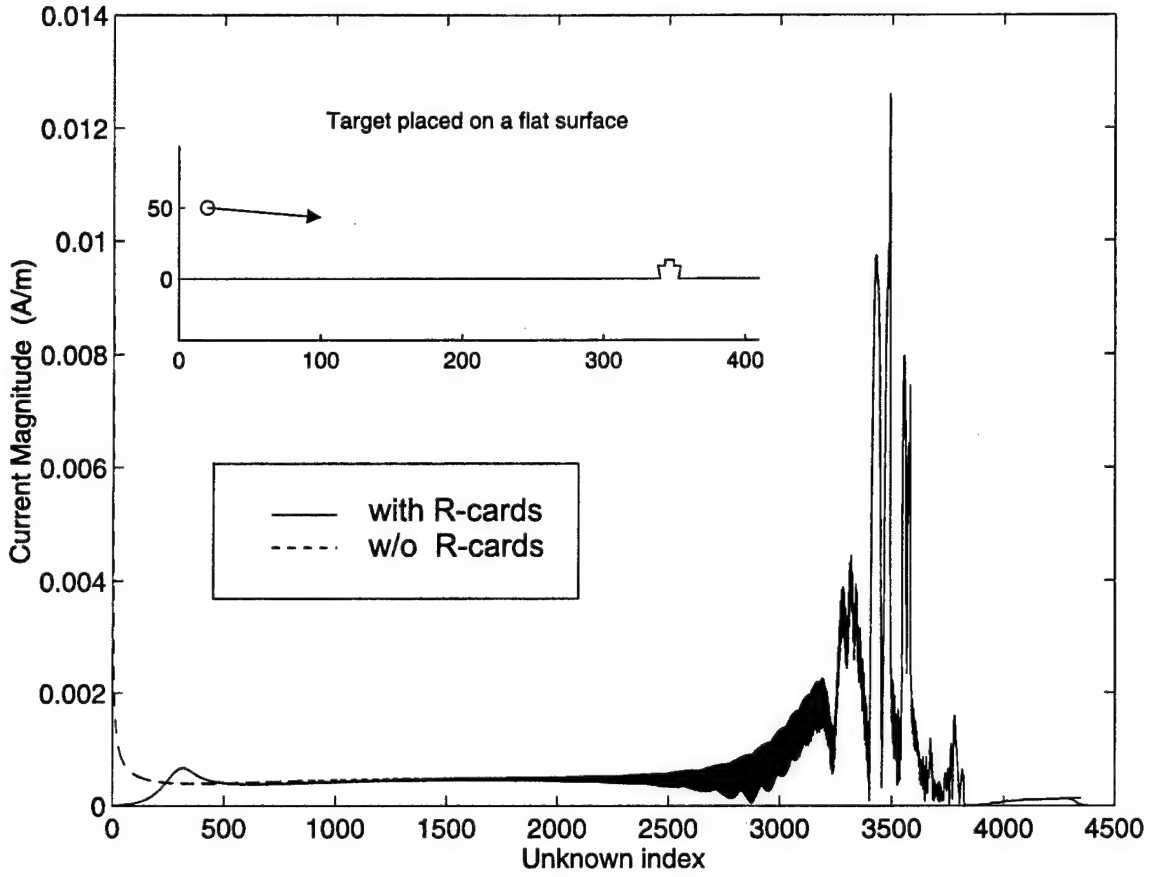


Figure 2.19: Distribution of the currents with and without the r-cards.

Z_s to the self terms Z_{mm} in the R-card regions.

Figure 2.19 shows the currents computed with and without the r-cards for a plane wave illuminating the target of Figure 2.17(a) on a 409.6 m flat surface. The elevation angle of the plane wave is 5° and its frequency is 300 MHz. The R-card placed the left end of the sea surface is 50λ long and the one placed at the right end is 10λ . It is seen that the R-cards minimize the end-point effect by smoothly tapering the current to zero. The effect of the R-cards on the scattered fields can be seen in Figure 2.20 where the bistatic 2D radar cross section (RCS) due to both currents is plotted. The use of the R-cards removes the rapid variations caused by the endpoint diffractions.

One of the reasons to include the spectral acceleration in the GFB method is to be able to analyze very large sea surfaces when the incidence angle is very low, because grazing

Bistatic RCS

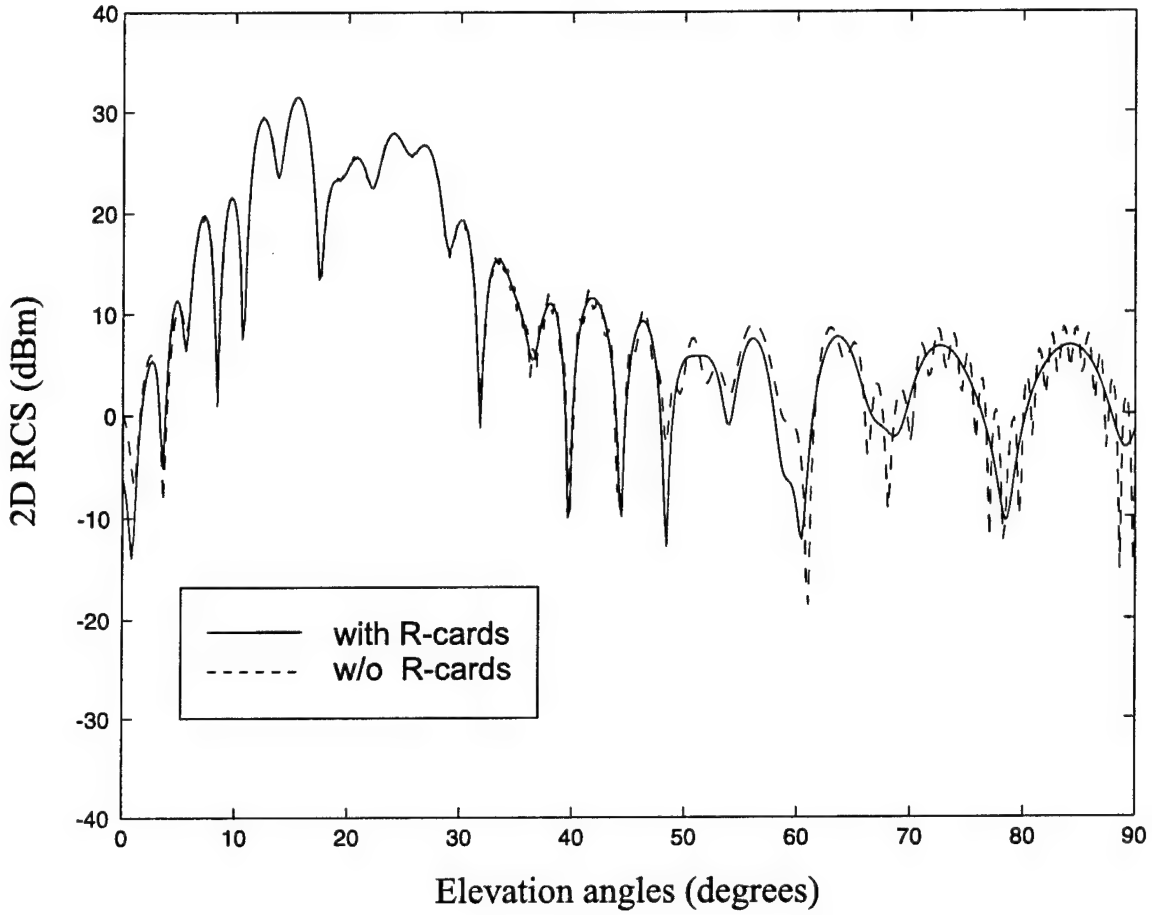


Figure 2.20: Bistatic RCS due to the currents with and without the r-cards. Frequency = 300 MHz, elevation angle = 5° .

incidence angles tend to illuminate a very large portion of the sea surface. The next examples show how the truncated length of the sea surface affects the RCS computations.

Figure 2.21 shows the bistatic RCS for the same flat surface case as Figure 2.20 for two finite surface lengths: 409.6 m, 3276.8 m. The lengths of the surfaces in front of the target are 340m and 3200 m, respectively. Again, the plane wave elevation angle is 5° and the frequency is 300 MHz. The infinite surface result is found using image theory. Both finite surface results match nearly exactly the image theory reference solution, but it is clear that the larger surface is more accurate at very low angles. The numerical precision of the fast method and the tapered R-card endpoint treatment is quite impressive considering that the

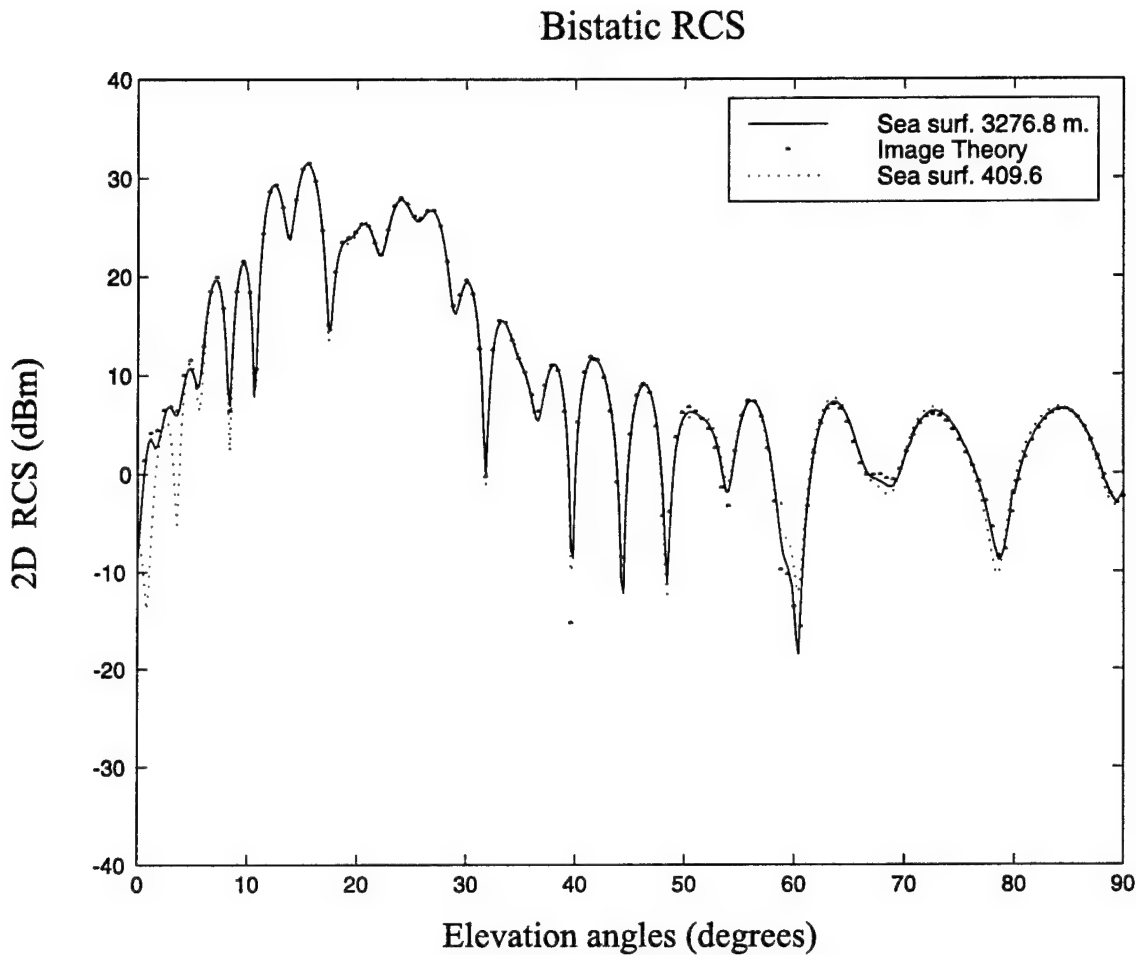


Figure 2.21: Bistatic RCS for two different lengths of a flat surface. Frequency = 300 MHz, elevation angle = 5° .

currents over target plus the entire sea surface are integrated to give the scattered field.

In the Figure 2.22, the same problem is analyzed but in this case two different lengths of rough sea surface are considered instead of flat surfaces. The wind speed used for this realization is 5 m/s (RMS wave height = 0.135 m). The rough sea surface is the same for both cases over the 340 m closest to the target. The two results match except for very low angles. The results of this figure and the last show why a large surface must be considered when low-grazing angles are analyzed.

Figure 2.23 shows the CPU time per iteration required by both methods (GFB and GFB with Spectral Acceleration) as a function of the number of unknowns for the sea surface.

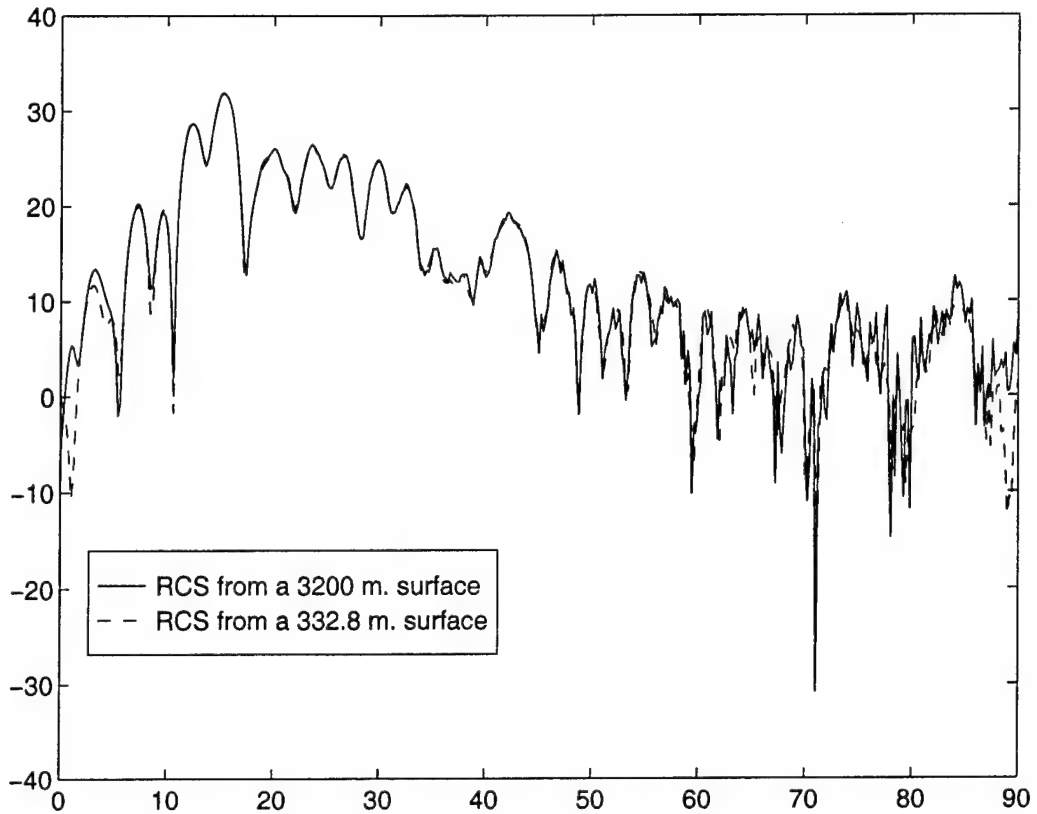


Figure 2.22: Bistatic RCS for two different lengths of rough sea surface. Frequency = 300 MHz, elevation angle = 5° , wind speed = 5 m/s.

These results agree with the computational cost estimate shown in the previous section; the GFB method presents a computational cost per iteration of $O(N^2)$, while with the spectral acceleration this cost is reduced to $O(N)$.

2.4.5 Conclusions

By including this Spectral Acceleration in the Generalized Forward-Backward method, it is possible to analyze the scattering from targets on very large surfaces with a low computational cost and without lost of accuracy. This makes this method suitable for analyzing low-grazing angle scattering problems where a large surface must be considered to solve the problem.

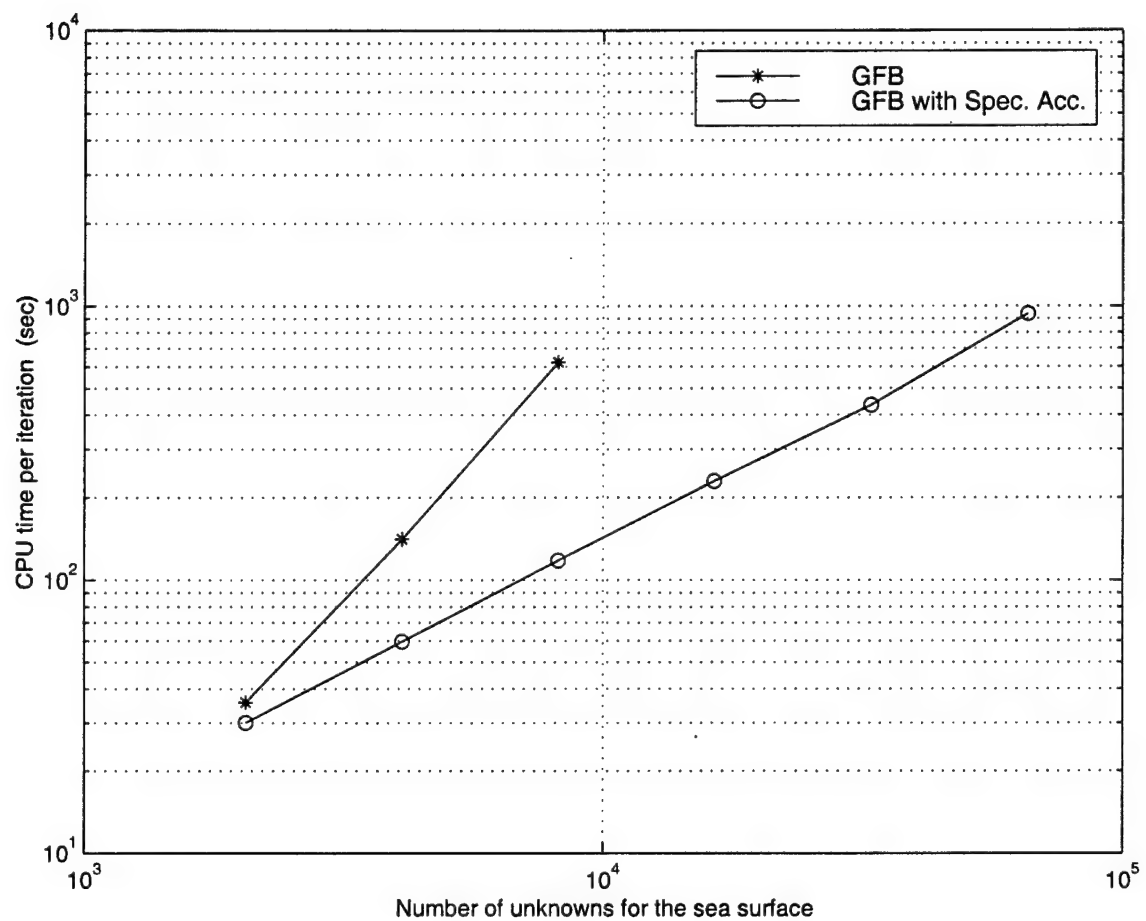


Figure 2.23: CPU time per iteration required by both methods (GFB and GFB with Spectral Acceleration) on a SGI workstation with a 150 MHz IP22 Processor.

Chapter 3

Plane Wave Spectral Properties of the Sea Scattered Field

3.1 Introduction

In this chapter the plane wave spectrum of the sea scattered field due to an incident plane wave is investigated. An understanding of the plane wave spectrum is important for gaining insight into a ray-optical representation of the sea scattered field. This would allow a target to be placed on the sea surface and its RCS computed using the ray-optical representation as the incident field. RCS prediction codes which use high-frequency asymptotic methods generally must assume a ray-optical incident field. In the following the polarization is horizontal and normal to the 2D geometry, and the surface is assumed to be PEC.

The plane wave spectrum is defined from the Fourier transform of the fields over a vertical cross-section above the sea surface, as shown in Figure 3.1. The total forward propagating electric field in the vicinity of the target is given approximately in terms of its plane wave spectrum as

$$E_y(x, z) \approx \int_{-\infty}^{\infty} F_y(k_z) e^{-j(k_x x + k_z z)} dk_z \quad (3.1)$$

where the Fourier spectrum is given by

$$F_y(k_z) = \frac{1}{2\pi} \int_0^h E_y(0, z) e^{jk_z z} dz \quad (3.2)$$

and h is the maximum height over which the expansion is valid. (3.1) is exact over the vertical cross-section at $x = 0$ and becomes more approximate as x is varied in the target

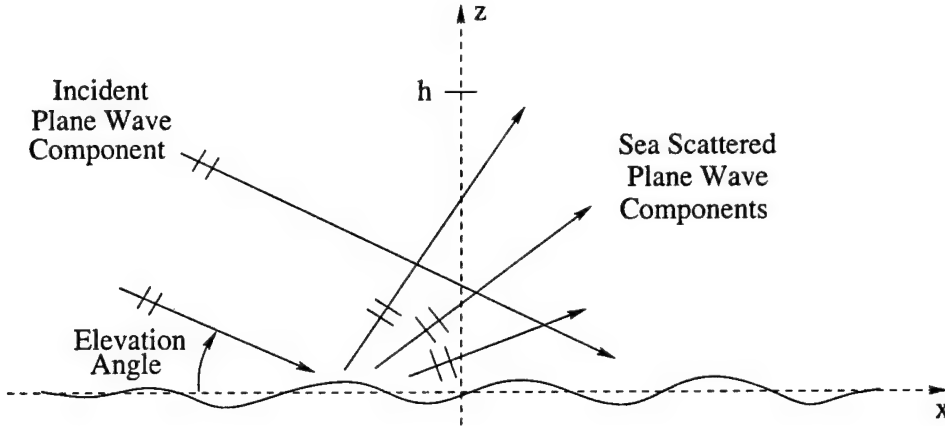


Figure 3.1: Incident and sea scattered fields transformed into a spectrum of plane waves over a vertical cross-section above the sea surface.

vicinity. We are usually only interested in propagating plane waves which are defined in terms of a propagation angle ϕ defined as the angle the plane wave makes with the x -axis. Using the transformation $k_z = k \sin \phi$ and integrating only over the propagating spectrum, (3.1) becomes

$$E_y(x, z) \approx k \int_{-\pi/2}^{\pi/2} F_y(\phi) \cos \phi e^{-j(kx \cos \phi + kz \sin \phi)} d\phi \quad (3.3)$$

where

$$F_y(\phi) = \frac{1}{2\pi} \int_0^h E_y(0, z) e^{j k z \sin \phi} dz. \quad (3.4)$$

This approximation is expected to be very accurate for large h and low angles of incidence. In the results which follow the sea scattered fields are computed numerically using the forward-backward method described in Chapter 2. The fields are then transformed using the above expressions.

3.2 Numerical Results

Figure 3.2 shows the magnitude of the plane wave spectrum for a 5° incidence angle and a wind speed of 5 m/s (11 mph) at 1 GHz. At this wind speed the standard deviation of the surface height profile σ (RMS wave height) is 0.135 m, corresponding to Sea State 2

as defined by the World Meteorological Organization (WMO) [2]. In terms of wavelength, $\sigma/\lambda = 0.45$. In general, the RMS wave height in meters is empirically related to the wind speed u in meters/second by [2]

$$\sigma = 0.0054u^2. \quad (3.5)$$

The actual surface is shown at the top of the figure. The “One realization” plot shows the total plane wave spectrum for this surface computed from (3.4), including the incident plane wave which corresponds to the impulse at a scattering angle of $\phi = -5^\circ$. The height h over which the fields are transformed for these results is 100 m. The sea scattered spectrum is visible for positive scattering angles, and shows an impulse at $\phi = 5^\circ$ which corresponds to the *coherent* reflection. The coherent component only contributes to the sea scattered field in the specular (direct reflection) direction, whereas the incoherent component contributes in all directions [1]. The coherent reflection is expected to always be about the same for a given incidence direction and wind speed, independent of time. The use of the term “coherent” in this report refers to a quantity that, by definition, does not change with time. This is shown in the “Coherent part” of Figure 3.2, which is the total spectrum averaged over 40 different randomly generated sea surfaces at a wind speed of 5 m/s. The incoherent spectrum averages out to zero while the coherent component stays relatively constant.

The coherent plane wave component of the scattered field may be obtained approximately by the physical optics (PO) technique used in [1] as

$$\begin{aligned} E_y^c &\approx E_y^i \Gamma(\phi^i) \\ \Gamma(\phi^i) &= R(\phi^i) e^{-2(k\sigma \sin \phi^i)^2} \end{aligned} \quad (3.6)$$

where $R(\phi^i)$ is the plane wave reflection coefficient for a planar interface of the same material as the sea surface and ϕ^i is the elevation angle of the incidence plane wave. For the case of Figure 3.2, $|\Gamma|=0.89$ computed from (3.6); this appears to agree with the numerical results because the coherent sea scattered impulse at 5° is about 0.89 of the incident impulse at -5° .

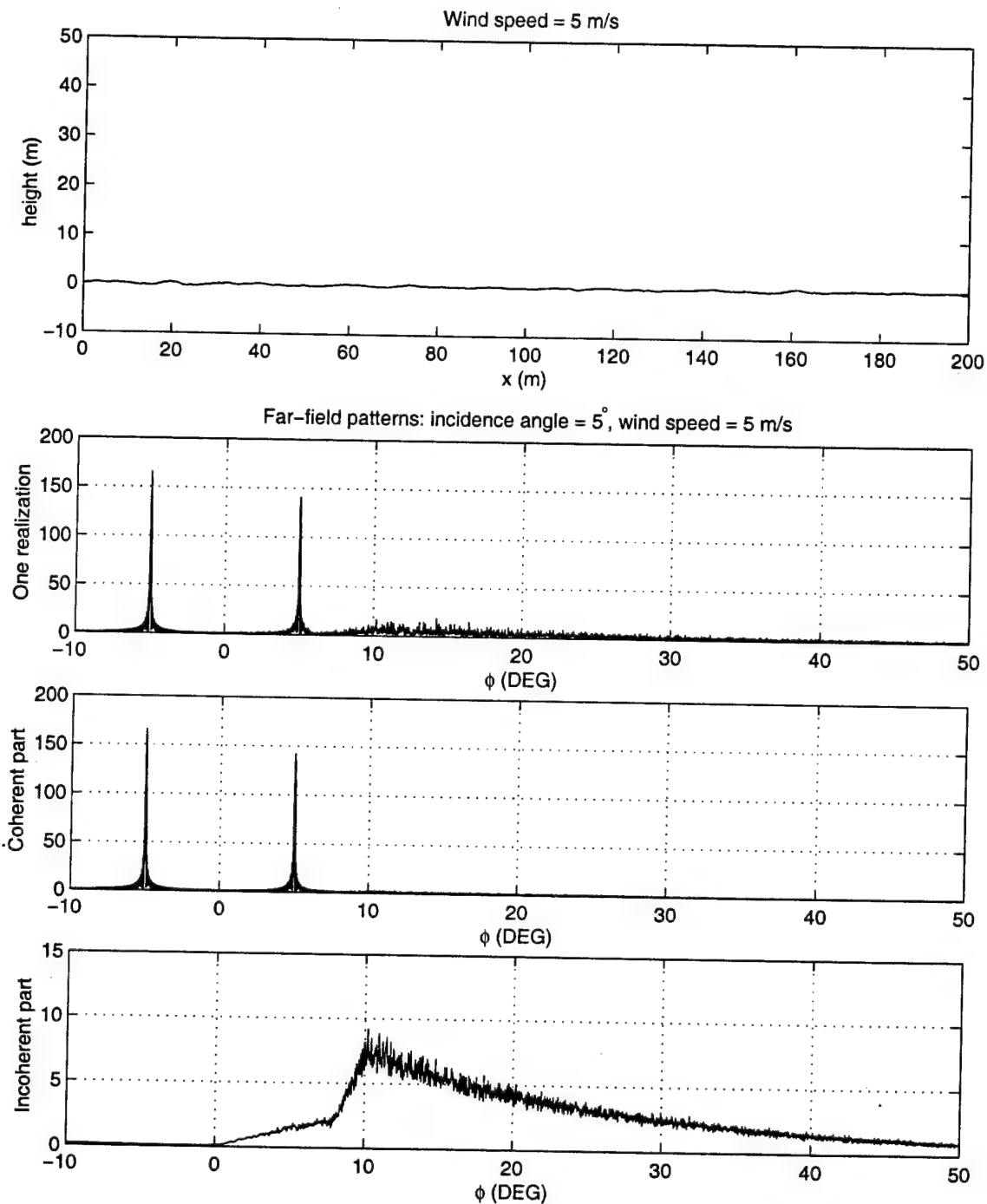


Figure 3.2: Plane wave spectrum due to a 1 GHz plane wave incident at 5° above a sea surface with wind speed 5 m/s. Coherent and incoherent parts are obtained by sampling 40 surface realizations.

As the coherent plot of Figure 3.2 shows, the remainder of the total spectrum, the *incoherent* spectrum, averages out to zero over many surface realizations indicating that it has a uniformly distributed random phase. The “Incoherent part” of the figure plots the RMS power of the incoherent spectrum averaged over 40 different randomly generated surfaces (and plotted on a smaller scale). For this result the coherent spectrum has been subtracted out. The incoherent power spectrum appears to have a well-behaved probability distribution as a function of angle. An analytic expression for this distribution is being investigated based on the derivation in [1].

Figure 3.3 shows the spectra for the same plane wave incident on a sea surface with a wind speed of 10 m/s (23 mph) and a corresponding RMS wave height $\sigma=0.54$ m (WMO Sea State 4), and $\sigma/\lambda = 1.8$. Clearly, the coherent component of the scattered field is much weaker than before (the incident plane wave component stays the same). For this case $|\Gamma|=0.14$ from (3.6), which is in fair agreement with the numerical results. Figure 3.4 shows the spectra for a sea surface with a wind speed of 15 m/s (34 mph), $\sigma=1.22$ m (WMO Sea State 5), $\sigma/\lambda = 4.1$, and $|\Gamma|=4.9 \times 10^{-5}$ from (3.6). For this case the coherent sea scattered component is not discernible.

As Equation (3.6) indicates, the coherent component is larger for lower angles of incidence. Figure 3.5 shows the spectra for a 1 GHz plane wave incident at 1.5° elevation over a sea surface at 15 m/s wind speed, which corresponds to $|\Gamma|=0.41$. The coherent scattered component is again visible in the sea scattered spectrum. This indicates that the coherent component may dominate for low-grazing angle RCS problems. This will be investigated further in the next two chapters.

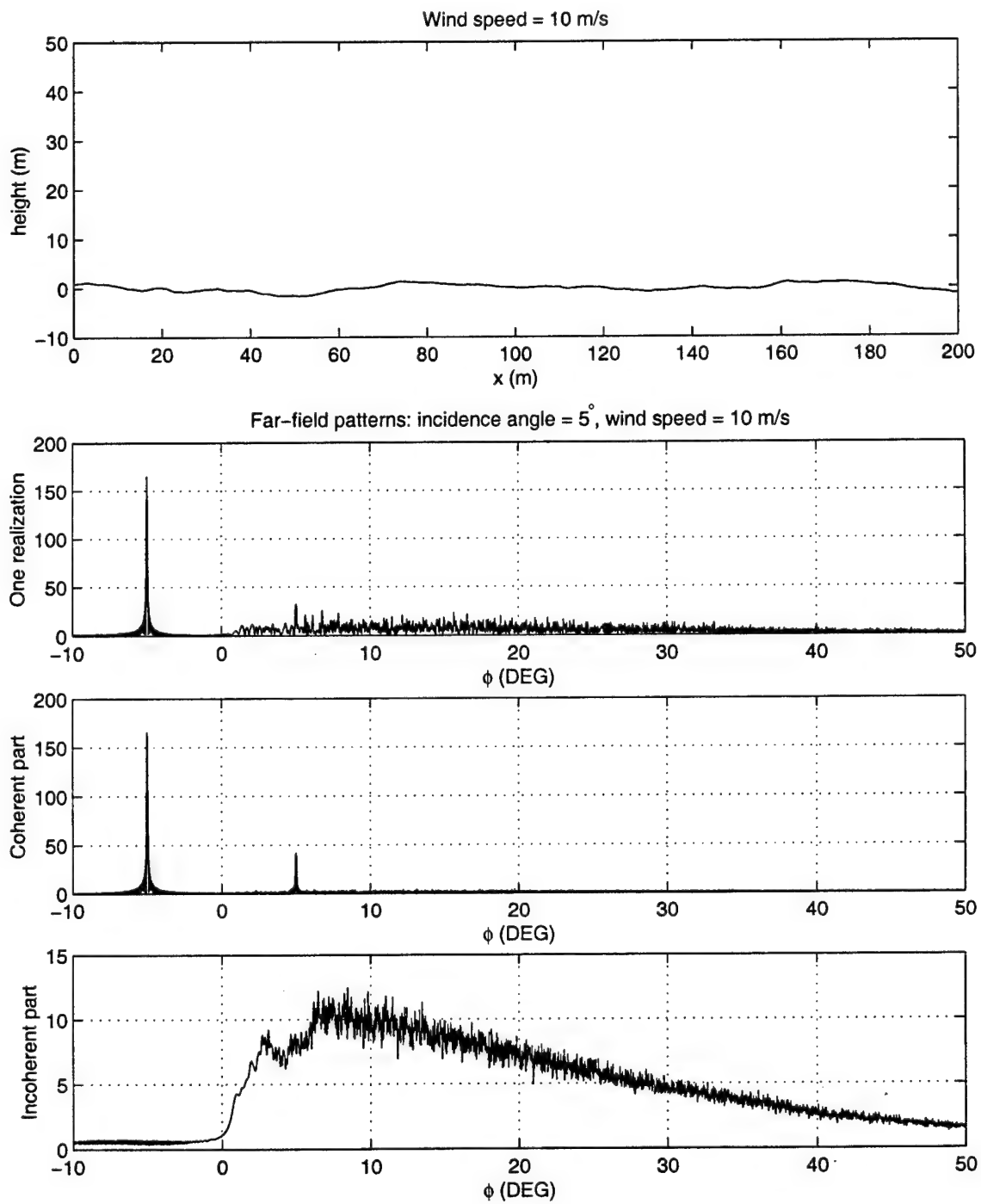


Figure 3.3: Plane wave spectrum due to a 1 GHz plane wave incident at 5° above a sea surface with wind speed 10 m/s. Coherent and incoherent parts are obtained by sampling 40 surface realizations.

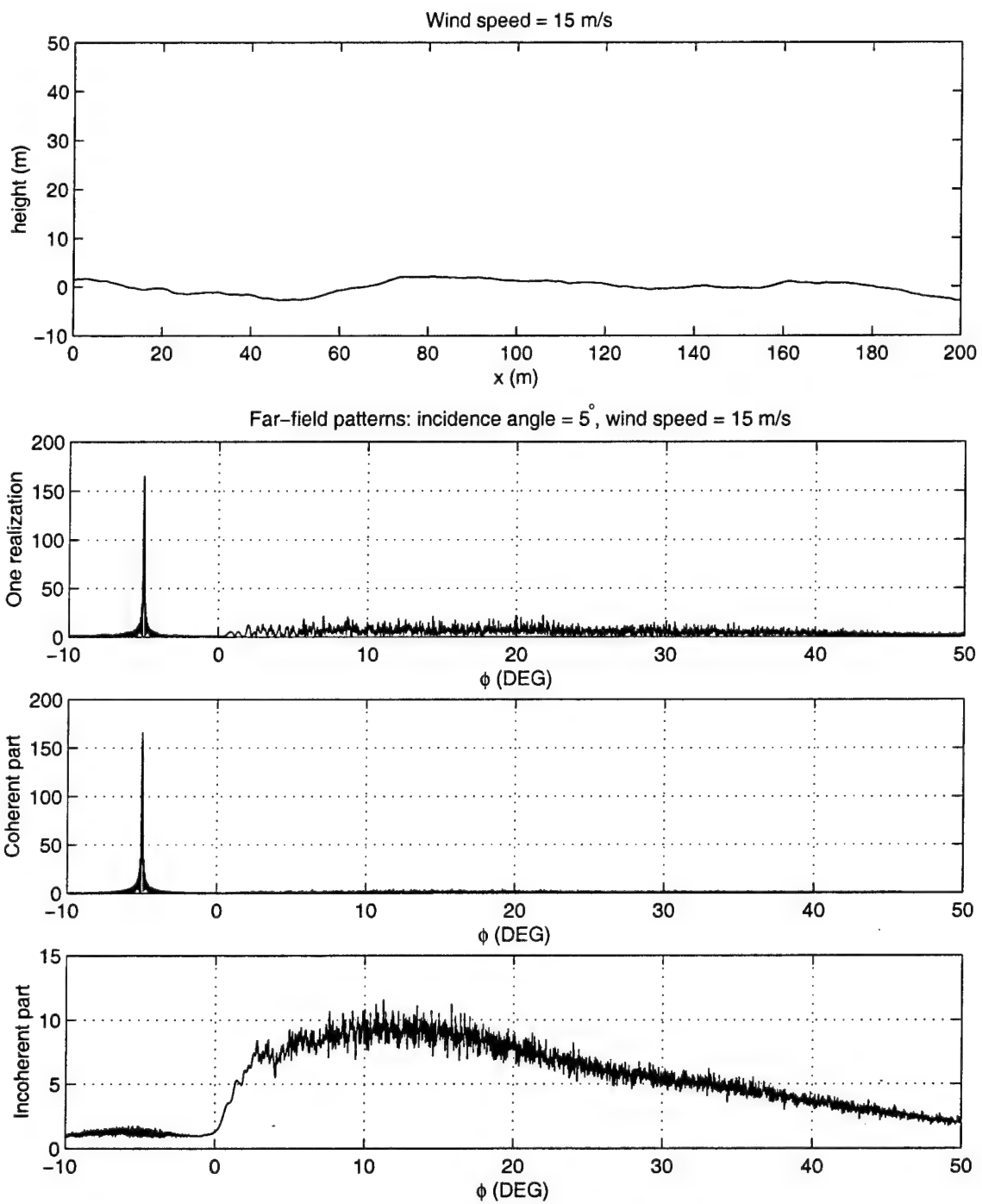


Figure 3.4: Plane wave spectrum due to a 1 GHz plane wave incident at 5° above a sea surface with wind speed 15 m/s. Coherent and incoherent parts are obtained by sampling 40 surface realizations.

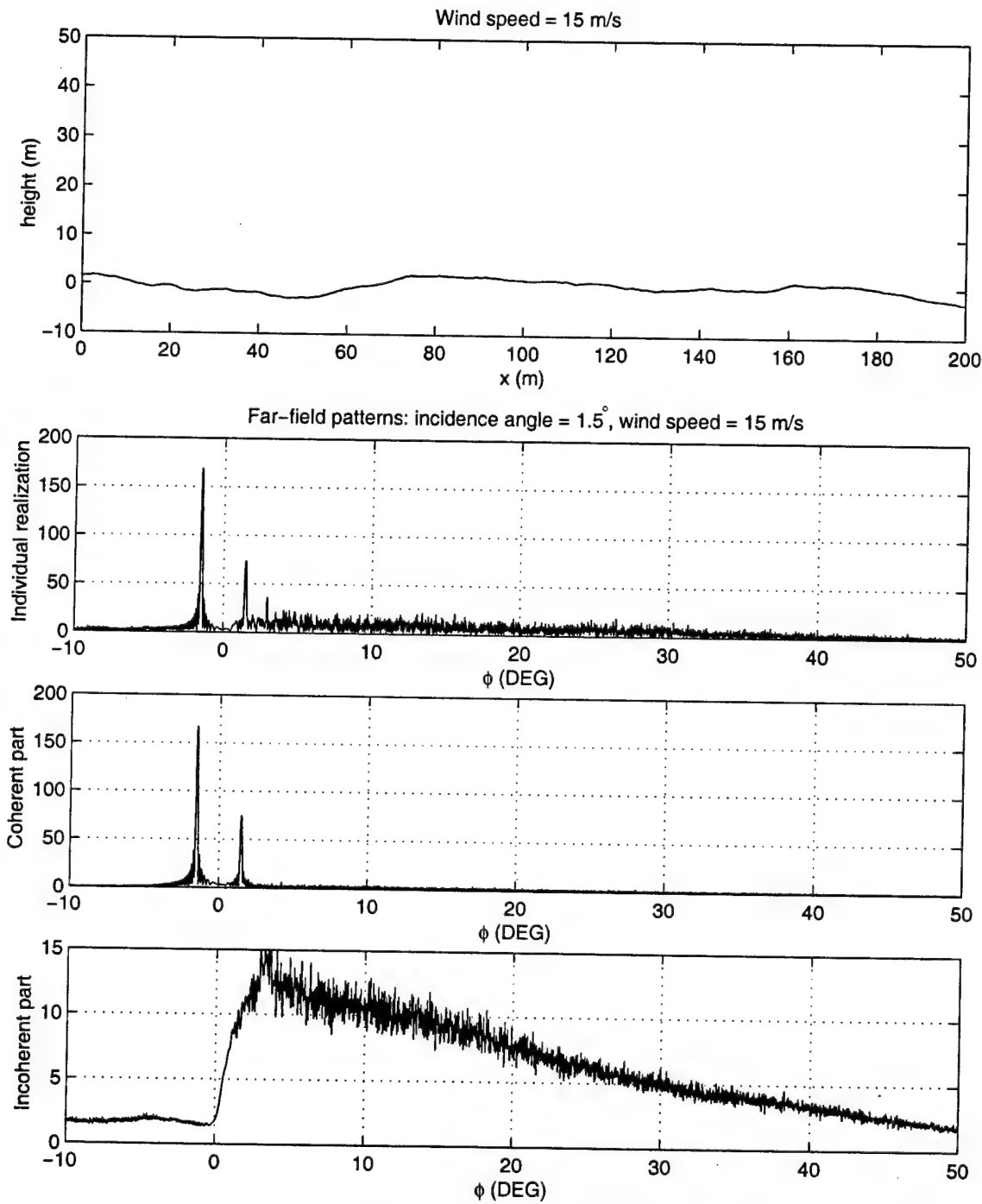


Figure 3.5: Plane wave spectrum due to a 1 GHz plane wave incident at 1.5° above a sea surface with wind speed 15 m/s. Coherent and incoherent parts are obtained by sampling 40 surface realizations.

Next, the plane wave reconstruction of the fields over the vertical cross-section above the sea surface will be investigated. Figure 3.6 plots the total fields and the fields reconstructed using only the coherent components, as a function of the vertical height above the surface for a 1 GHz plane wave incident at 5°. Results for wind speeds of 5 m/s and 10 m/s are shown. The coherent components reconstruct well the total fields for the 5 m/s case, but not for the 10 m/s case. This is expected from a comparison of Figures 3.2 and 3.3. At 5 m/s the coherent scattered component is much greater than the incoherent spectrum, so most of the scattered power is coherent. But at 10 m/s the coherent scattered component is comparable to the incoherent spectrum, so more power is distributed in the incoherent field.

Since it is clear that in some cases the coherent field is insufficient for representing the total field, the following discrete plane wave expansion is considered:

$$E_y(x, z) \approx \sum_{m=1}^M A_m e^{-jk(x \cos \phi_m + z \sin \phi_m)}. \quad (3.7)$$

The discrete plane wave directions ϕ_m and the coefficients A_m are chosen to give the best reconstruction for a given number of plane waves M . The number of plane waves should be as small as possible since the goal of the plane wave expansion is to provide a ray-optical incident field for RCS codes, and efficiency is a primary concern. It would be inefficient, for example, to sample the continuous spectrum of (3.3) at the Nyquist rate and replace the integral with a summation. This is because the height h over which the expansion is needed to illuminate the target could be quite large in terms of wavelength, so a very large number of plane waves would be needed. Instead, it is possible to extract only the largest plane wave components from a given sea scattered spectrum using a simple feature extraction algorithm. Figure 3.7 shows the reconstruction of the 10 m/s field using the 50 strongest plane wave components, instead of just the coherent components as in Figure 3.6. The reconstruction agrees much better with the total field. This discrete plane wave expansion will be used as the incident field for computing the RCS of a target on the surface in Chapter 4.

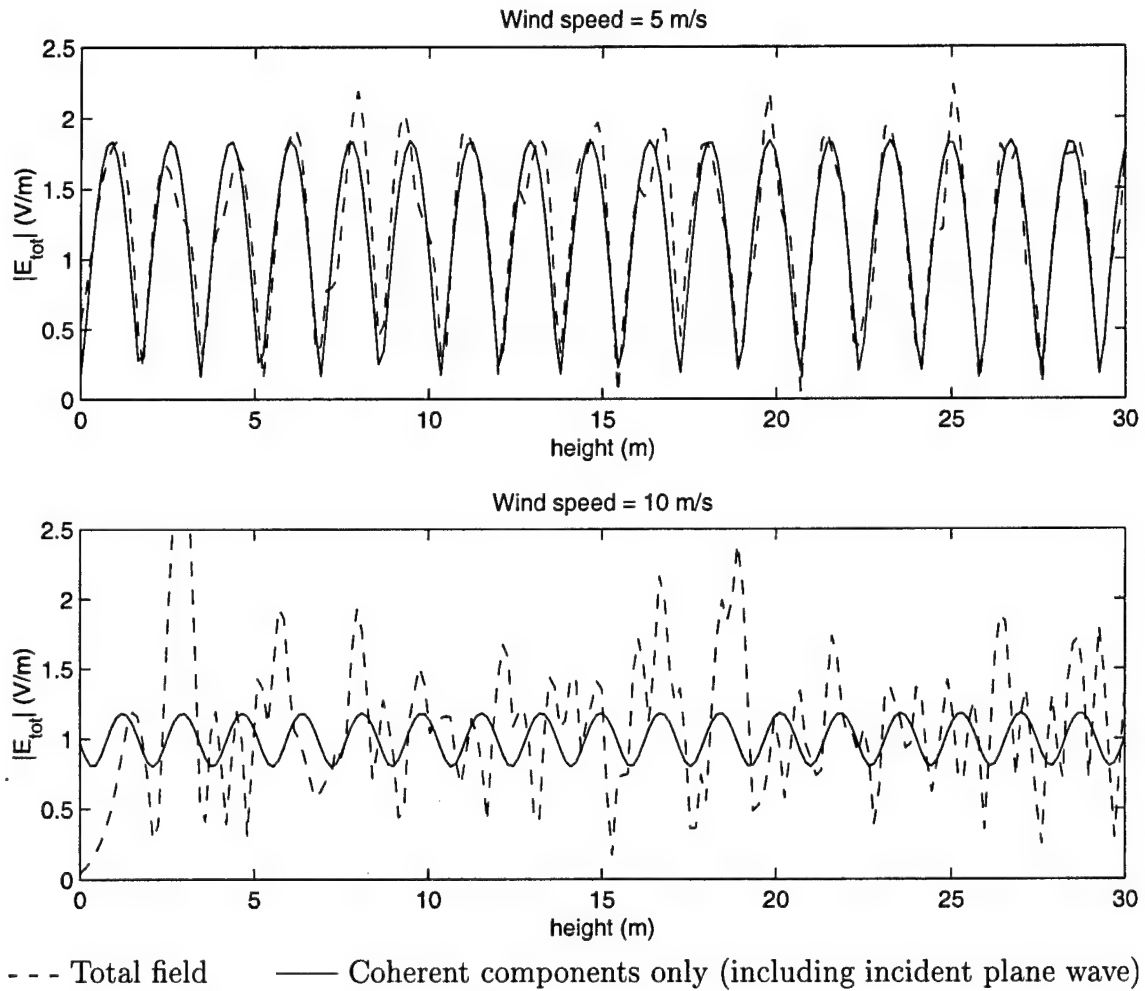


Figure 3.6: Coherent plane wave reconstruction of the total fields above the sea surface. Top: wind speed = 5 m/s. Bottom: wind speed = 10 m/s. Incident elevation angle = 5°, frequency = 1 GHz.

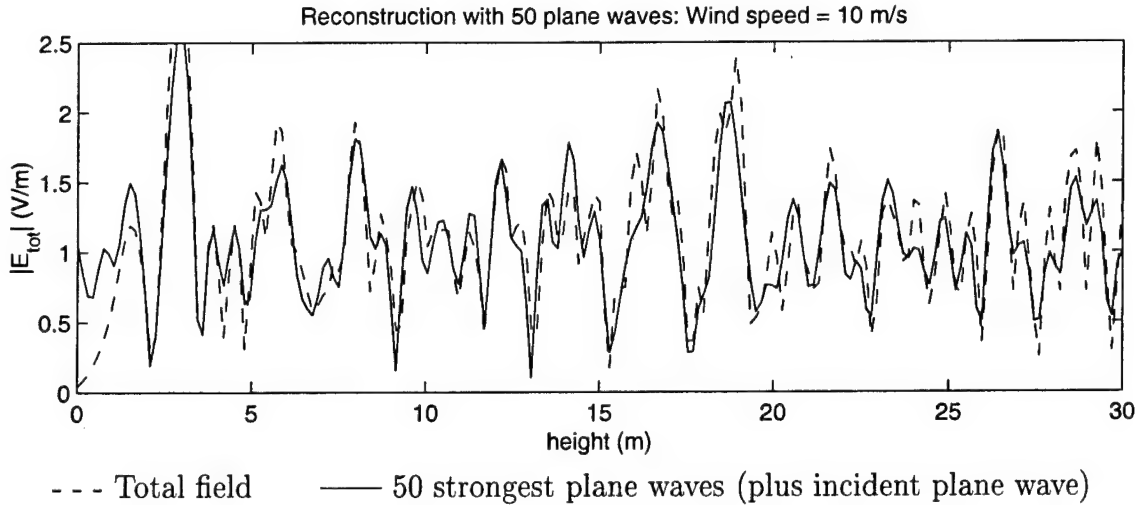


Figure 3.7: Reconstruction of the total fields above the sea surface using the 50 strongest plane wave components. Wind speed = 10 m/s. Incident elevation angle = 5° , frequency = 1 GHz.

3.3 Conclusions

It has been shown that the plane wave spectrum of the sea scattered field due to an incident plane wave may be decomposed into coherent and incoherent components. The coherent component is well predicted by the PO formula of (3.6), and may be stronger or weaker than the incoherent spectrum depending on the incidence angle, frequency, and wave height. As the incidence angle approaches grazing, the coherent component strength approaches the strength of the geometrical optics reflected field for a planar interface, so by conservation of power the incoherent component goes to zero. For shipboard surface-to-surface radar systems, the incidence angle is almost always very near grazing because the transmit antenna height is much, much smaller than the distance to the target. Even for air-to-surface radars the incidence angle is probably going to be very close to grazing for most problems of interest. Therefore, in most cases the coherent component is probably going to be sufficient for representing the sea scattered field in the vicinity of the target.

For cases when the coherent component alone does not accurately represent the sea scattered field, a discrete plane wave expansion may be used as in (3.7). A relatively small number of plane waves may be chosen if the strongest spectral components can be found from

a given spectrum. The possibility of using discrete plane waves with randomly generated amplitudes and phases is being investigated, and is based on ascertaining the probability distribution function of the sea scattered spectrum for a given wind speed. The effect of using the plane wave expansion to illuminate a target on a surface for the purpose of computing its RCS is investigated in the next chapter.

Chapter 4

Ship Radar Cross Section Computation Using Ray-Optical Methods

4.1 Introduction

In this chapter the RCS of a 2D target on a sea surface is computed using ray-optical methods that decouple the ship scattering problem from the sea surface scattering. First, the total incident field in the vicinity of the target (i.e., incident plane wave plus sea scattered field), but with the target absent, is expressed in terms of a discrete set of plane waves as in the last chapter. Next, the target is placed on an infinite planar interface and illuminated with the set of plane waves to find the scattered fields over the surface of the target. Lastly, the reciprocity theorem is used to find the backscattered field by reacting the incident field with the scattered field over the surface of the target. The reciprocity formulation is derived first in Section 4.2 because it defines the field quantities needed to compute the RCS. Then in Section 4.3 the approximately equivalent ray-optical scattering problem is presented. Numerical results are presented which compare the ray-optical results with rigorous numerical results generated using the spectrally accelerated GFB method. Conclusions follow at the end of the chapter.

4.2 Reciprocity Formulation for the Backscattered Field

4.2.1 Basic Derivation

The following derivation is for a three-dimensional geometry except where noted.

Figure 4.1 shows three different field configurations over the same sea surface. The top figure is the geometry of interest, which is a scattering target on the sea surface illuminated by an incident field generated by the antenna on the left, and the desired quantity is the scattered field (\bar{E}^s, \bar{H}^s) due to the *presence* of the target. The incident field (\bar{E}^i, \bar{H}^i) is defined as the field over the sea surface in the *absence* of the ship, and is illustrated in the middle figure. The total field is therefore,

$$(\bar{E}, \bar{H}) = (\bar{E}^i, \bar{H}^i) + (\bar{E}^s, \bar{H}^s)$$

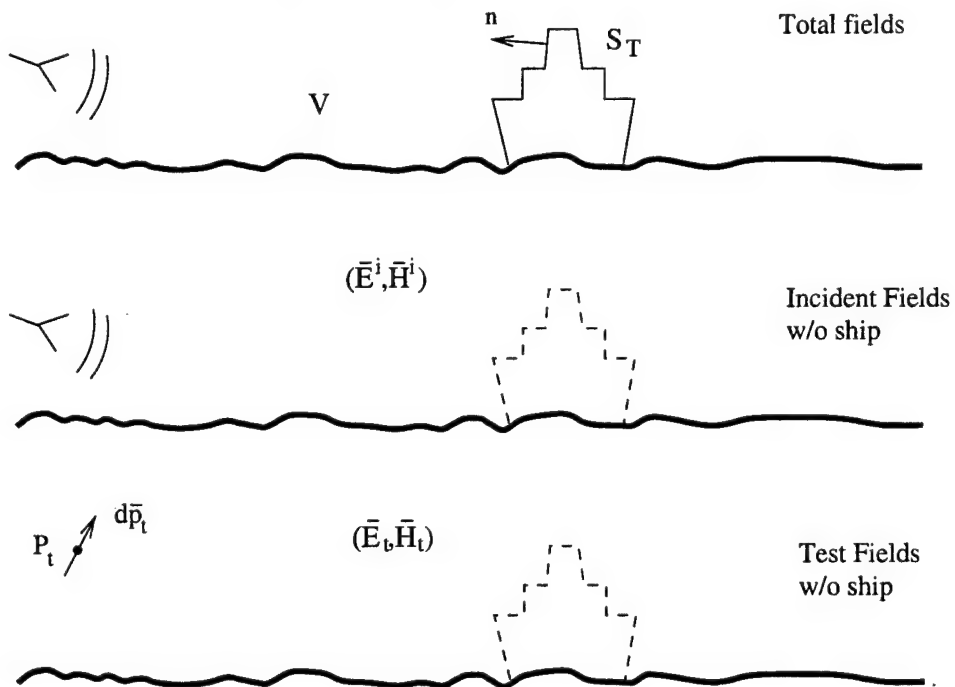


Figure 4.1: Sea surface and scattering target configurations for the reciprocity formulation. Top: incident and scattered fields with target present. Middle: Incident fields with target absent. Bottom: Fields of a test source with target absent.

$$(\bar{E}, \bar{H}) = (\bar{E}^i, \bar{H}^i) + (\bar{E}^s, \bar{H}^s). \quad (4.1)$$

It is of interest to compute the scattered electric field at some point P_t . To invoke reciprocity, we place an electric point dipole test source $d\bar{p}_t$ at P_t and define the fields (\bar{E}_t, \bar{H}_t) as the fields of this test source in the presence of the sea surface, but in the *absence* of the target, as illustrated in the bottom figure of Figure 4.1. Applying the reciprocity theorem [4] to the fields of the test source and the scattered fields within the volume V yields

$$d\bar{p}_t \cdot \bar{E}^s(P_t) = \int_{S_{sea} + S_\infty + S_T} (\bar{E}^s \times \bar{H}_t - \bar{E}_t \times \bar{H}^s) \cdot \hat{n} dS \quad (4.2)$$

where \hat{n} points into the volume V . The volume V contains the point P_t and is bounded by the target surface S_T , the sea surface S_{sea} outside of the target, and the surface at infinity S_∞ . The fields (\bar{E}^s, \bar{H}^s) and (\bar{E}_t, \bar{H}_t) satisfy the same boundary conditions on S_{sea} and S_∞ , so the surface integral vanishes on those surfaces leaving

$$d\bar{p}_t \cdot \bar{E}^s(P_t) = \int_{S_T} (\bar{E}^s \times \bar{H}_t - \bar{E}_t \times \bar{H}^s) \cdot \hat{n} dS \quad (4.3)$$

which is the form of interest. This equation states that the scattered electric field at P_t can be found by integrating the “reaction” of the scattered fields with the test fields over the target surface. (The reciprocity integral is sometimes called the *reaction integral*.) This is computationally significant because the target scattered fields only need to be found on the surface of the target, and do not need to be tracked from the target back to the observer. The expression of (4.3) is an exact formulation derived directly from Maxwell’s equations and from the boundary conditions on the sea surface and at infinity. An approximation will be used later to compute the scattered fields (\bar{E}^s, \bar{H}^s) on the surface of the target.

4.2.2 Simplification for Plane Wave Backscattering

For backscattering problems the formulation is even simpler because the incident source may be used as the test source, so $(\bar{E}_t, \bar{H}_t) = (\bar{E}^i, \bar{H}^i)$. A plane wave incident field is generated by placing a dipole source at infinity, as shown in Figure 4.2. The dipole \hat{p} is assumed to have unit strength and is placed at \bar{r} , $r \rightarrow \infty$ with respect to the reference origin O . The plane wave incident electric field at a O as shown in the figure is then given by

$$\bar{E}_o^i(O) = \lim_{r \rightarrow \infty} -\hat{p} \frac{jkZ_o e^{-jkr}}{4\pi} \frac{e^{-jkr}}{r}. \quad (4.4)$$

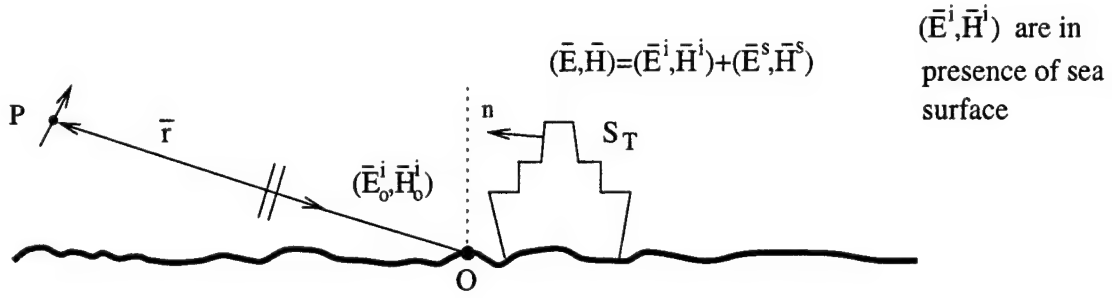


Figure 4.2: Plane wave backscattering configuration for the reciprocity formulation.

The reciprocity equation then becomes

$$\hat{p} \cdot \bar{E}^s(\bar{r}) = \lim_{r \rightarrow \infty} -\frac{jkZ_o}{4\pi r} e^{-jkr} \int_{S_T} (\bar{E}^s \times \bar{H}^i - \bar{E}^i \times \bar{H}^s) \cdot \hat{n} dS \quad (4.5)$$

where (\bar{E}^i, \bar{H}^i) are the fields due to the incident plane wave, *phase-referenced to point O*, in the presence of the sea surface. This equation may be used directly for backscatter RCS computations. It is only necessary to find the scattered fields (\bar{E}^s, \bar{H}^s) over the target surface due to the incident fields (\bar{E}^i, \bar{H}^i) . For 2D scattering problems, a line source replaces the point source and the factor $\frac{jkZ_o}{4\pi r}$ is replaced with $Z_o \sqrt{\frac{jk}{8\pi r}}$

4.2.3 Equivalent Current Form for a PEC Target

Equivalent surface currents are often used in RCS computation methods, such as in physical optics (PO) [3] and the method of moments [7]. For a PEC target, the equivalent magnetic surface current is zero and the electric current is given by

$$\bar{J}_s = \hat{n} \times \bar{H} \quad (4.6)$$

where \bar{H} is the total field. In the integrand of (4.5), for a PEC target it may be shown that

$$\begin{aligned} (\bar{E}^s \times \bar{H}^i - \bar{E}^i \times \bar{H}^s) \cdot \hat{n} &= [-\bar{E}^i \times \bar{H}^i - \bar{E}^i \times (\bar{H} - \bar{H}^i)] \cdot \hat{n} \\ &= -\bar{E}^i \times \bar{H} \cdot \hat{n} \\ &= \bar{E}^i \cdot \bar{J}_s \end{aligned} \quad (4.7)$$

so (4.5) becomes

$$\hat{p} \cdot \bar{E}^s(\bar{r}) = \lim_{r \rightarrow \infty} -\frac{jkZ_o}{4\pi r} e^{-jkr} \int_{S_T} \bar{E}^i \cdot \bar{J}_s dS. \quad (4.8)$$

The problem is reduced to finding \bar{J}_s over the target surface. It must be noted that \bar{J}_s is found in the presence of the sea surface, so the usual equivalent current methods must be modified. For example, the electric field integral equation (EFIE) [7] for this problem is given by

$$-\hat{n} \times \bar{E}^i = \hat{n} \times \int_{S_T} \bar{J}_s \cdot \bar{\bar{G}}_{sea} dS \quad (4.9)$$

where $\bar{\bar{G}}_{sea}$ is the dyadic Green's function for the space above the sea surface instead of the usual free space dyadic Green's function $\bar{\bar{G}}_o$.

4.2.4 Local Planar Approximation for Sea Surface

Since the Green's function for a rough surface is not easy to find, an approximation may be used which assumes the surface is locally flat *only* for the purposes of finding \bar{J}_s in (4.9). The incident field \bar{E}^i is still in the presence of a rough surface. With this approximation, the sea surface dyadic Green's function in (4.9) is replaced with:

$$\bar{\bar{G}}_{sea} \approx \bar{\bar{G}}_o + \bar{\bar{G}}_I \quad (4.10)$$

where $\bar{\bar{G}}_I$ is the image dyadic Green's function as shown in Figure 4.3. Using image theory [4], the image of the incremental current element generates the reflected field. It is noted that $\bar{\bar{G}}_I$ must take into account the reflection coefficient from the planar interface if it is not PEC. The image approach is not exact for non-PEC interfaces, but should be a good approximation if the interface is of a highly impenetrable material such as sea water. The reciprocity integral for plane wave incidence (4.9) becomes

$$-\hat{n} \times \bar{E}^i = \hat{n} \times \int_{S_T} (\bar{J}_s \cdot \bar{\bar{G}}_o + \bar{J}_s \cdot \bar{\bar{G}}_I) dS. \quad (4.11)$$

4.3 Equivalent Ray-Optical Scattering Problem

In this section the discrete plane wave expansion of (3.7) in Chapter 3 is used to define the incident field in the local planar approximation for the EFIE (4.11) for finding the equivalent

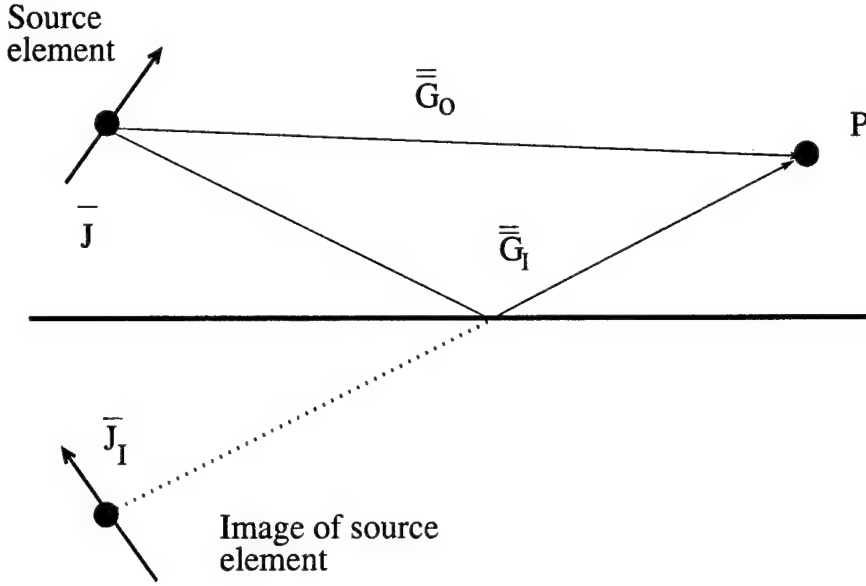


Figure 4.3: Local planar approximation for the sea surface and image theory used to find the scattered fields in the vicinity of the target.

currents over the target surface. Referring to Figure 4.4, the incident fields at a point \bar{r}' on the target surface are given by

$$\begin{aligned}\bar{E}^i(\bar{r}') &= \sum_{m=0}^M \hat{p}_m A_m e^{-j\bar{k}_m \cdot \bar{r}'} \\ \bar{H}^i(\bar{r}') &= \sum_{m=0}^M \bar{k}_m \times \hat{p}_m \frac{1}{kZ_o} A_m e^{-j\bar{k}_m \cdot \bar{r}'}\end{aligned}\quad (4.12)$$

where for the m^{th} plane wave, \hat{p}_m is the unit electric polarization vector, \bar{k}_m is the propagation vector ($|\bar{k}_m| = k$), and A_m is the bistatic sea scattering coefficient in the direction of \bar{k}_m . The $m = 0$ term is the original incident plane wave, and the $m > 0$ terms are the sea scattered plane waves. For the case when only the coherent components are used, $M = 1$ and $\bar{k}_1 = \bar{k}_o - 2(\hat{z} \cdot \bar{k}_o)\hat{z}$ (where \hat{z} points straight up), and $A_1 = \Gamma(\bar{k}_o)$ from Equation (3.6).

Using the above ray-optical incident field expansion, the EFIE of (4.11) is solved numerically for \bar{J}_s over the ship surface using the MoM [7] or approximately using a high-frequency method such as physical optics [3]. It is also possible to use (4.5) directly to find the scattered fields using high-frequency methods, without the intermediate step of first solving for equivalent currents. In the numerical results of the next section the MoM is used. It is noted

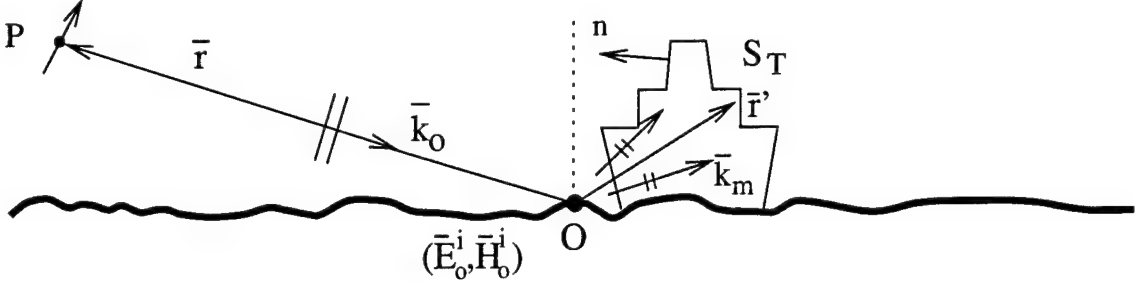


Figure 4.4: Target illuminated by a discrete set of plane waves.

again that (4.11) is solved in the presence of a locally flat surface using the image Green's function. This allows the target scattering problem to be solved approximately, independent of the exact rough sea surface.

As an example of a high-frequency solution using physical optics [3], the surface currents may be found approximately by

$$\bar{J}_s(\bar{r}') \approx 2\hat{n} \times \bar{H}_{GO}^i(\bar{r}') \quad (4.13)$$

where $\bar{H}_{GO}^i(\bar{r}')$ is the geometrical optics (GO) component of the incident field. In terms of the plane wave expansion of (4.12), the PO currents are given by

$$\bar{J}_s(\bar{r}') \approx \sum_{m=0}^M \begin{cases} \hat{n} \times (\bar{k}_m \times \hat{p}_m) \frac{2}{kZ_o} A_m e^{-j\bar{k}_m \cdot \bar{r}'} & : \text{lit region of } m^{\text{th}} \text{ plane wave,} \\ 0 & : \text{shadow region of } m^{\text{th}} \text{ plane wave.} \end{cases} \quad (4.14)$$

In the above the “lit” region is defined as points \bar{r}' on the surface of the target where the GO field is non-zero. As with the EFIE, the GO field must also include the locally planar surface during the ray tracing process, as illustrated in Figure 4.5. It is possible that a GO ray may reflect from the target and hit the sea surface, then hit the target again as shown. The second hit on the target would also contribute to \bar{J}_s in the PO approximation. This contribution is important to include because the ship hull and its image could form a large corner reflector, which would likely be the dominant backscatter mechanism for the target.

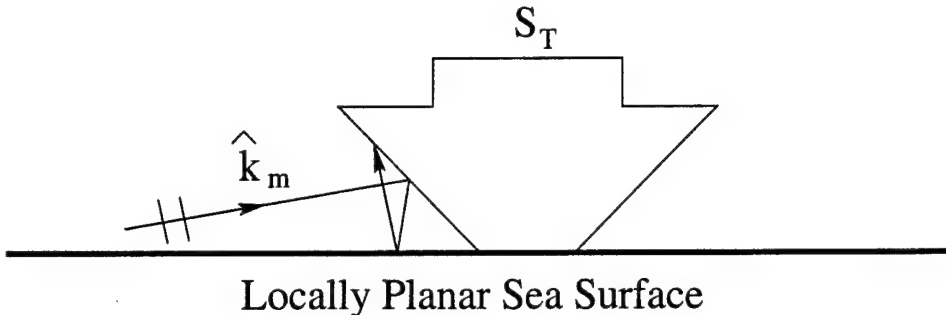


Figure 4.5: GO ray from the m^{th} incident plane wave which reflects from the target, hits the sea surface, and then hits the target again.

4.4 Numerical Results

In the numerical results of this section the general 3D formulations of the previous section are converted to 2D, and the electric field is horizontally polarized (i.e., $\hat{p}_m = \hat{y}$ and $\hat{p}_m \cdot \bar{k}_m = 0$) as in Chapters 2 and 3. The equivalent surface currents on the target are found using (4.11) with (4.12) representing the incident fields, and the backscattered fields are found using (4.8). The 2D RCS, or more specifically, the 2D radar echo width, is defined by

$$\text{RCS}_{2D} = \lim_{r \rightarrow \infty} 2\pi r \left| E_y^s(\bar{r}) \right|^2. \quad (4.15)$$

Using the 2D form of (4.8) for horizontal polarization this becomes

$$\text{RCS}_{2D} = \frac{k Z_o^2}{4} \left| \int_{S_T} E_y^i J_s \, dS \right|^2 \quad (4.16)$$

where J_s is the scalar portion of \bar{J}_s which is \hat{y} -directed.

The frequency is 1 GHz in all the results of this section. The reference RCS results predicted by the GFB method are for the total backscatter from the ship and sea surface together. However, as shown in the results of Chapter 2, the backscatter from the sea surface is generally more than 30 dB below the backscatter from the ship.

To establish an accuracy bound on the GFB reference solution, Figure 4.6 plots the 2D RCS of the 13 m high ship target on a 402.4 m flat sea surface computed using the spectrally accelerated GFB method. The 2D ship geometry is shown in the figure above the plot; the hull makes an angle of 80° with the horizontal axis. The plane wave is incident from the left.

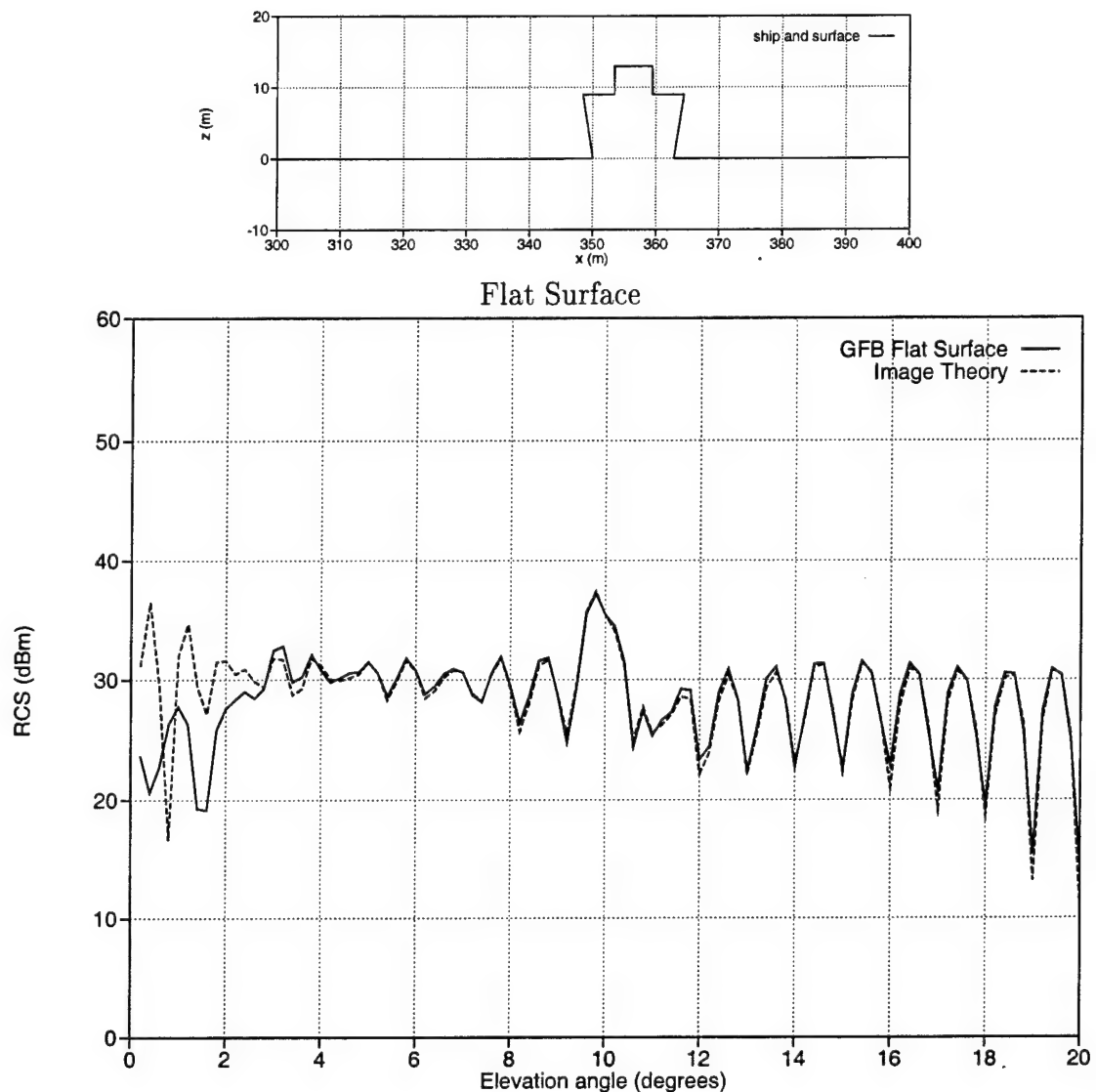


Figure 4.6: 2D RCS of a 13 m high ship on a 402.4 m flat surface computed using GFB and image theory. Frequency = 1 GHz.

Also plotted is a reference solution computed using exact image theory for the ship on an infinite flat surface. It is noted that for a flat sea surface the sea scattered incident field is entirely coherent. Notice the large peak around 10° which is due to the sea reflected plane wave hitting the ship hull broadside. There is excellent agreement everywhere except below about 3° . This is due to the fact that the GFB uses a finite flat surface (with R-cards on the ends), whereas the image theory result assumes an infinite surface. The GFB solution could be improved for low angles by using a larger sea surface, but at the expense of increased CPU time. As an example of the CPU time required, the spectrally accelerated GFB result took 2 hours to compute on a 450 MHz Pentium II processor, and the image theory result about 2 minutes. The patterns are sampled at 0.2° increments. These times are typical of all the results of this chapter—2 hours for GFB RCS patterns and 2 minutes for coherent RCS patterns.

Figure 4.7 plots the 2D RCS of the 13 m high ship target on a 402.4 m sea surface with wind speed 5 m/s (RMS wave height $\sigma = 0.14$ m, $\sigma/\lambda = 0.47$). The ship geometry and the last 100 m of sea surface are shown above the plot. The solid line is the GFB reference solution, and the dashed line is the RCS computed using only the coherent components of the incident field (in the presence of the sea surface) and uses the local planar approximation of (4.11) solved using the MoM. The coherent component of the sea scattered incident field is found from the formula of (3.6). The agreement is good for low angles (except for the discrepancies at very low angles due to the finite surface), but the coherent result generally under-predicts the RCS at higher angles. This is expected from (3.6) since the coherent component becomes weaker as the elevation angle increases.

Figure 4.8 shows the same RCS result, but the dashed line is computed using the 50 strongest plane wave components to represent the sea scattered incident field (in addition to the incident plane wave \bar{k}_o). The plane wave amplitudes are found by extracting the strongest spectral components of the sea scattered field with the ship absent, which was computed using the FB method. The overall agreement with the reference GFB solution does not improve much compared with the coherent result, although the envelope of the

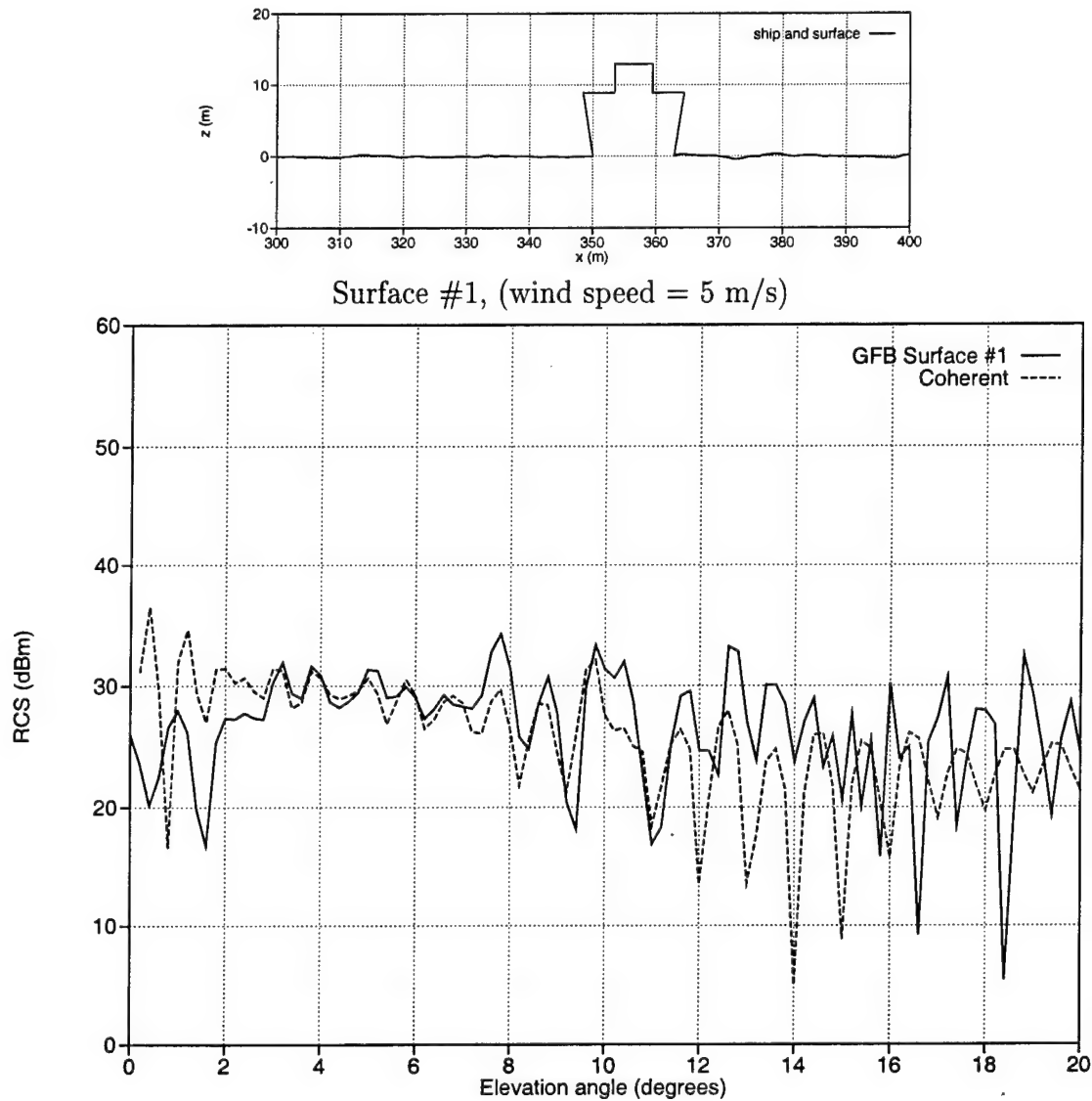


Figure 4.7: 2D RCS of a 13 m high ship on a 402.4 m surface computed using coherent components of sea scattered incident field. Wind speed = 5 m/s, frequency = 1 GHz.

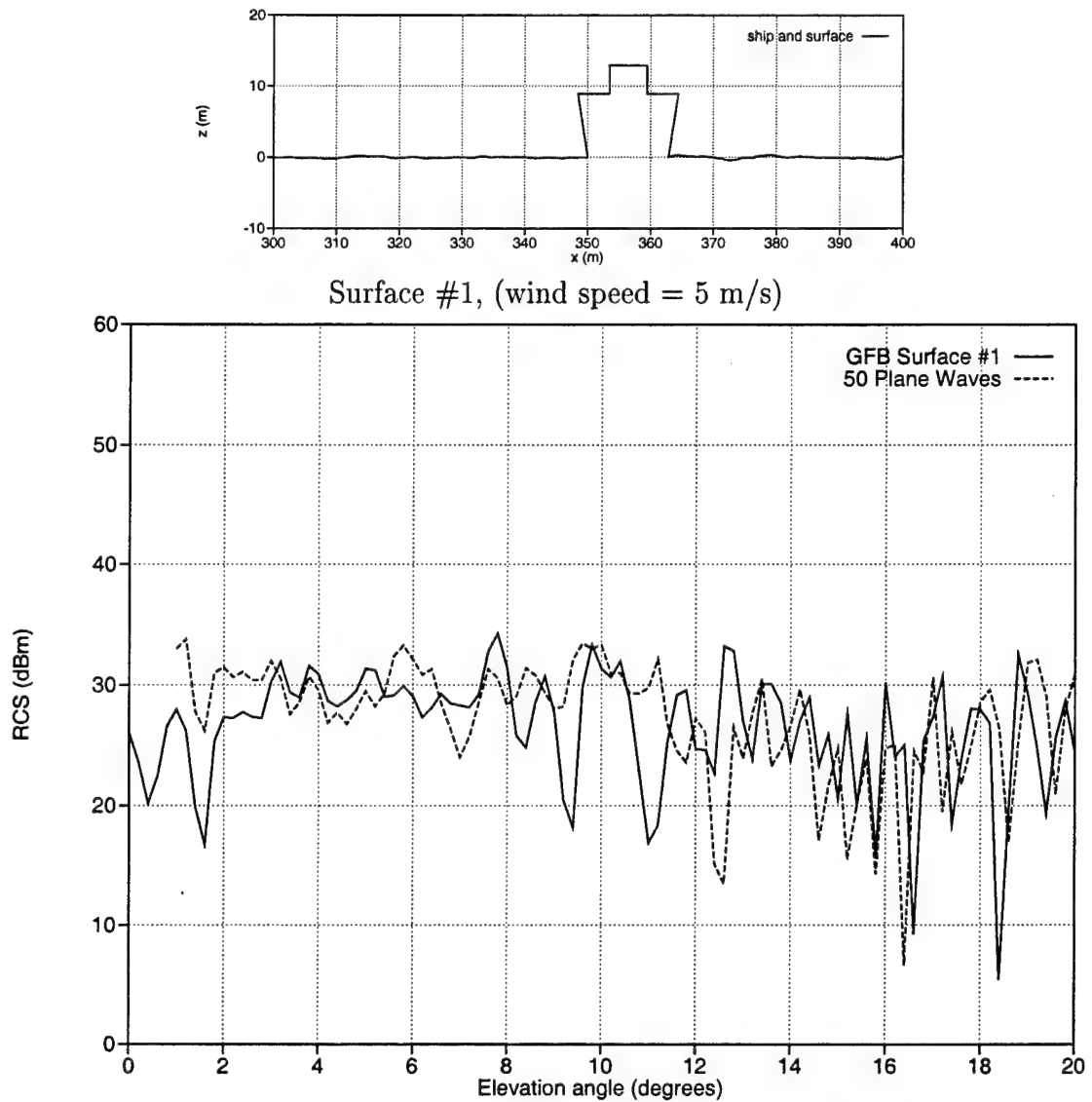


Figure 4.8: 2D RCS of a 13 m high ship on a 402.4 m surface computed using 50 strongest plane wave components of sea scattered incident field. Wind speed = 5 m/s, frequency = 1 GHz.

patterns appears to agree better for higher angles. The RCS is generally not under-predicted in this plot, except for a few isolated angles. This is important because the purpose of the approximate ray-optical methods is to predict the peak levels and range of variation of the RCS pattern.

Figure 4.9 shows the RCS computed using the numerically exact incident field obtained from the FB method. The results are very similar to the 50 plane wave incident field representation, indicating again that the plane waves adequately reconstruct the sea scattered incident field. The differences with the GFB reference solution are due entirely to the local planar approximation used to find the scattered fields over the surface of the target, which seems to mostly effect the details of the pattern and not the overall envelope.

Figure 4.10 shows the RCS of the 13 m ship computed using the GFB method for a flat surface and for Surface #1 (wind speed = 5 m/s). Also plotted is the RCS computed using only the coherent component of the incident field. This figure shows that the envelope of the RCS pattern for the rough surface is generally bounded above by the envelope of the flat surface pattern, and below by the envelope of the coherent pattern. Also notice that the two GFB results agree very well for low angles because they both include the effects of using a finite sea surface for the computations.

To see if the envelope agreement holds up for a different randomly generated surface with the same wind speed, Figure 4.11 shows the same results for Surface #2 which is shown above the plot. The two GFB results agree quite well for this case, and the envelopes of the flat and coherent results provide an upper and lower bound for the rough surface RCS plot.

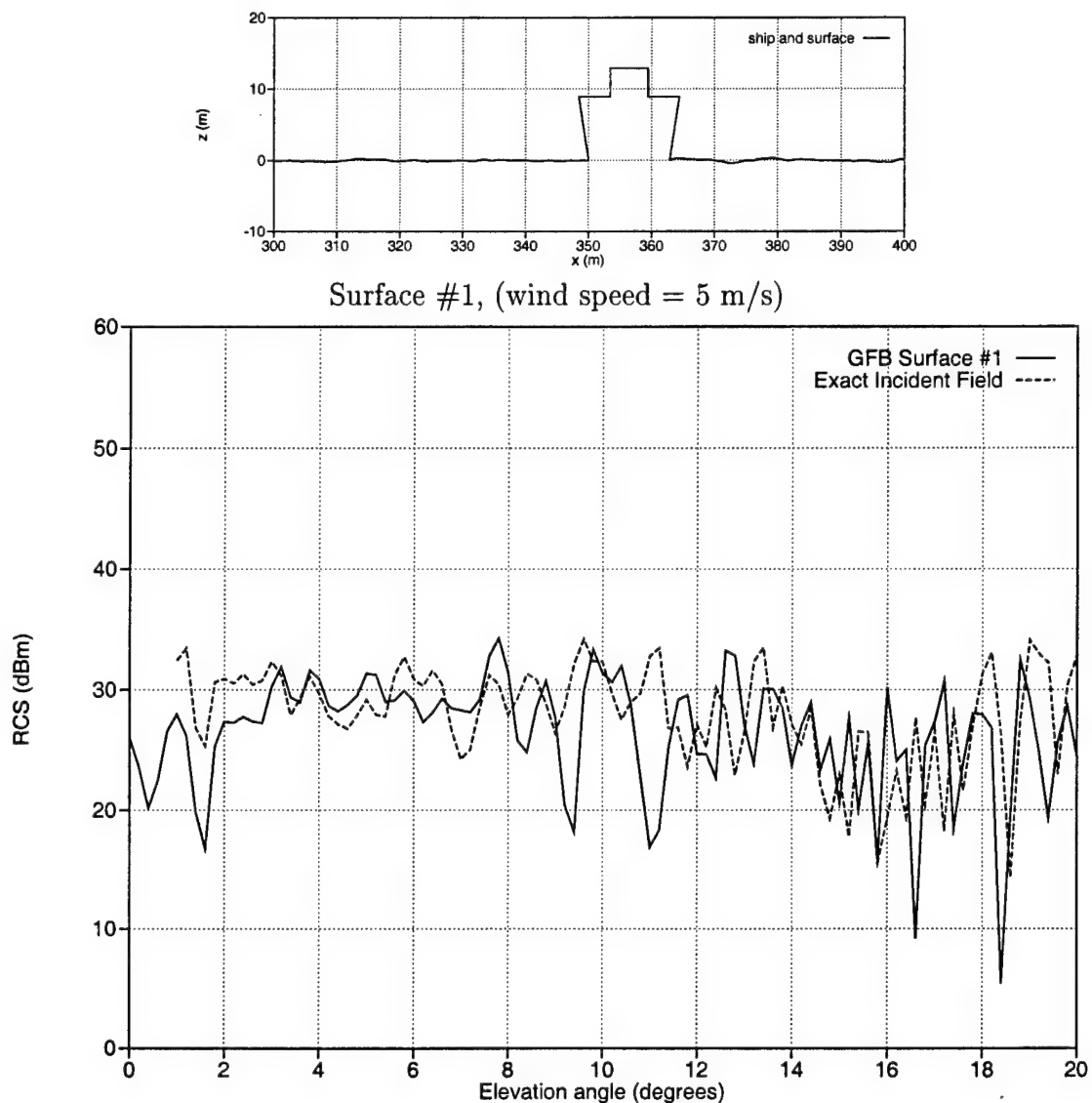


Figure 4.9: 2D RCS of a 13 m high ship on a 402.4 m surface computed using the numerically exact sea scattered incident field. Wind speed = 5 m/s, frequency = 1 GHz.

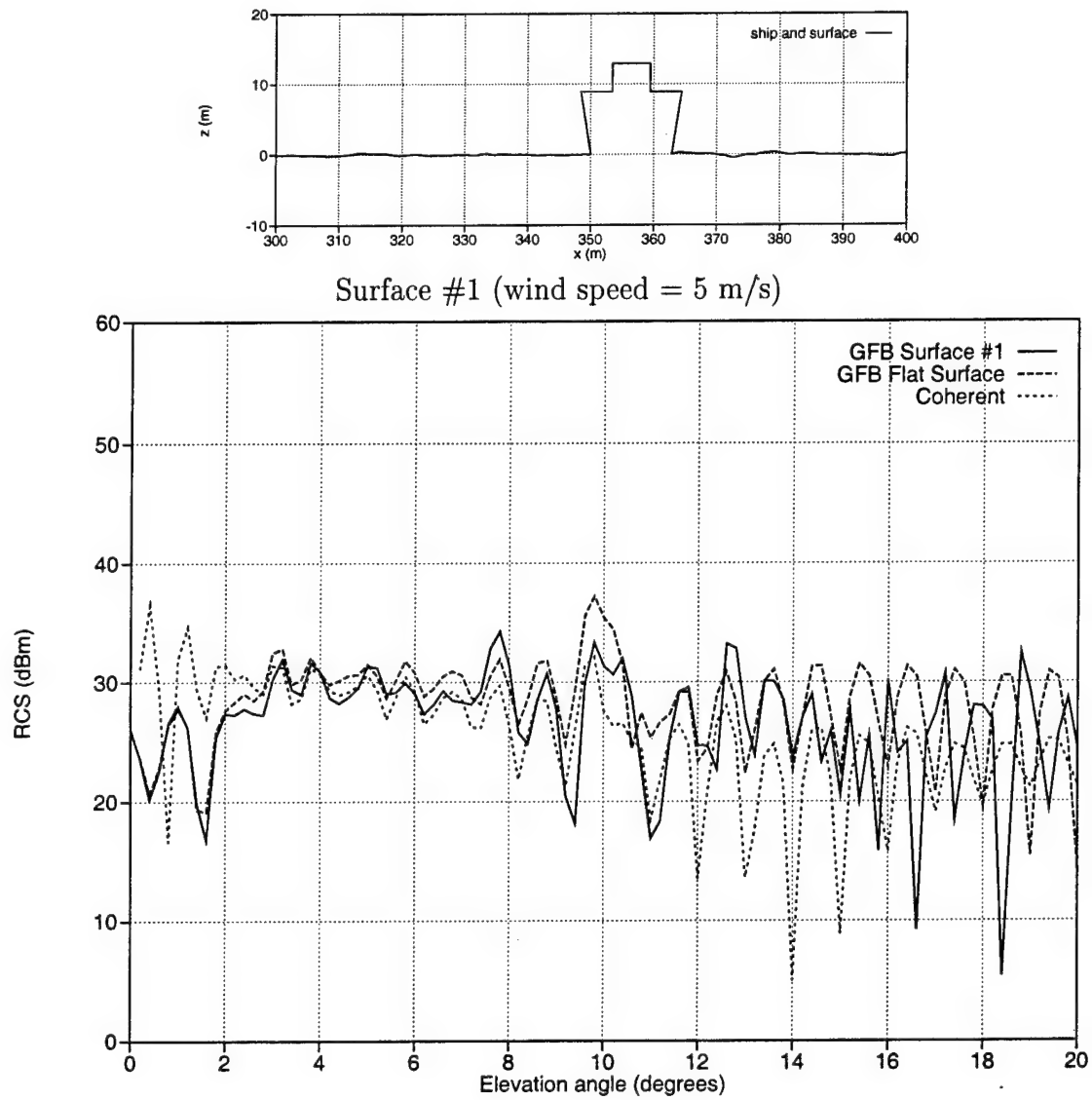


Figure 4.10: 2D RCS of a 13 m high ship on a 402.4 m surface computed using GFB for a flat surface and a rough surface. Wind speed = 5 m/s, frequency = 1 GHz.

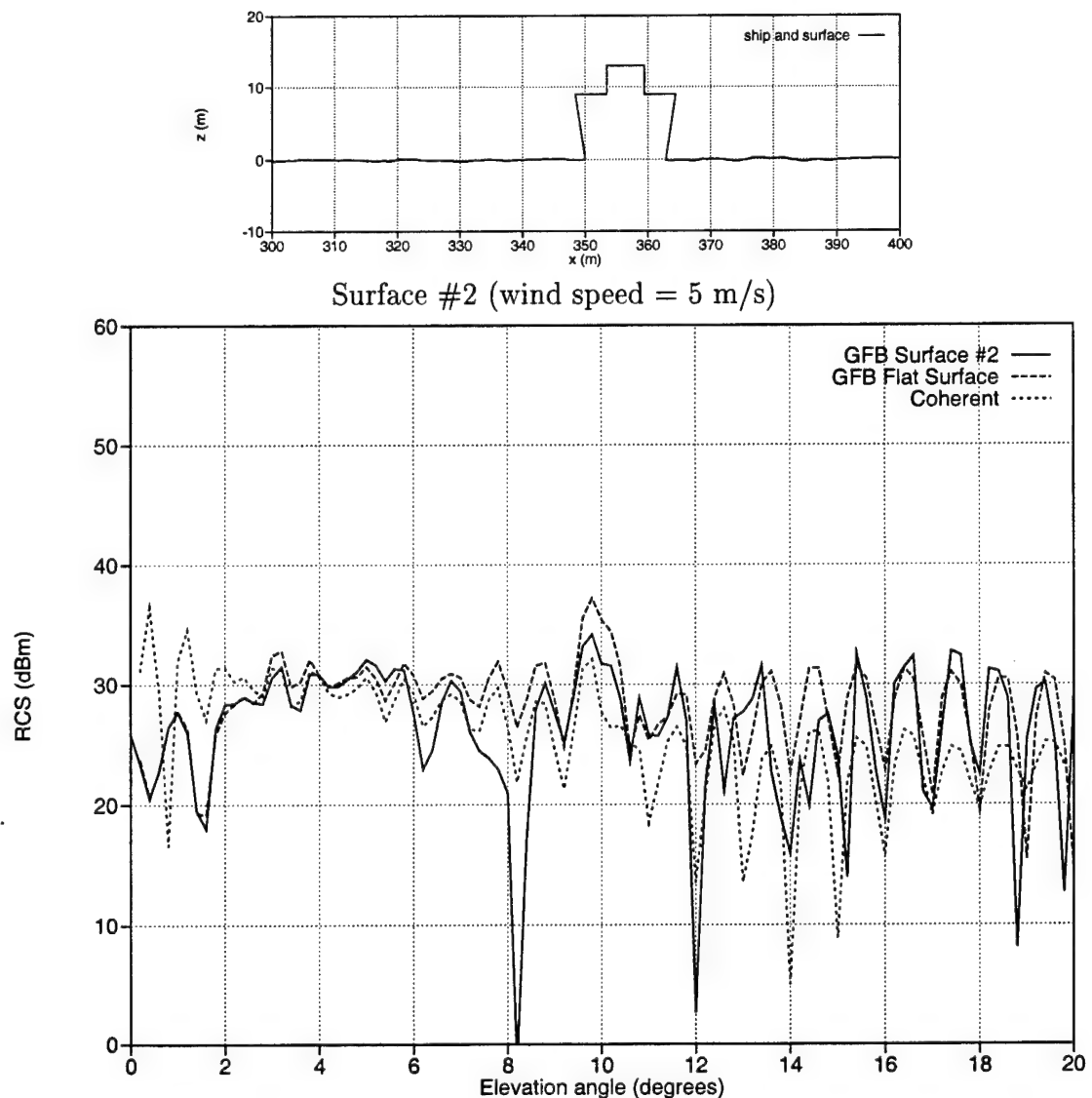


Figure 4.11: 2D RCS of a 13 m high ship on a 402.4 m surface computed using GFB for a flat surface and a rough surface. Wind speed = 5 m/s, frequency = 1 GHz.

To investigate further the envelope behaviors of the RCS patterns, Figure 4.12 shows the RCS of the 13 m ship on a surface with a wind speed of 10 m/s (RMS wave height $\sigma = 0.54$ m, $\sigma/\lambda = 1.8$), and Figure 4.13 shows the RCS for a wind speed of 15 m/s (RMS wave height $\sigma = 1.22$ m, $\sigma/\lambda = 4.1$). The ship geometry (which is the same) and the last 200 m of the sea surface are shown above the plots. Again, the flat surface and coherent results are also plotted. The envelope of the rough surface RCS patterns generally lie between the flat surface and coherent envelopes, and the overall level of the flat surface pattern is in good agreement with the level of the rough surface pattern. The patterns generally show more variation in the RCS at higher wind speeds, especially at lower elevation angles.

Figure 4.14 shows the same results as Figure 4.13 but for a different randomly generated surface at the same wind speed of 15 m/s. Even though the patterns for Surface #4 and Surface #5 are significantly different, the same conclusions about the envelope levels seem to be confirmed.

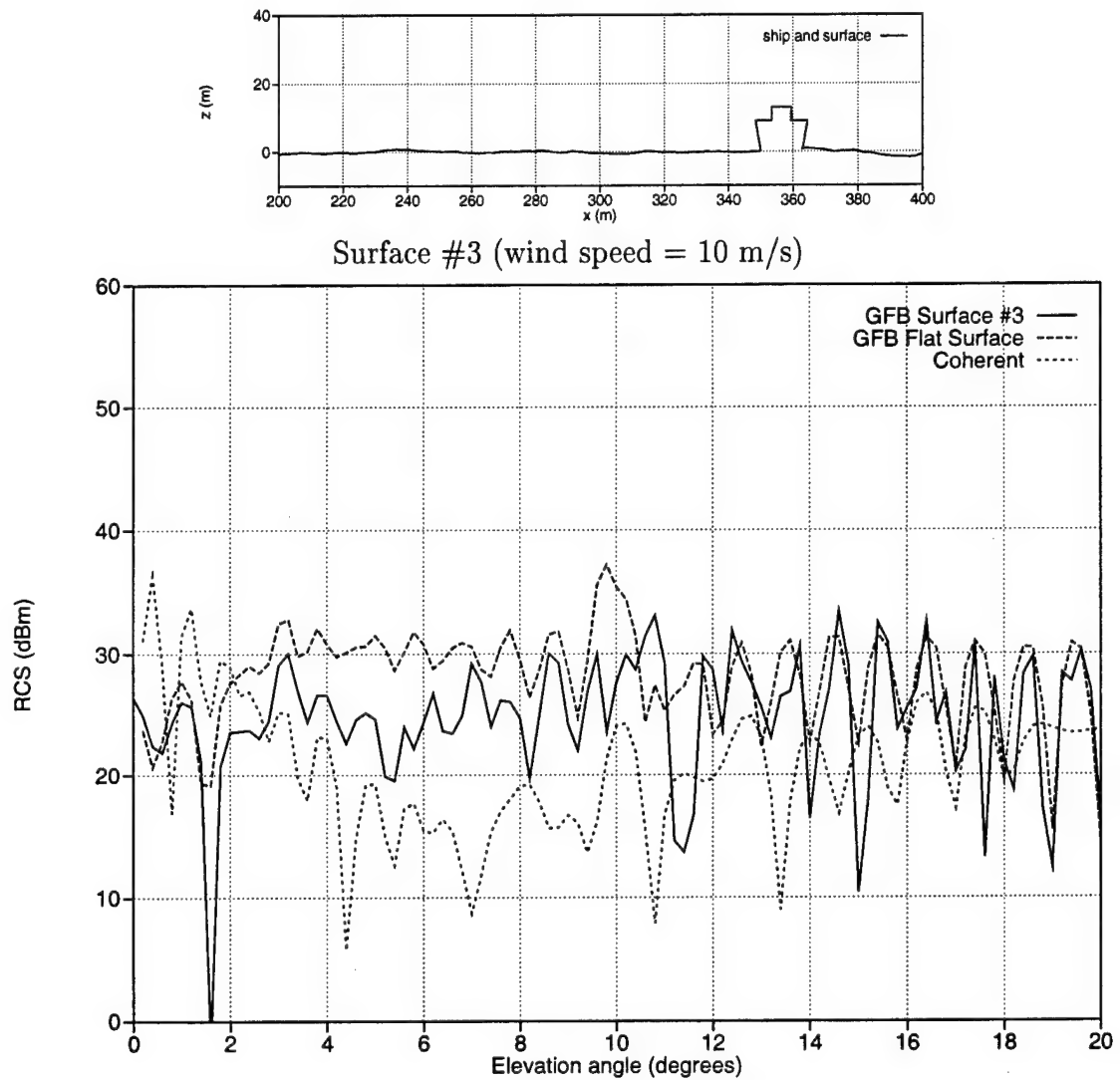


Figure 4.12: 2D RCS of a 13 m high ship on a 402.4 m surface computed using GFB for a flat surface and a rough surface. Wind speed = 10 m/s, frequency = 1 GHz.

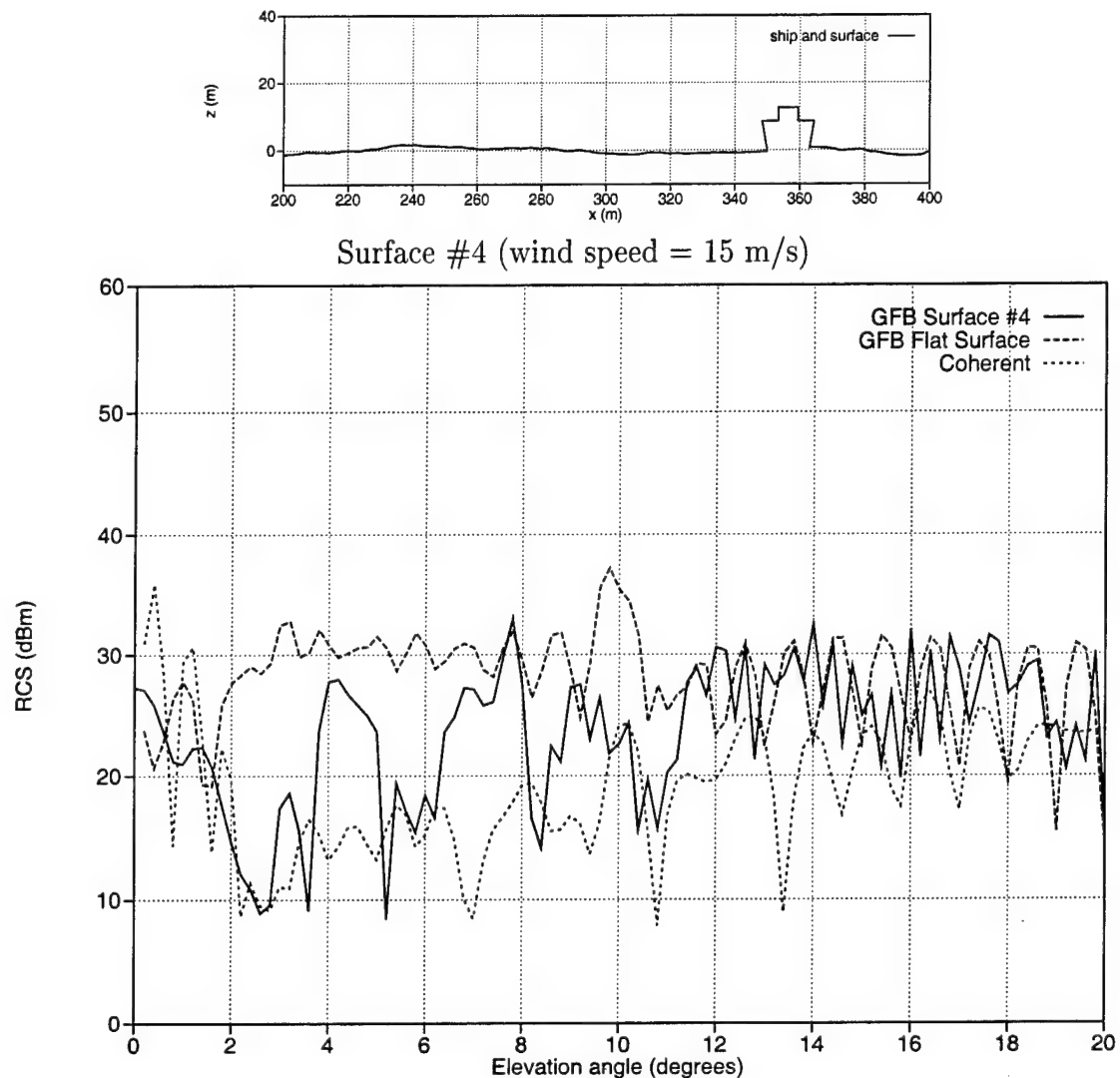


Figure 4.13: 2D RCS of a 13 m high ship on a 402.4 m surface computed using GFB for a flat surface and a rough surface. Wind speed = 15 m/s, frequency = 1 GHz.

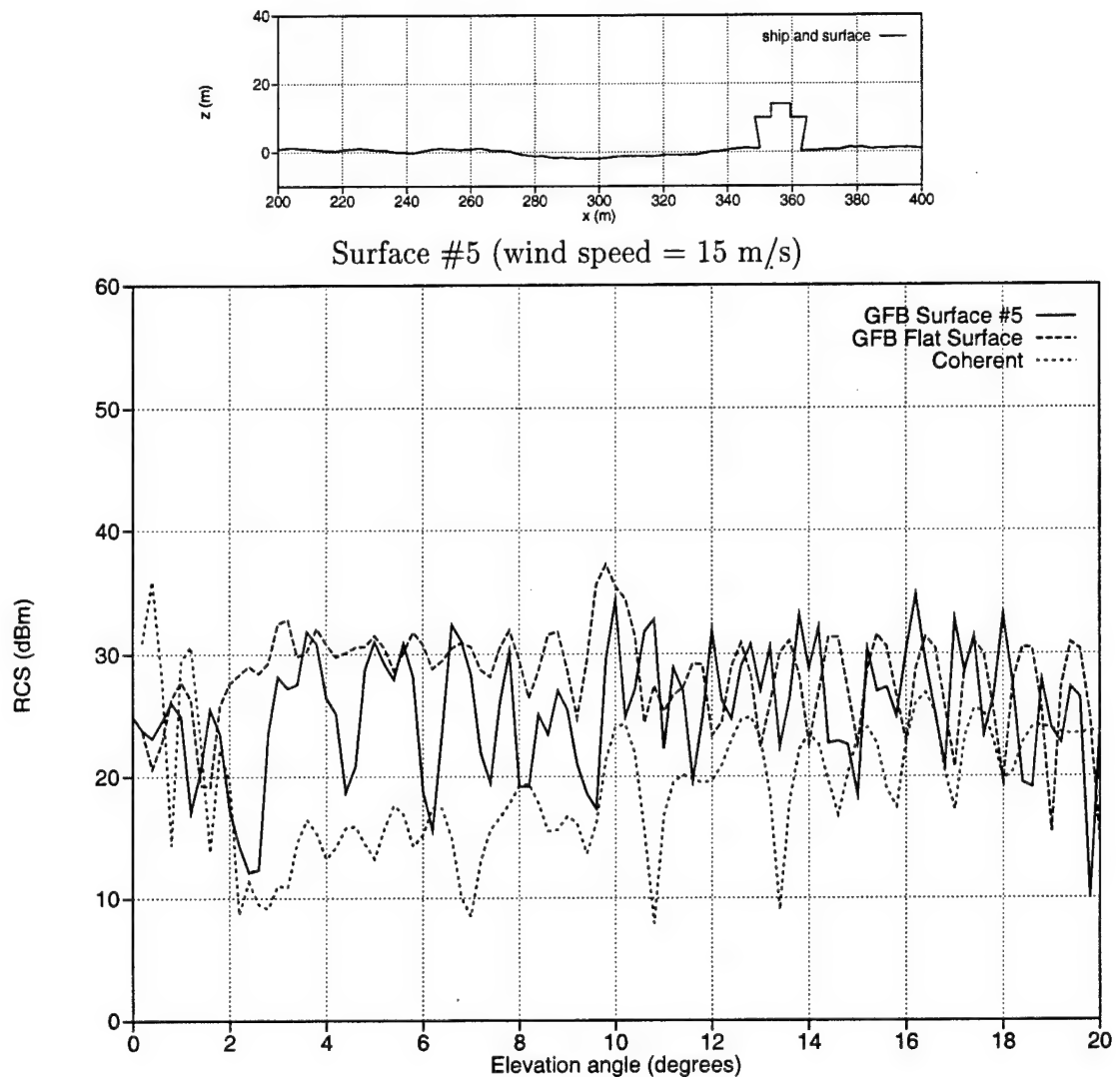


Figure 4.14: 2D RCS of a 13 m high ship on a 402.4 m surface computed for flat case, coherent case, and rough surface case. Wind speed = 15 m/s, frequency = 1 GHz.

All of the previous results are for the same ship with a hull angle of 80° with respect to the sea surface. It may be noticed that the peak levels and the variations of the RCS patterns for this target at different wind speeds are about the same, even for zero wind speed (flat surface). Figure 4.15 plots the RCS patterns for a hull angle of 90° , with the rest of the topside ship geometry unchanged. The wind speed is 15 m/s, and the sea surface is the same as in Figure 4.13 (Surface #4). The 90° hull angle is a pathological case (and is often encountered) because the side of the ship forms a large corner reflector with a flat sea surface, so the RCS is expected to be very high. The GFB Flat Surface result confirms this. Unlike the previous target with an 80° hull angle, the rough surface greatly reduces the peak RCS levels for this target. The rough surface result is bounded by the flat surface and coherent results as before, although the space between them is much larger.

Lastly, it is of interest to investigate the use of a high-frequency asymptotic technique for computing the RCS of a simple target geometry. Figure 4.16 plots the RCS of a flat-top ship on a flat surface (shown above the plot), computed using the EFIE from (4.11) and physical optics from (4.14). It is noted that for this flat surface case only the incident and direct reflected plane waves are used. The ship is 9 m high and the hull makes an angle of 80° with the surface. The PO solution is first order, so multi-bounce effects are not included. The agreement between the numerically exact EFIE solution and the approximate PO solution is very good. The strong peak around 10° is due to the sea-reflected plane wave hitting the hull broadside.

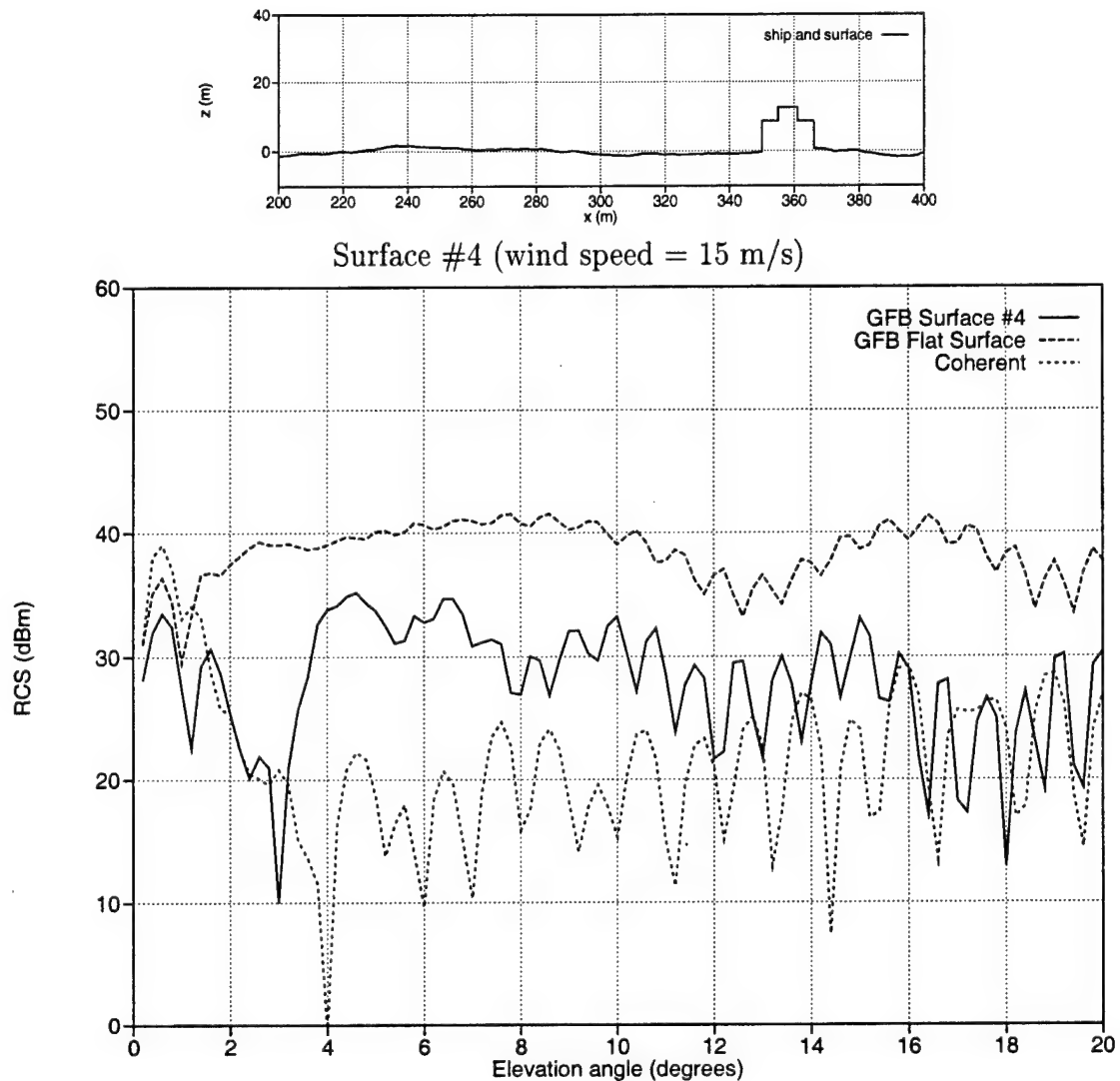


Figure 4.15: 2D RCS of a 13 m high ship with a 90° hull angle on a 402.4 m surface computed for flat case, coherent case, and rough surface case. Wind speed = 15 m/s, frequency = 1 GHz.

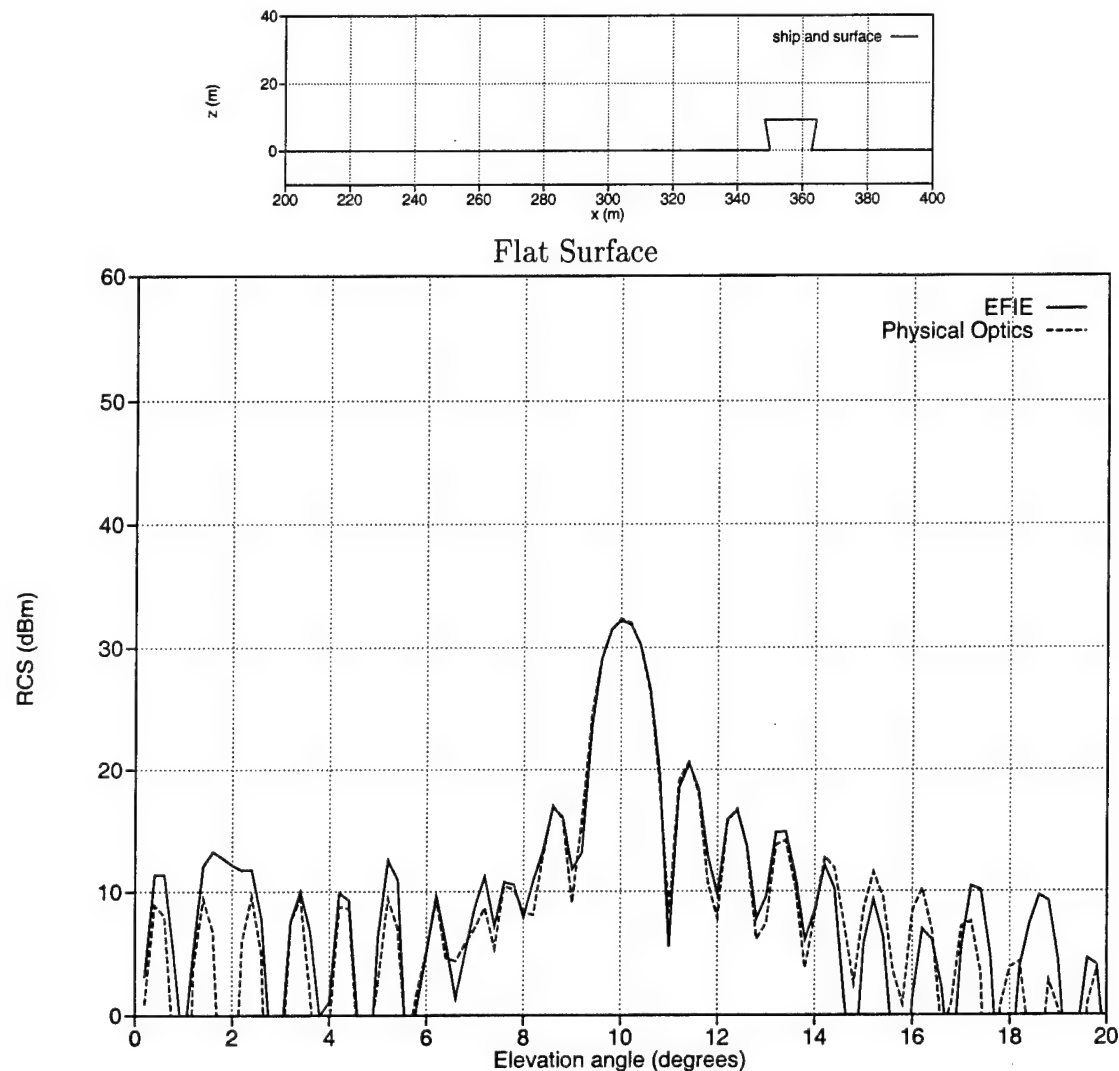


Figure 4.16: 2D RCS of a 9 m high ship on a 402.4 m flat surface computed with the EFIE and physical optics. Frequency = 1 GHz.

4.5 Conclusions

The numerical results show that computing the RCS of a target on a rough surface using only the incident plane wave and the coherent plane wave component of the sea scattered field to illuminate the target, generally under-predicts the actual RCS level. Using more plane waves to characterize the sea scattered field raises the RCS level to where it should be, but the details of the pattern are not recovered. Of course, the advantage of using plane waves to characterize the sea scattered field which illuminates the ship is the great reduction in CPU time, because the sea surface is then decoupled from the ship scattering calculation. What is important is that the ray-optical results predict the peak levels of the RCS patterns and the range of variation.

The numerical results also show that the RCS of a target on a rough surface is generally bounded above by the RCS of the same target on a flat surface. However, as in the case with the 90° hull angle (corner reflector), the flat surface RCS may be considerably higher than the rough surface RCS. And in the next chapter it will be seen that the RCS as a function of time on a moving sea surface can have peaks above the flat surface RCS for some targets. It is shown that the RCS as a function of roll angle should also be investigated to understand the RCS variations of a target on a realistic sea surface.

Chapter 5

Statistical Properties of the Ship Radar Cross Section

5.1 Introduction

In the last chapter the ray-optical approaches were shown to be useful for finding the bounds on the RCS pattern of a target on a rough sea surface, as a function of the elevation angle of the incident plane wave. In general, the pattern is bounded below by the coherent RCS computation, and bounded above by the RCS pattern for the target on an infinite flat surface. These bounding patterns are easy to find because they only require a simple plane wave scattering analysis combined with image theory. The effects of differing random sea surfaces and wind speeds on the RCS patterns were also investigated.

In this chapter the statistical properties of the RCS of a ship-like target on a rough sea surface are investigated. For these results the elevation angle of the incident plane wave and the wind speed will be held constant while other parameters are varied. In particular, the sea surface will evolve as a function of time so that the RCS as a function of time may be viewed. Also, the ship roll angle will be varied. Lastly, different target shapes will be considered. Conclusions are discussed at the end of the chapter.

5.2 RCS as a Function of Time

The RCS plotted as a function of time is probably the most realistic visualization of how the rough sea surface affects the RCS. In the results which follow, an initial random sea surface is allowed to evolve with time according to a deep-water linear hydrodynamic dispersion relation. The RCS is computed at each time step using the GFB method. The ship is allowed to float up and down with the waves so that the left side of the hull is always the same length above the waterline for each time step, but the ship is not allowed to roll as a function of time. (The roll of a ship is a very complex function of the moving sea surface, and depends on the ship center of gravity, inertial moment, etc., which is beyond the scope of this investigation.)

Figure 5.1 shows the RCS as a function of time for the 13 m high ship with a 90° hull angle of Figure 4.15 of the last chapter. The wind speed is 15 m/s, and at time zero the sea surface is exactly the same as Surface #4 of Figure 4.15. The elevation angle of the incident plane wave is held constant at 5°. Also shown is the RCS level for the ship on a flat surface and the coherent RCS, both of which obviously do not vary with time. Somewhat surprisingly, the peaks of the rough surface RCS never reach the flat surface level, as might be expected if the sea surface becomes locally flat near the ship. Figure 5.2 shows the actual evolution of Surface #4 at 5 second intervals. The vertical scales in this figure are stretched to better visualize the differences in the surfaces. At time zero the surface appears to be relatively flat just in front of the ship, so the RCS is expected to be high because of the corner reflector effect. The RCS pattern shows a peak at zero, but it is considerably lower than the flat surface level. At 5 s and 15 s the top of the ship reaches its highest points on top of the waves, but the RCS does not show peaks there. The RCS is low at 10 s and 20 s, but it is not immediately apparent how the local sea surface affects this.

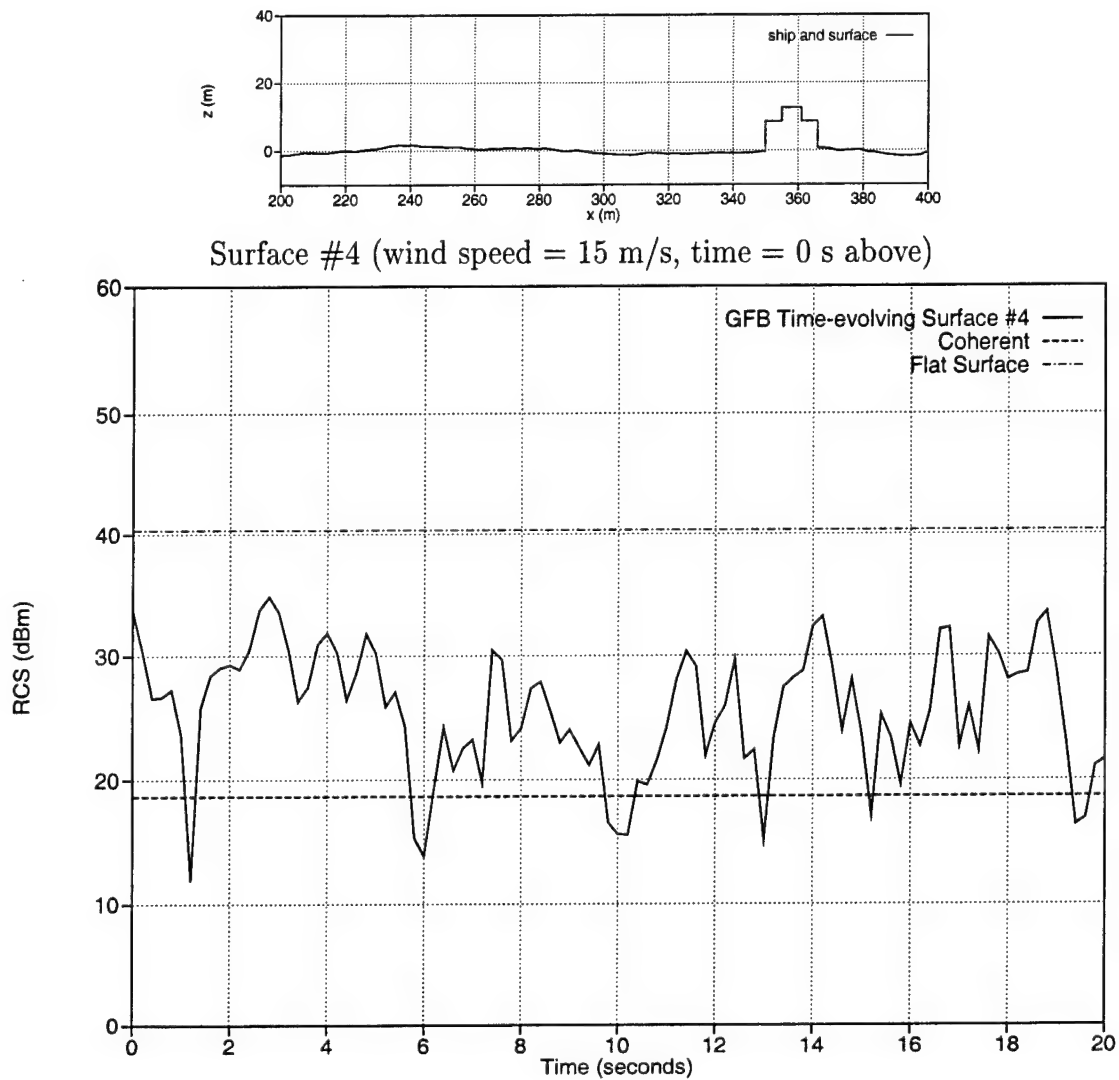


Figure 5.1: 2D RCS vs. time for a 13 m high ship on a 402.4 m surface. Elevation angle = 5° , wind speed = 15 m/s, frequency = 1 GHz.

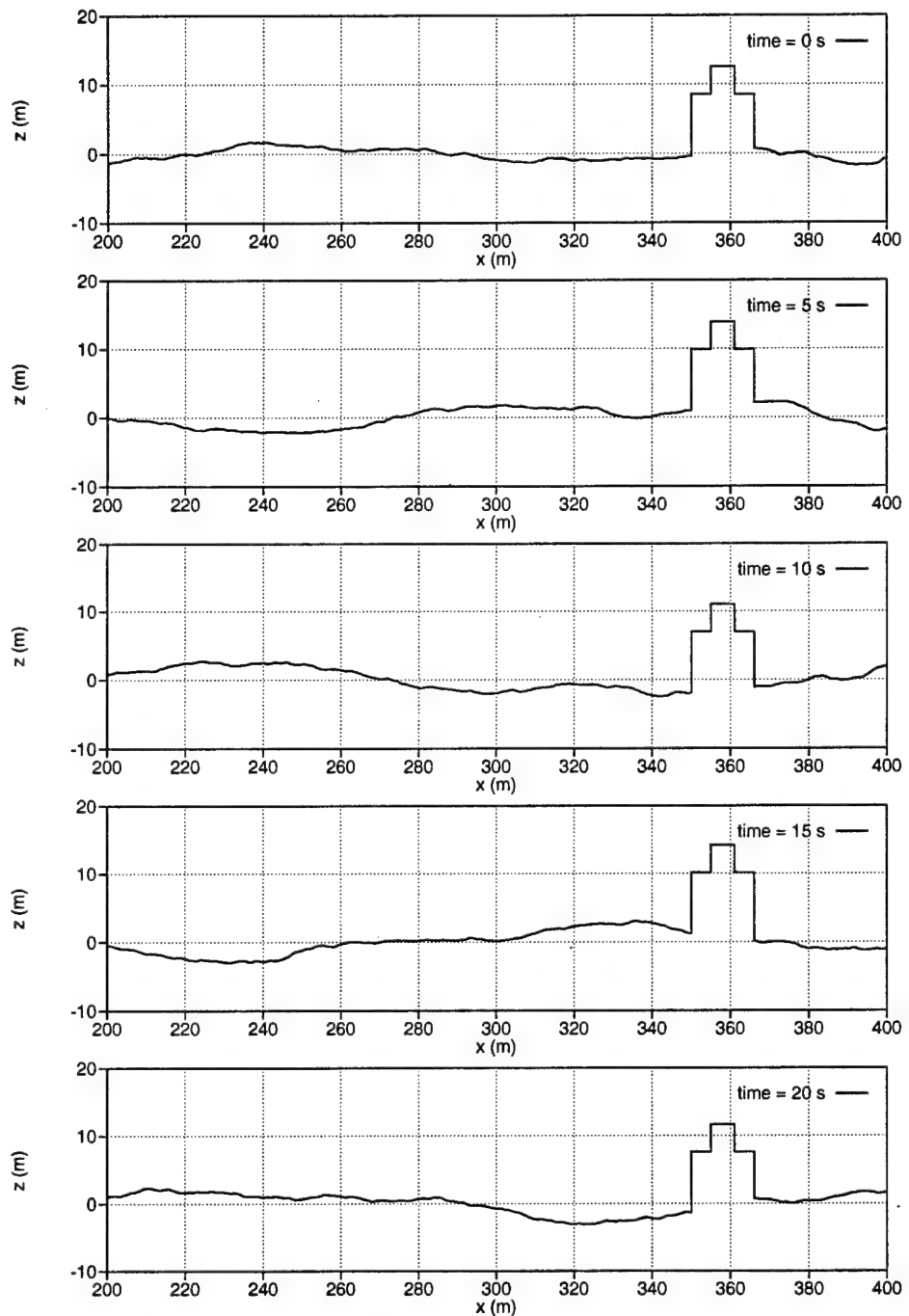


Figure 5.2: 13 m high ship on a 402.4 m time-evolving sea surface. Wind speed = 15 m/s, frequency = 1 GHz.

Figure 5.3 shows the same RCS vs. time result, with additional plots for wind speeds of 5 m/s and 10 m/s. The 5 m/s result is very close to the flat surface level, and the 10 m/s result has peaks a little higher than the 15 m/s result. Furthermore, the 5 m/s result does not vary much from its mean, while the 10 m/s and 15 m/s results vary quite significantly. The 15 m/s result is the most rapidly varying, although the range of variation is similar to the 10 m/s result.

Figure 5.4 shows the RCS vs. time for the 13 m ship with a hull angle of 80° at a wind speed of 15 m/s. Also shown is the ship RCS on a flat surface and the coherent RCS. The levels are lower than the 90° hull angle case, but the peaks of the time-varying RCS come closer to the flat surface level. The time-varying RCS pattern stays generally between the flat surface and coherent levels.

Figure 5.5 shows the backscattered fields as a function of time for a directive 300 MHz source antenna which is 150 m from the ship, as shown in the figure above the plot. The geometry is the same as in Figure 2.5 of Chapter 2. Units of RCS are not used, and the frequency is 300 MHz instead of 1 GHz, so the levels are not comparable to the previous results of this chapter. Three different wind speeds are considered in addition to the flat surface result (wind speed zero). For 5 m/s, $\sigma = 0.135$ m and $\sigma/\lambda = 0.135$. For 10 m/s, $\sigma = 0.54$ m and $\sigma/\lambda = 0.54$. For 15 m/s, $\sigma = 1.22$ m and $\sigma/\lambda = 1.22$. The important thing to note for this case is that the backscattered field can peak above the flat surface result for all three wind speeds.

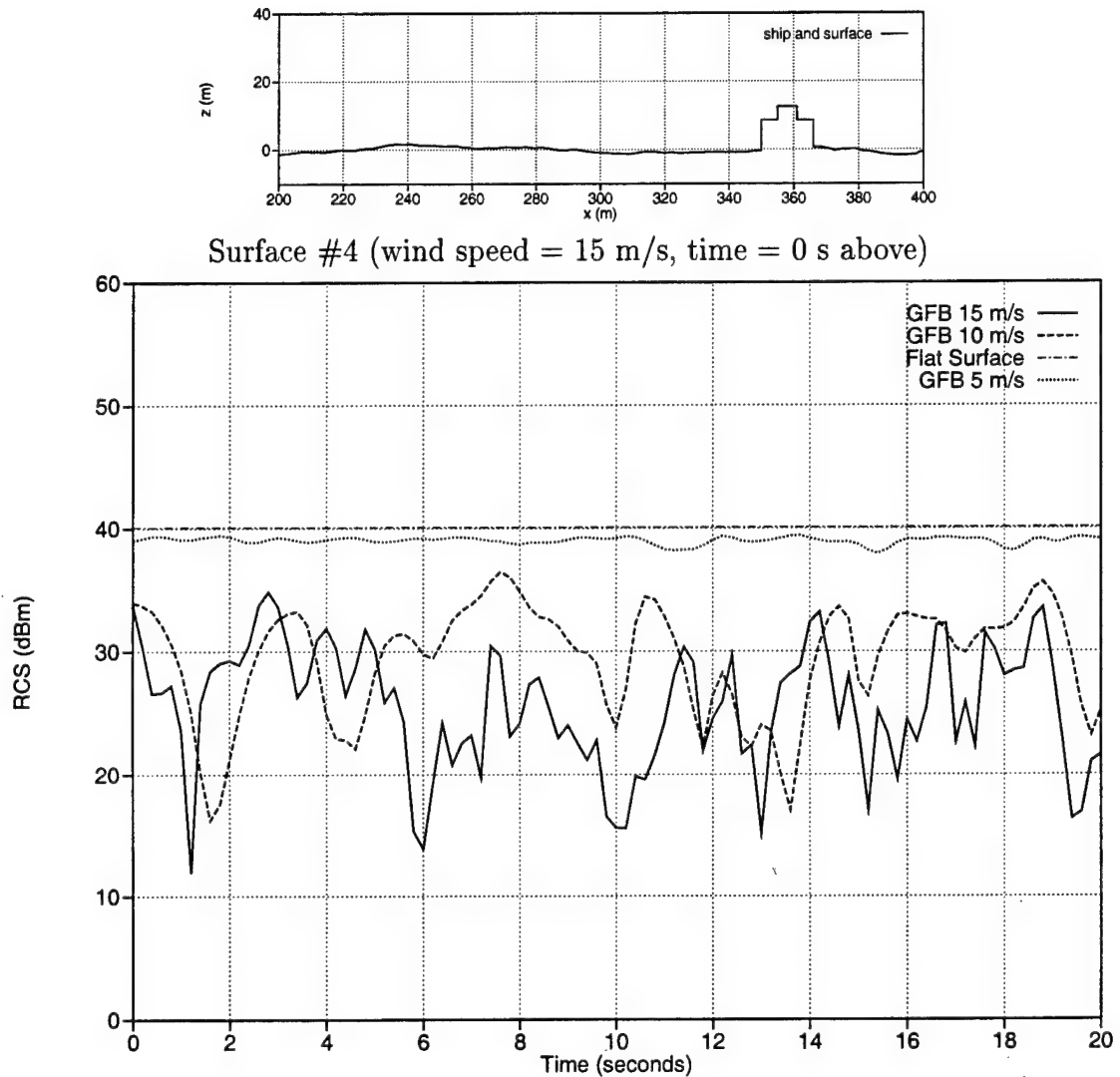


Figure 5.3: 2D RCS vs. time for a 13 m high ship on a 402.4 m surface at three different wind speeds. Elevation angle = 5° , frequency = 1 GHz.

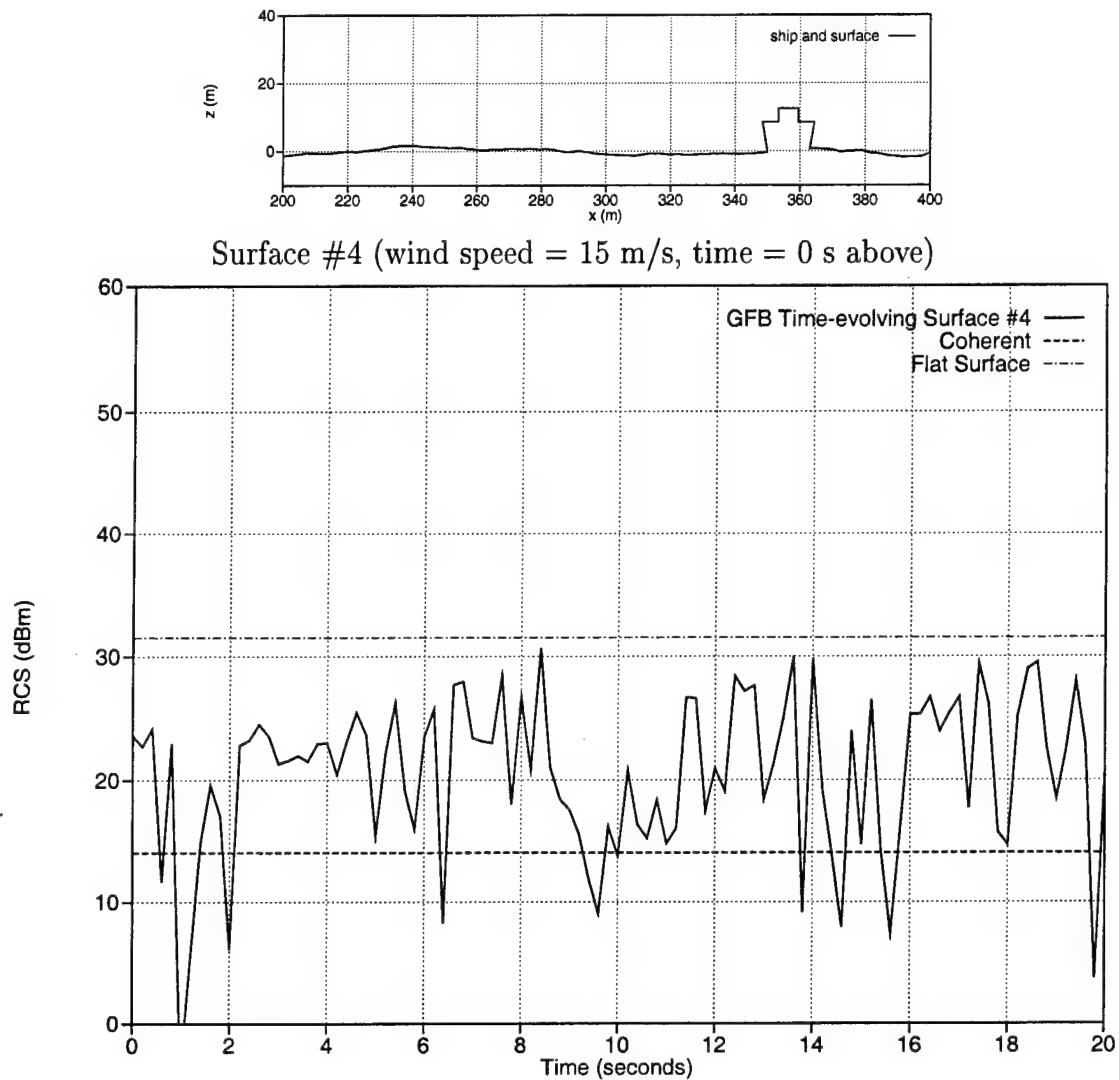
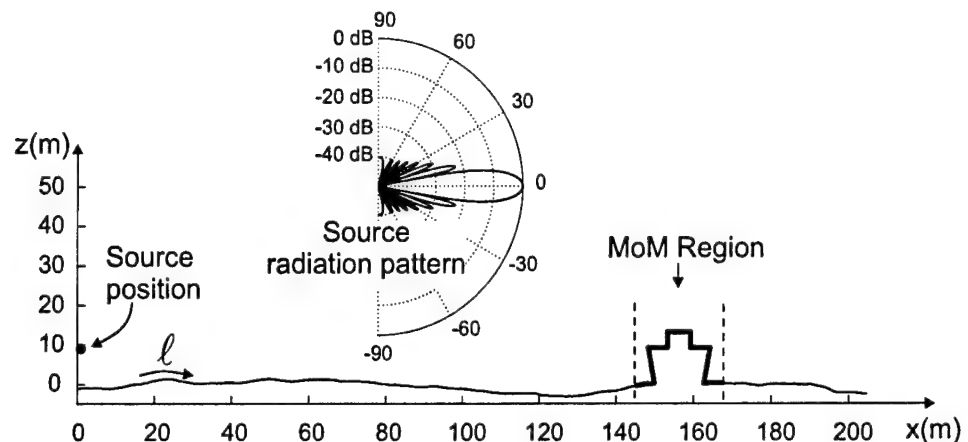


Figure 5.4: 2D RCS vs. time for a 13 m high ship on a 402.4 m surface. Elevation angle = 5° , wind speed = 15 m/s, frequency = 1 GHz.



Wind Speed = 15 m/s, at time = 0 s

$f=300\text{MHz}$, $l=204.8$, angle=5 deg

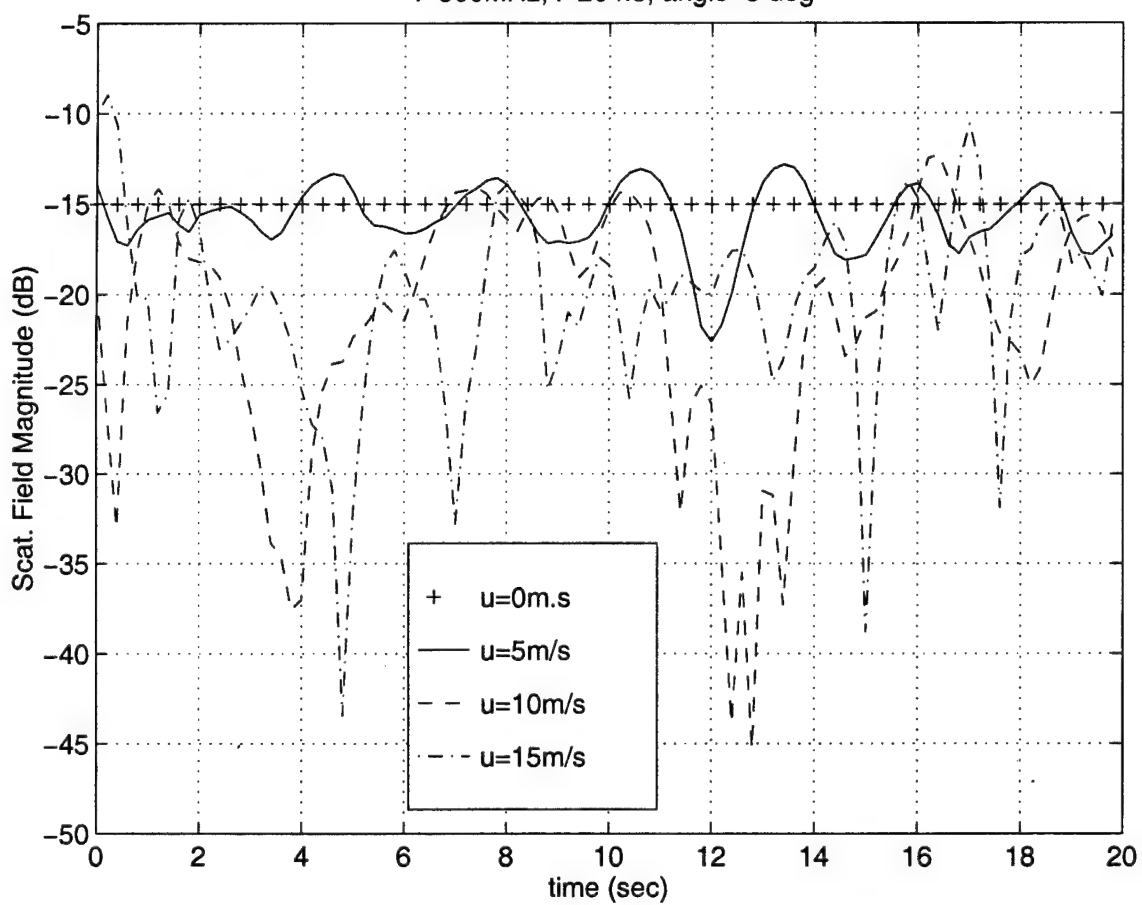


Figure 5.5: 2D backscatter vs. time for a 13 m high ship on a 204.8 m surface. Elevation angle = 5°, frequency = 300 MHz.

5.3 RCS as a Function of Ship Roll Angle

Figure 5.6 shows the RCS as a function of roll angle for the 13 m high ship on a flat surface with hull angles of 80° and 90° with respect to the horizontal plane. The elevation angle of the incident plane wave is 5° . The figures above the plot show the ships at a roll angle of $+10^\circ$. The large peak around 10° for the 80° hull angle is due to the left hull face forming a 90° corner reflector with the sea surface. Likewise, the large peak around 0° for the 90° hull angle is due to the left hull face forming a corner reflector with the sea surface. The peaks at -5° , 5° , and 15° are all due to the incident or sea reflected plane wave hitting the left hull face broadside. Away from the peaks, the pattern variations and overall levels are similar to the RCS vs. time plots. The exception is the 90° hull angle case for low wind speeds, where the corner reflector effect dominates independently of time.

It is interesting to note that the roll angle patterns are very similar for roll angles of less than -5° . For these angles the scattering appears to be dominated by the ship topsides (which are identical), and the scattering from the hull has a lesser effect.

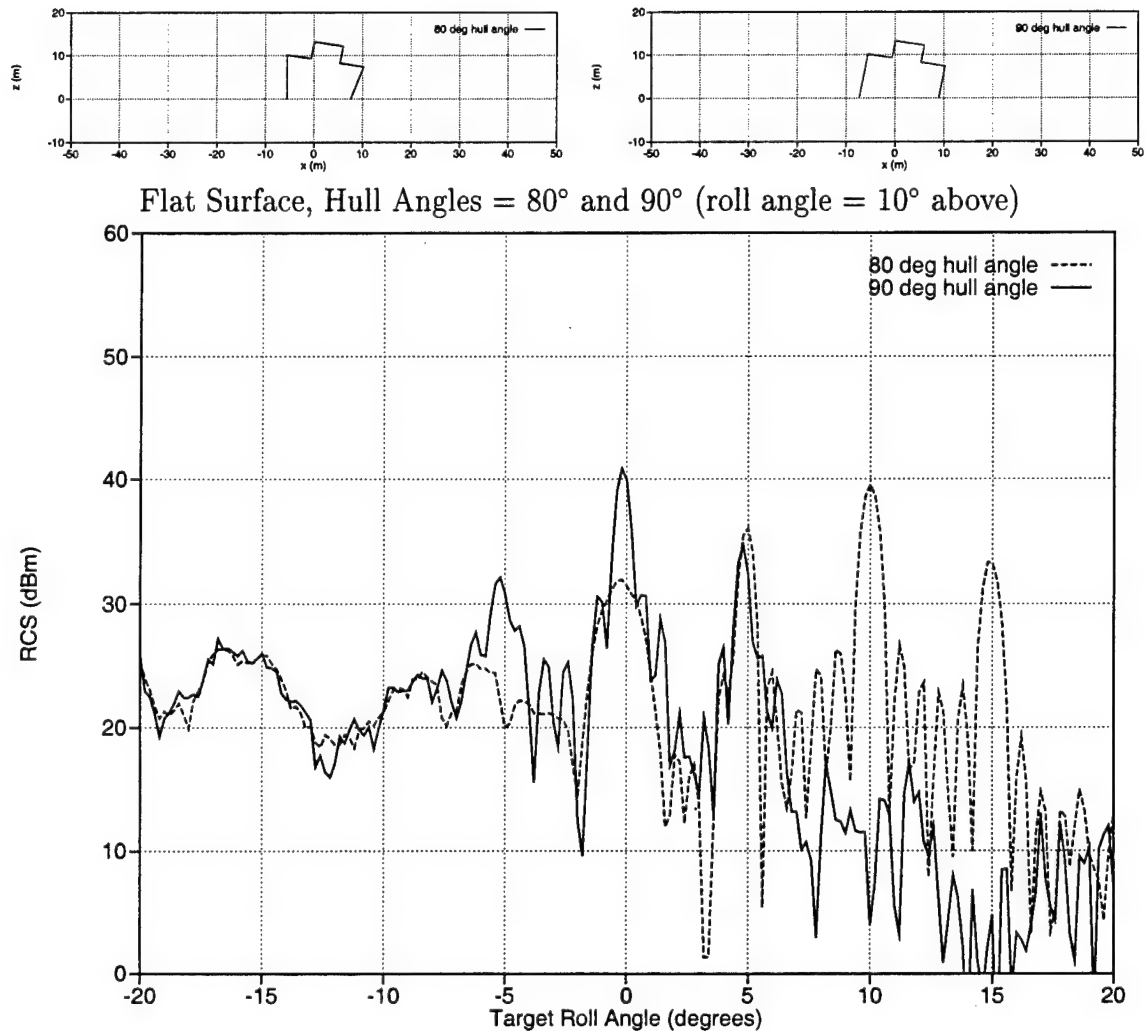


Figure 5.6: 2D RCS vs. roll angle for a 13 m high ship on a flat surface. Elevation angle = 5°, frequency = 1 GHz.

5.4 Effect of Target Geometry on the RCS

As was seen in the last two sections, the angle the hull makes with the sea surface has a strong impact on the ship RCS pattern. A hull angle of 90° gave the highest RCS levels for flat and time-varying sea surfaces. In general, the RCS for rough time-varying surfaces was lower than the flat surface result. The ship geometries considered so far have very high radar signatures. Next, the scattering characteristics of a low-RCS shape will be investigated.

Figure 5.7 shows the RCS vs. time for a low-RCS shape with wind speeds of 15 m/s and 5 m/s, and the elevation angle is again 5° . Also shown is the flat surface RCS for this elevation angle. The shape is 9 m high and the hull makes an angle of 110° with the horizontal plane (20° from vertical). The overall RCS level is about 30 dB lower than the previous ship geometries (note the vertical scale is shifted with respect to previous plots), but more important to note is that the flat surface RCS is less than most of the peaks in the time-varying RCS for this case. It is also significant to note that the RCS patterns for the two different wind speeds have about the same range of variation. This was not necessarily the case for the conventional ship geometries considered in the last two sections of this chapter. In particular, the RCS vs. time plot for the 90° hull angle at a wind speed of 5 m/s was very close to the flat surface result, while the 15 m/s result had large variations.

Figure 5.8 shows the RCS as a function of roll angle for the same low-RCS shape on a flat surface (computed using coherent scattering/image theory). The elevation angle of the incident plane wave is again 5° . For a roll angle of zero the RCS has a minimum. The large peak at -15° is due to the incident plane wave hitting the left hull face broadside. At -20° the left hull face is vertical, and makes a 90° corner reflector with the ocean. Since under normal conditions it is unlikely that the shape would roll more than 10° from vertical, the expected peak RCS level is about 10 dB for this shape. However, the RCS vs. time plots for this shape indicate a maximum RCS level of about 0 dB. A more detailed study is necessary to determine which level is more accurate under realistic conditions, but the conservative estimate is probably the most advisable to follow because a roll angle of only a few degrees greatly increases the RCS for this case.

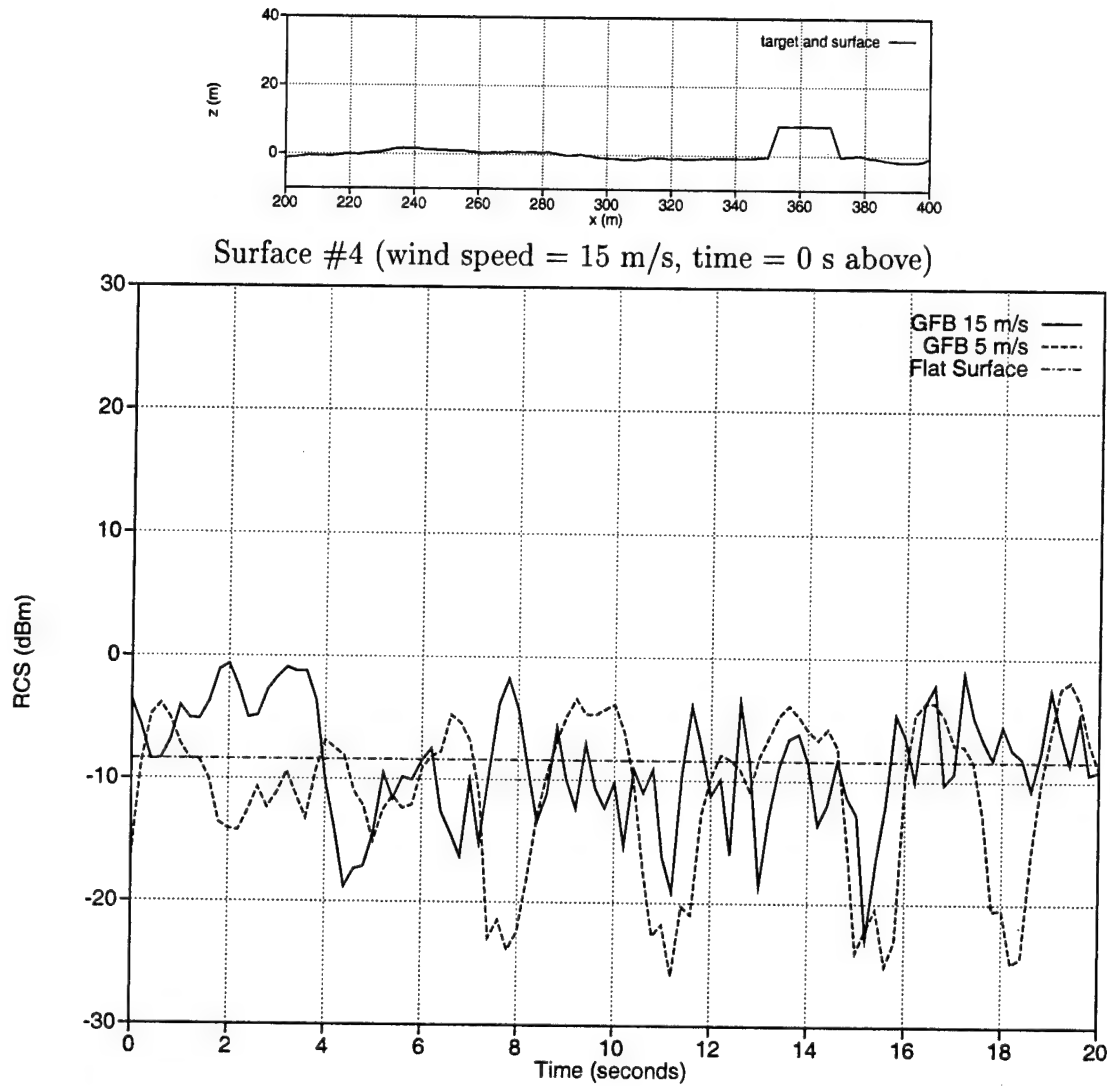


Figure 5.7: 2D RCS vs. time for a 9 m high low-RCS shape on a 402.4 m surface. Elevation angle = 5°, frequency = 1 GHz.

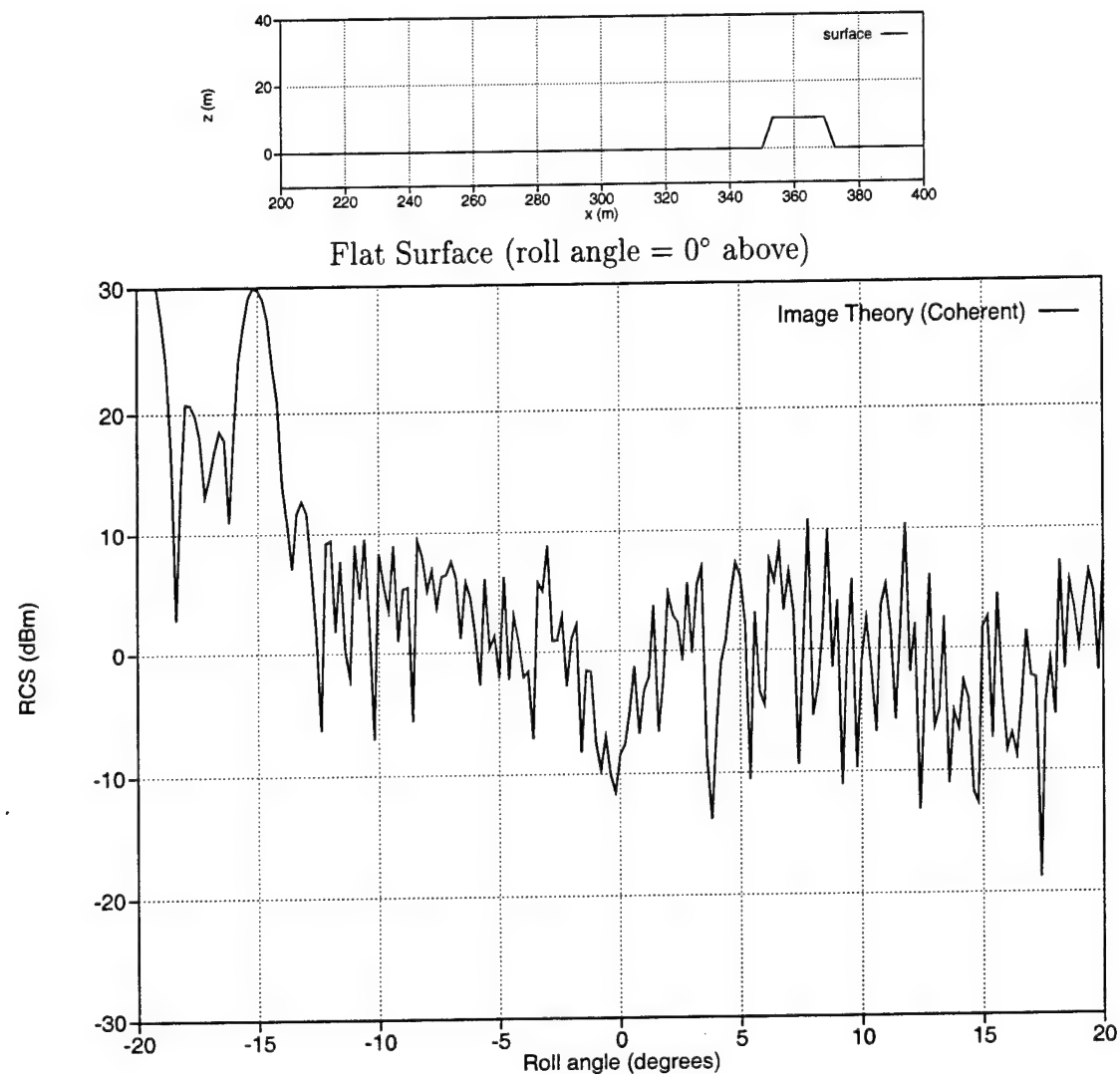


Figure 5.8: 2D RCS vs. roll angle for a 9 m high low-RCS shape on a flat surface. Elevation angle = 5°, frequency = 1 GHz.

It is clear from the results of this section that the shape of the target has a significant effect on how RCS varies as a function of the time-changing sea surface. It is clear that the roll angle may be the deciding factor on the peak RCS level, but it is beyond the scope of this investigation to determine how the roll angle of a ship varies with the sea state.

5.5 Conclusions

The RCS vs. time results of this chapter have shown that the RCS of a ship on a rough surface can be higher than the RCS on a flat surface. This is especially true for low-RCS shapes. On the other hand, the RCS as a function of roll angle for a ship on a flat surface shows the maximum expected RCS values. The maximum roll angle for a given ship and sea state should be available in most situations of interest (but is not available here), so the roll angle plot is probably the most useful for determining the peak RCS level which may be expected. It also seems to provide a good indication of the expected variation of the RCS as the sea surface changes with time or with wind speed.

Chapter 6

Conclusions and Future Directions

6.1 General Observations

The 2D investigation reported here into the radar scattering phenomenology of a target on a rough sea surface has yielded some interesting results, some expected, some not. It was expected that the time-varying RCS of a ship on a rough, moving sea surface could have peaks higher than the RCS of the same ship on a smooth surface. However, this appears to be true mainly for low-RCS shapes. For high-RCS targets, such as conventional ship designs where the hull makes close to a 90° angle with the sea surface, the time-varying RCS is generally lower than the flat surface level. For low-RCS targets the time-varying RCS ranges above and below the flat surface level.

It was expected that the variation (i.e., maximum deviation) of the time-varying RCS would depend strongly on the wind speed (or wave height). However, somewhat surprisingly, the results have shown that the variation is about the same for different wind speeds (except for the case when the wind speed is very low and the target has a high RCS, which tends to be close to the flat surface case).

Although a great deal of effort was spent to develop the spectrally accelerated GFB method described in Chapter 2, it was invaluable for efficiently computing many reliable scattering patterns. This made possible the phenomenology study of Chapter 5. It also provided valuable reference solutions for evaluating the ray-optical method of Chapter 4. Two journal papers are being prepared based on this work.

The investigation of Chapter 3 into the plane wave spectrum of the sea scattered field (with the target absent) yielded, as expected, a singular coherent component in the direction of reflection from a flat surface. In addition to the time-independent coherent component, the incoherent spectrum was seen to be randomly distributed in angle. The incoherent power spectrum appears to have a well-behaved probability distribution in angle, whereas the phase is uniformly distributed. Therefore, the incoherent spectrum averages to zero when sampled over many time steps. The amplitude of the coherent component of the sea scattered field is well-predicted by the physical optics formula derived in [1]. It approaches the amplitude of the incident plane wave for very low incidence angles and wind speeds, but rapidly approaches zero as the elevation angle or wind speed increases, or the frequency of the incident field increases. A discrete plane wave expansion was also investigated Chapter 3, and was shown to adequately reconstruct the incident and sea scattered field in the vicinity of the target. The expansion uses the incident and coherent sea scattered plane waves, in addition to a number of the strongest incoherent components.

The plane wave expansion for the incident field illuminating the target was used in Chapter 4 as a ray-optical excitation for finding the ship scattered field over the surface of the ship. As an approximation which allows the use of ray-optical methods, it is assumed that the ship is on a locally flat surface when solving for the ship scattered fields. A reciprocity integral was derived which computes the target backscattered field at the source using only the incident and scattered fields over the surface of the target, without having to back-track the scattered fields back to the source. This approach effectively decouples the ship scattering problem from the sea surface. It was found that by using only the coherent components of the illuminating field, the RCS would generally be under-predicted. Using a more complete discrete plane wave expansion using 50 plane waves predicted well the level of the RCS pattern, but not the details because of the locally planar approximation for the sea surface. However, the ray-optical approach developed here is not expected to predict the RCS pattern exactly, but instead be able to predict the peak levels and range of variation of the pattern which it does nicely.

The discrete plane wave expansion used for the incoherent sea scattered field was obtained here for a pre-determined sea surface, and required a numerically intensive computation. It is of interest to investigate the possibility of using a randomly generated plane wave expansion based on the probability distribution of the incoherent spectrum. This will be part of future work.

The RCS vs. time results of Chapter 5 were very insightful for visualizing the variation and peak levels of the RCS for a time-changing sea surface. However, since these results are only available from a numerically intensive reference solution which includes the entire sea surface (i.e., GFB), it is desirable to be able to instead use the ray-optical techniques which remove the sea surface from the computation. Unfortunately, the coherent scattering computations were shown to generally under-predict the RCS level, and the more complete plane wave expansion is also numerically expensive to obtain (although this may be remedied in future work).

The most useful ray-optical results were shown to be the flat surface RCS patterns, both as a function of elevation angle and roll angle. For high-RCS targets the flat surface result is generally the worst case in terms of peak RCS levels. But for low-RCS targets the flat surface RCS may be lower than the peaks of the time-varying RCS. In those cases the roll angle plots are especially useful for visualizing the variation of the RCS around roll angles close to zero. The flat surface RCS is easy to compute using ray techniques and/or image theory.

6.2 Future Work

Clearly, there is a little more investigation needed for 2D problems before proceeding to 3D. A better defined plane wave expansion is needed for the sea scattered field which illuminates the ship, one which only needs to know about the statistical properties of the sea surface and not the exact surface. The expansion should use the fewest plane waves necessary to get a good result, because too many plane waves could greatly reduce the efficiency of the ray-optical method. Another possible approach which is currently being investigated is to

use an equivalent planar impedance surface or periodic surface to model the sea surface locally in the vicinity of the ship. The equivalent surface would be chosen to best simulate the plane wave scattering characteristics of a random sea surface as a function of wind speed, frequency, and incidence angle.

The extension to 3D will begin with a spectral scattering analysis of a realistic 3D ocean surface. This will determine the statistical properties of the plane wave spectrum so that a randomly generated discrete plane wave expansion can be used to illuminate the ship. A 3D surface scattering code based on the forward-backward method with spectral acceleration is currently being developed under a separate project.

Next, the plane wave scattering from a 3D target will be computed using the local planar approximation for the sea surface. The scattering will be computed using the method of moments as in the 2D case, in addition to high-frequency methods such as physical optics and UTD. Of particular interest will be the use of the RCS Basic Scattering Code (RCS-BSC) which is based on the UTD and was developed here at the OSU ElectroScience Laboratory [11].

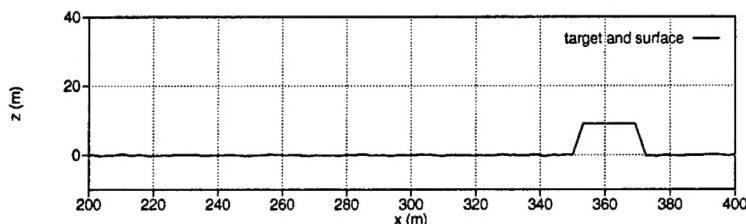
It will also be necessary to obtain 3D reference solutions for a target on a rough surface, possibly again using numerical solutions for some limited cases, and using available measurements. Not as much effort will be put into a full 3D numerical solution (which implicitly includes the sea surface) as was put into the 2D GFB code because of the numerical and geometrical complexity. Only a few selected configurations will be analyzed numerically to establish the reliability of the ray-optical methods.

6.3 A Final Note on Coherent Scattering

It needs to be re-emphasized that for most realistic situations the incidence angle is very close to grazing the sea surface because the height of the source antenna is going to be much smaller than the distance to the target. Therefore, the coherent sea scattered plane wave component is expected to typically be very strong according to Eq. (3.6). Physically, this means that the random variations in the sea scattered field tend to average out to zero over

long propagation distances, so only the coherent field remains. This lends further importance to the flat surface RCS analysis because for grazing angles the incident field is nearly the same as for a flat surface. Unfortunately, the GFB reference solution becomes less accurate for grazing incidence because the sea surface must be truncated to a finite length which is usually much less than the distance from the source to the target. Since the numerical reference solution is unreliable for this case, realistic experimental data is needed to support the hypothesis that the coherent scattering computation is sufficient in most cases of interest, provided that variations in the target roll angle are included in the analysis.

Figure 6.1 shows RCS vs. time plots for the low-RCS target from Figure 5.7 at a wind speed of 5 m/s, with the elevation angle of the incident plane wave at 5° and 1.6° . The magnitude of the coherent sea scattered plane wave component computed from (3.6) for an elevation angle of 1.6° is 0.99 of the incident plane wave magnitude. Therefore, the RCS is not expected to vary much with time as the plot confirms. For 5° the coherent component is 0.89 of the incident plane wave, so the RCS would also not be expected to vary much with time, but the plot shows large variations. Investigation of realistic experimental data is needed to better understand at what point the RCS becomes strongly coherent, and whether the time variation of the RCS is determined more by the sea surface or the rolling of the target. One thing is certain from the numerical results of this report: if the coherent sea scattered term given by (3.6) is much smaller than 1, the time-varying RCS of a target on the sea surface will have large variations. A limit to the variation is reached as the coherent component approaches zero, which depends on the frequency and elevation angle as well as the wind speed.



Surface #1 (wind speed = 5 m/s, time = 0 s above)

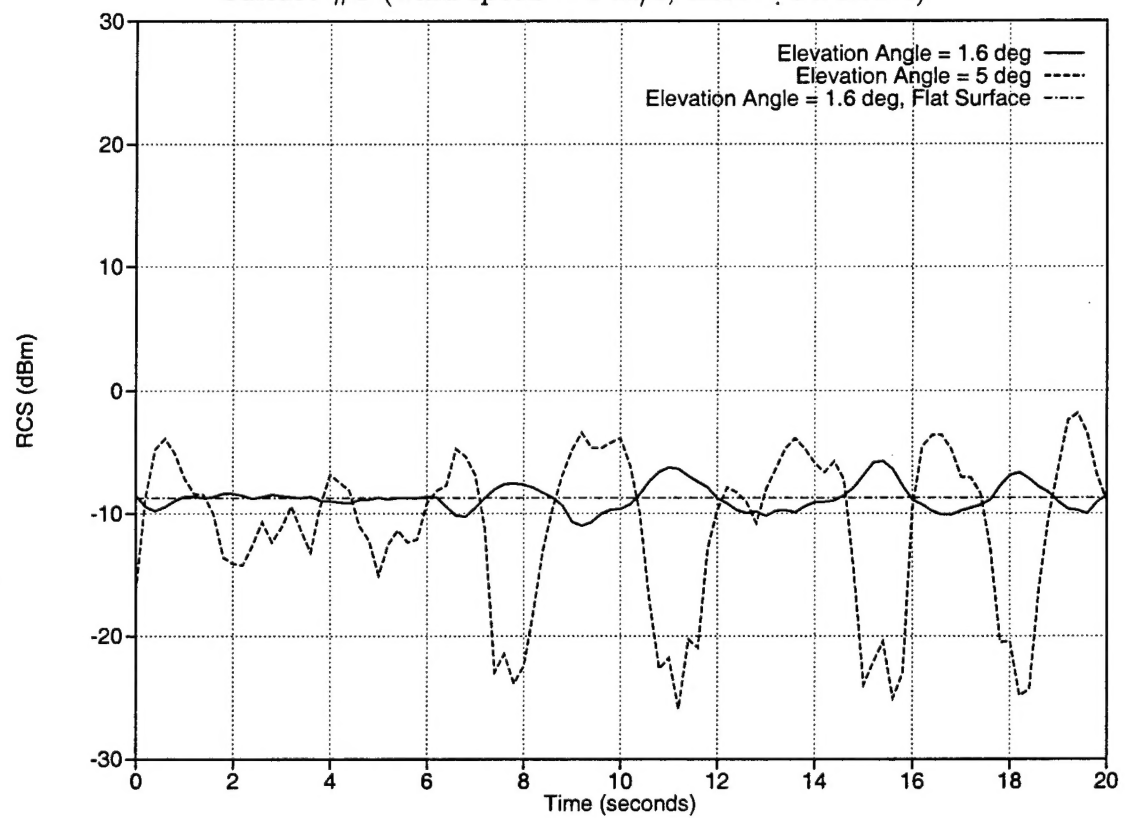


Figure 6.1: 2D RCS vs. time for a 9 m high low-RCS shape on a 402.4 m surface with two different incidence angles. Wind speed = 5 m/s, frequency = 1 GHz.

Bibliography

- [1] L. Tsang, J. A. Kong, and R. T. Shin, *Theory of Microwave Remote Sensing*. Wiley, New York, 1985.
- [2] M. Skolnik, *Radar Handbook*. McGraw-Hill, New York, 1990.
- [3] P. H. Pathak, *Antenna Handbook, Theory Application and Design: Techniques for High Frequency Problems*. Van Nostrand Reinhold, 1988.
- [4] R. F. Harrington, *Time-Harmonic Electromagnetic Fields*. McGraw-Hill, New York, 1961.
- [5] D. Holliday, J. L. L. DeRaad, and G. J. St-Cyr, "Forward-Backward: A new method for computing low-grazing angle scattering," *IEEE Trans. Ant. Prop.*, vol. 44, pp. 722–729, May 1996.
- [6] H.-T. Chou and J. T. Johnson, "Novel Acceleration algorithm for Forward-Backward method in the computation of scattering from rough surfaces," *Radio Science*, vol. 33, no. 5, pp. 1277–1287, 1998.
- [7] R. F. Harrington, *Field Computation by Moment Method*. IEEE Press, 1993.
- [8] W. J. Pierson and L. Moskowitz, "A proposed spectral form for fully developed wind seas based on the similarity theory of S.A. Kitaigorodskii," *J. Geophys. Res.*, vol. 69, pp. 5181–5190, 1964.
- [9] R. J. Burkholder and D.-H. Kwon, "High-frequency asymptotic acceleration of the fast multipole method," *Rad. Sci.*, vol. 51, pp. 1199–1206, Oct. 1996.
- [10] D. Torrungrueng and E. H. Newman, "The Multiple Sweep Method of Moments (MSMM) Analysis of Electrically Large Bodies," *IEEE Trans. Ant. Prop.*, vol. 45, pp. 1252–1258, Aug. 1997.
- [11] R. J. Marhefka, "Radar Cross Section - Basic Scattering Code RCS-BSC (Version 2.0) User's Manual," *The Ohio State University ElectroScience Lab Technical Report 718295-15*, Feb. 1990.

Antennas
Adaptive Arrays
Diffraction and Scattering
Electromagnetic Compatibility
Ground Penetrating Radar
Numerical Techniques
Radar and Antenna Metrology

THE OHIO STATE UNIVERSITY
ElectroScience Laboratory

Department of Electrical Engineering
1320 Kinnear Road
Columbus, Ohio 43212-1191
esl.eng.ohio-state.edu

Radar Cross Section Studies
Radar Imaging
Satellite Communications
Signal Processing
Target Identification
Wave Propagation
Wireless Communications
April 29, 1999

Mr. Ronald P. Radlinski, ONR 334
Office of Naval Research
Ballston Centre Tower One
800 North Quincy Street
Arlington, VA 22217-5660

Dear Mr. Radlinski:

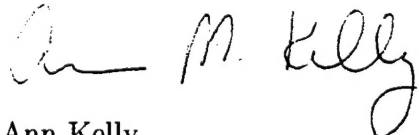
Enclosed are 3 copies of the report

"Development of Ray-Optical Methods for Studying the RCS of 2D Targets on a Rough
Sea Surface"

by R.J. Burkholder, M.R. Pino and D.-H. Kwon, Report No. 735231-1, dated January 1999,
prepared under Grant No. N00014-98-1-0243.

We have enjoyed working with you on this project and trust that this report is satisfactory.
We look forward to the opportunity of working with you again in the future.

Sincerely,



Ann Kelly
Editorial Services

MPN: 865509
Date: April 29, 1999
RF Project No. 735231
Type of Report: Technical
Shipped by Registered Mail

cc: A. Rundle

1 copy of report, Director ONR
2 copies of report, DTIC